Important Notice

UNIVERSITY OF CALGARY

Iterative Multiparameter Elastic Waveform Inversion Using Prestack Time Imaging and Kirchhoff approximation

by

Hassan Khaniani

A THESIS

SUBMITTED TO THE FACULTY OF GRADUATE STUDIES

IN PARTIAL FULFILLMENT OF THE REQUIREMENTS FOR THE

DEGREE OF DOCTOR OF PHILOSOPHY

DEPARTMENT OF GEOSCIENCES

CALGARY, ALBERTA

January, 2015

ABSTRACT

This thesis proposes a “standard strategy” for iterative inversion of elastic properties from the seismic reflection data. The term “standard” refers to the current hands-on commercial techniques that are used for the seismic imaging and inverse problem. The method is established to reduce the computation time associated with elastic Full Waveform Inversion (FWI) methods. It makes use of AVO analysis, prestack time migration and corresponding forward modeling in an iterative scheme.

The main objective is to describe the iterative inversion procedure used in seismic reflection data using simplified mathematical expression and their numerical applications. The frame work of the inversion is similar to (FWI) method but with less computational costs. The reduction of computational costs depends on the data conditioning (with or without multiple data), the level of the complexity of geological model and acquisition condition such as Signal to Noise Ratio (SNR). Many processing methods consider multiple events as noise and remove it from the data. This is the motivation for reducing the computational cost associated with Finite Difference Time Domain (FDTD) forward modeling and Reverse Time Migration (RTM)-based techniques. Therefore, a one-way solution of the wave equation for inversion is implemented.

While less computationally intensive depth imaging methods are available by iterative coupling of ray theory and the Born approximation, it is shown that we can further reduce the cost of inversion by dropping the cost of ray tracing for traveltime estimation in a way similar to standard Prestack Time Migration (PSTM) and the corresponding forward modeling. This requires the model to have smooth lateral variations in elastic properties, so that the traveltime of the scatterpoints can be approximated by a Double Square Root (DSR) equation.

To represent a more realistic and stable solution of the inverse problem, while considering the phase of supercritical angles, the boundary condition of the wave equation is set up along reflection surfaces. Hence, the surface integral Kirchhoff approximation is used as a mathematical framework instead of the volume integral of the Born approximation.

In addition, I study the feasibility of iterative coupling of ray theory with the Kirchhoff approximation for inversion. For the amplitude considerations, the direct relationship between the scattering potential of the Born approximation with the reflectivity function of the asymptotic

Kirchhoff approximation for elastic waves is used. Therefore, I use the linearized Zoeppritz approximation of Aki and Richards (1980) for computation of the forward modeling and migration operators as well as gradient function from Amplitude vs Offset (AVO) inversion.

The multiparameter elastic inversion approach is applicable to all types of reflected wavefields such as P-to-P, P-to-S, S-to-S and S-to-P. Traveltime estimation of forward modeling and migration/inversion operators are based on the DSR equation. All operators involved in inversion, including the background model for DSR and AVO are updated at each iteration. The migration/inversion procedure maps the mode converted waves to the traveltime of incident waves which fixes the registration problem of events that travel from source to scatter point. The inversion of the reflected P-to-P and P-to-S synthetic and field data are provided for the numerical examples.

This approach is applicable for complex structures however, to estimate the traveltime of scatterpoints, ray tracing can be added to the algorithm. For such a medium, the scatterpoint traveltime approximations from the PSTM, is compared to the PSDM approach using numerical analysis of ray- and FDTD-based modeling.

In part of this thesis, I further improve the conventional velocity analysis of Common Scatter Point (CSP) gathers by including the tilt effects. I show that travel time response of scatter points beneath a dipping interface experiences an additional linear time shift. The normal hyperbolic shape of travel time in a CSP gather becomes tilted, causing inaccuracy in velocity analysis. The focusing of the separated energy in the semblance plots is enhanced by removing the tilt effects. As a result, the accuracy of migration velocity inversion is enhanced and the focusing of output images of time migration is improved.

Acknowledgements

I wish to thank sponsors of the Consortium for Research in Elastic Wave Exploration Seismology (CREWES), Department of Geoscience, University of Calgary for supporting my work and for providing necessary and useful courses during my education. In collaboration with the CREWES project, the shale gas department of Nexen Energy ULC has also supported this thesis and provided me the opportunity to study its data set. This collaboration greatly contributed to dealing with the implementation of the elastic FWI method on field acquired multicomponent data.

I would like to thank Dr. John C. Bancroft for his supervision, guidance and making corrections to my research. He allowed me a great deal of independence and provided unfailing encouragement and support.

My special thanks go to Eric von Lunen, from Nexen Energy ULC, for providing me with exceptional mentorship and support. His thoughts and industry experience on inverse problems from field data was invaluable. I also want to express my appreciation to Dr. Stephen Jensen for his comments on this work. My appreciation also goes to David Gray, Dr. Jennifer Leslie-Panek and Jason Hendrick for their encouragement during my work at Nexen.

I want to thank Dr. Gary F. Margrave, as I became inspired to work on the Full Waveform Inversion problem largely due to his encouragement. Thanks to Dr. Laurence Lines for his motivations and supports to continue my education in geophysics. Thanks to Joan Embleton for her useful helps, advises and supports. Thanks to Laura Baird for her useful assistances and supports. I also want to thank Dr. Edward S. Krebes and Dr. Kristopher Innanen for their course notes and teachings at the University of Calgary.

Many thanks go to Neda Boroumand for many useful discussions, motivation and contributions to this thesis. I also appreciate Dr. Shahpoor Moradi for his useful suggestions and for sharing his interesting views on this thesis from the physics perspectives.

I am thankful to Dr. Sylvestre Charles, Shahin Moradi, Dr. P. F. Dale, Jared Fath, Dr. Abdolnaser Yousefzadeh, Dr. Mostafa Naghizadeh, Dr. Hossein Aghabarati, Dr. Saeed Taheri, Liliana Zuleta,

Ben Wards, Marcus Wilson, Davood Nouroozi, Dr. Peter Manning, Kevin Hall, Amir Shamsa, Mahdi Zeidooni and Dr. Hugh Geiger for many constructive discussions.

Finally, and most importantly, I would like to thank my wife Simin Negintaji for her support, encouragement and quiet patience that allowed me to dedicate most of my time to school.

Dedication

To Simin

Contents

List of Tables

List of Figures

Chapter 1: Introduction

1.1 Exploring the Earth's subsurface

Seismic data can play an important role in the exploration and exploitation of oil and gas reservoirs. It contains information from waves that propagate through the subsurface and arrive at one or more receivers. Analyzing the recorded wave in terms of their travel time, amplitude and phase, then deriving a model of the subsurface, are the main objectives of this thesis. I study seismic reflection data, which is wave energy that responds to variations in subsurface properties. These reflectors correspond to interfaces where contrasts in the elastic properties of the subsurface medium exist. When the wave energy interacts with this interface, some of the energy is reflected back toward the receivers located on or beneath the surface of the earth. This interaction is governed by wave equation, which is defined by a mathematical and physical relationship of subsurface models. In this studies, elastic wave equation is used are obtained from coupling of Newton's second law of motion and the Hooke's law of elasticity.

1.2 Subsurface imaging

Figure 1-1 represents a cross section of an Earth model, and shows reflection of different layers of rock that have different rock properties (e.g., a velocity model). One objective of acquiring seismic data is to obtain an image of this subsurface geology. Knowledge of this geology will aid in finding minerals and hydrocarbon reservoirs.

Seismic data can be acquired by an energy source at or near the surface with many receivers on the surface to record the reflection energy as illustrated in Figure 1-2. These records can be made by recording waves that originate from different source locations. For each record, any subsurface point scatters the incident wave, and contributes to the energy of received wave. These points are referred as "**scatter points**" and in this thesis is the basis for analysing the recorded data. It incorporates the approximation of traveltime and amplitude of the scattered waves in the recorded wave (see e.g., blue dots in Figure 1-2). These approximation depends on the ray paths that the wave originated from the source then scattered toward the recovers (see e.g., red lines inside velocity model of Figure 1-1). The recorded data is processed using imaging algorithms to produce an image of the geology as illustrated in Figure 1-3. Knowledge of the subsurface not only aids in identifying the location of stored hydrocarbons, but also the different type of rock that produces it (e.g., source rock).

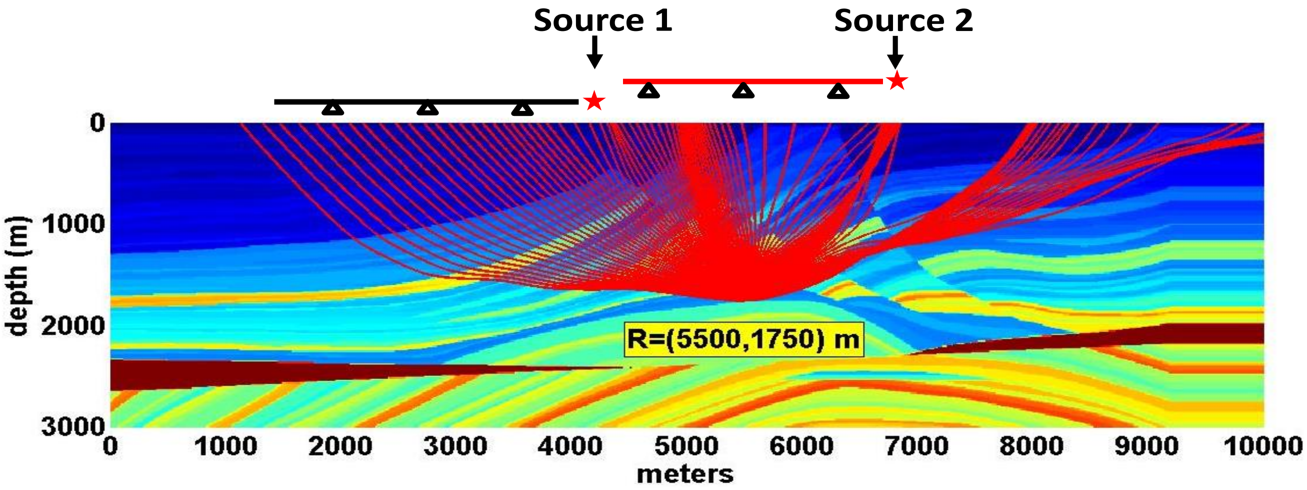

Figure 1-1: Marmousi model and the two source position. A fan of rays (red lines) emanate from the scatter point **R** and travel toward the receivers laid in surface.

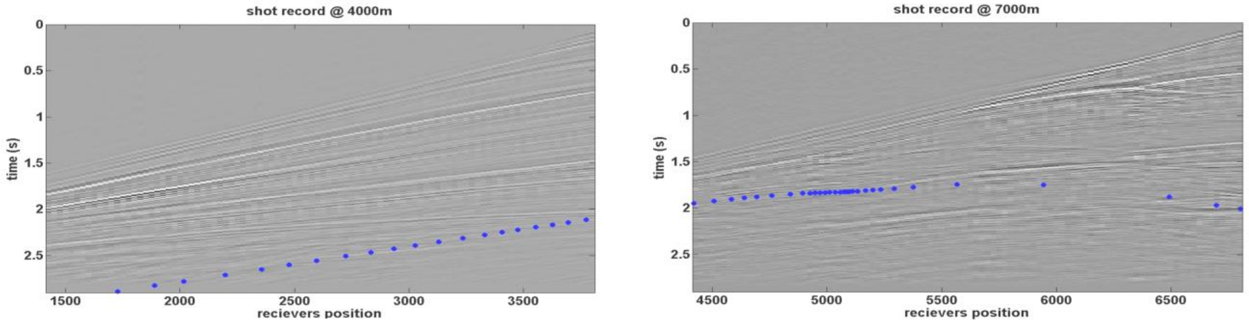

a) b)

Figure 1-2 Shot records of model shown in Figure 1-1. a) Shot record of source 1. b) Shot record of source 2. The blue dots shows the contribution of scatter point R.

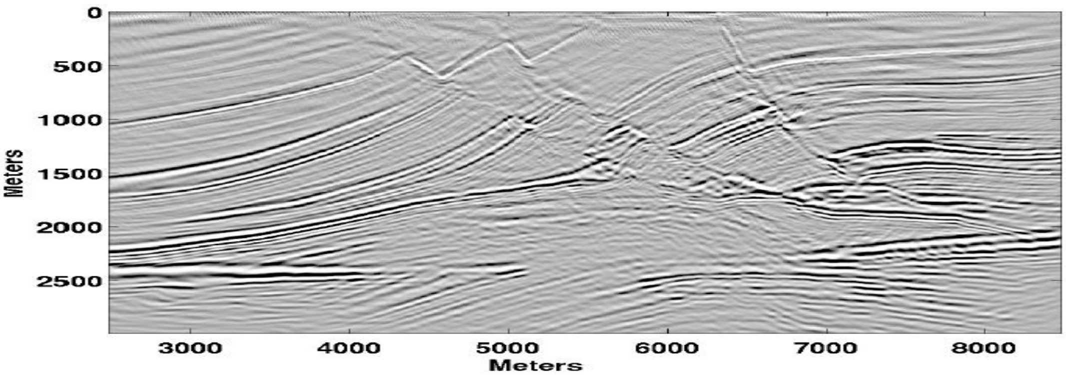

Figure 1-3: An image of the Marmousi data set using RTM. Image captured from Wards et al., (2008).

1.3 Wave types in the subsurface.

Energy in the subsurface can propagate with two different modes known as the P-wave and the S-wave. In the P-mode, the particle motion is in the direction of propagation, similar to "push-pulling" a hose. In the S-mode, the particle moves sidewise to the direction of propagation, similar to shaking a hose "sideways". Each of these modes has a different propagation velocity and different reflecting properties from the same rock type. The analysis of the P- and S- wave from seismic data helps to estimate the rock properties.

1.4 Seismic processing, migration, and inversion

There are many steps to processing seismic data from removing of noise to the focusing the reflection energies to their reflector location. These steps can take many source records (as in Figure 1-2) to create the image in Figure 1-3. The major processes that we are concerned within this thesis are those of seismic migration and inversion.

I will refer to seismic true amplitude migration as simply "**<u>migration</u>**" and its objective is to relocate the reflection energy on the source records, to the location of the reflector. It is mainly designed to define the structure in terms of time space and amplitude.

The objective of seismic inversion, or simply "**<u>inversion</u>"**, is to identify the properties of the rock. These properties include the propagation velocities of P- and S- modes, and density. From these properties we can identify other properties such as fluid content, or the orientation of fractures.

There are several approaches for the migration of seismic data that can be classified as "**depth migration**" or "**time migration**". Depth migrations migrate the seismic data to a model as a function of depth. It requires mainly the input velocity models as a function of depth and it needs to solve the depth based wave equation to obtain the traveltime of the reflectors (e.g., ray tracing, FDTD). Time migrations migrate the seismic data to the model as a function of time. The input velocity model is usually defined as a function of time and it assumes that the paths of the rays of the waves have predictable pattern. The assumptions of time migration helps to solve the wave equation to obtain the traveltime of the reflectors faster than the corresponding depth migration. The approach presented here is applicable to both depth migration and time migration, however, I will be using Prestack Kirchhoff Time Migration (PSTM) which has economical computation time.

Computational time is currently a big challenge when implementing the wave equation to model earth response. In this regard, the wave equation is best classified in two types:

1- **Two-way wave equations** such as Time Domain Finite Difference (FDTD) or Frequency Domain Finite Difference (FDFD).
2- **One-way wave equations** such as the one-way Kirchhoff, or phase shift downward continuation methods.

Two-way wave equations are more expensive compared to one-way wave equations, but they have the potential to use multiple reflections in the data. One-way wave equations assume that multiple reflections have been removed from the data, but they require less computational time. Currently, most standard geophysical applications for earth model estimation are based on the one-way wave equation.

Many processes in geophysics use the term inversion to estimate or approximate the rock properties. I will be using a process known as Full Waveform Inversion (FWI) method that uses repeated migrations and inversions to form a more accurate estimate of rock properties. The approach requires iterations for inversion as is in the attention of several authors (e.g., Tarantola 1984a, 1984b & 1986, Mora, 1987, Plessix, 2008, Ikelle et al., 1986; Pratt, 1999). The iterations require improvement in lower computational costs (e.g., Vigh and Starr, 2008, Sirgue and Pratt, 2004; Maurer et al., 2009). In this study the computation cost for iterative inversion is reduced by implementing one-way PSTM and corresponding forward modeling approximation. Two approaches for the solution of the one-way equation are considered here. The first approach is the **Born approximation**. It is a volume integral approach and has been implemented for iterative inversion of subsurface properties (Beydoun and Mendez, 1989 and Jin et al., 1992). The second approach is the **Kirchhoff approximation** which is a surface integral based on the changes of elastic properties across the bedding interface (Bleistein, 1986). I study and implement the Kirchhoff approximation approach for the iterative inversion scheme.

1.5 My contributions in this thesis

The contributions can be summarized as follows.

1) Implementation of the Kirchhoff approximation in an iterative FWI method for multiparameter elastic inversion.

2) Numerical simplification of the FWI method for several mode converted data (e.g., P-to-P, P-to-S) by implementing a time-imaging method of forward modeling and corresponding migration/inversion.

3) Implementation of a migration scheme for multicomponent P-to-P and P-to-S waves based on scatter point P-wave time. This solves the subsurface registration problem for prestack time migration. The value of combined P-to-P and P-to-S inversion can be significantly greater than the interpretation of the individual volumes.

4) Facilitation of joint elastic inversion based on proposed P-to-P and P-to-S seismic migration schemes.

5) Use of the relationship between the solution of the wave equation by Born approximation (e.g., Beylkin and Burridge, 1990) and Kirchhoff approximation (e.g., Bleistein, 1984) to demonstrate that the conventional AVO inversion can be used for gradient calculation in the FWI method.

6) Enhancement of the conventional AVO procedure. The first iteration of the method is equivalent to conventional AVO inversion. Once the algorithm is iterated, the conventional AVO result will be updated.

7) Implementation of the PSTM numerical algorithm on real multicomponent P-to-P and P-to-S data.

8) Enhancing migration PSTM image output and the migration velocity analysis by implementation of tilt effect to Common Scatter Point (CSP) gathers.

1.6 Thesis overview

Chapter (2) explains the nonlinear least squares concept and its relationship with perturbation theory. I start with a one-step inversion according to perturbation theory and Born approximation, then explain its roles in the FWI method. The FWI method presented here has two main features. One, it is based on the Kirchhoff approximation instead of the Born approximation, and two, it is based on the time imaging approach instead of depth imaging. I compare PSDM to PSTM and the corresponding forward modeling associated with the inversions. Similarly, I use numerical examples to compare the consistency of three seismic modeling and imaging techniques, namely Kirchhoff time migration, ray-based depth migration, and Finite Difference Time Domain (FDTD) modeling. I compare the modeled scatter point response obtained with the ray tracing method and the finite difference method. To illustrate coherency, both ray-traced data and finite difference data are mapped to a CSP gather, which is an intermediate PSTM gather of Equivalent Offset Migration (EOM) (Bancroft et. al. 1998). The final section of Chapter (2) is inspired by the paper written by Beylkin and Burridge (1990) on the subject of the Born approximation and perturbation theory for derivation of scattered wave fields in an elastic medium.

Chapter (3) is inspired by the hyperbolic formulation of Common Scatter point (CSP) gathers of Equivalent offset Migration (EOM) and its application to the inverse problem of the acoustic wave equation. I further improve the conventional velocity analysis of CSP gather by including the tilt effects. I show that travel time response of scatter points beneath a dipping interface experiences an additional linear time shift. The normal hyperbolic shape of travel time in a CSP gather becomes tilted, causing inaccuracy in velocity analysis. The focusing of the separated energy in the semblance plots is enhanced by removing the tilt effects. As a result, the accuracy of migration velocity inversion is enhanced and the focusing of output images of time migration is improved. I discuss the implementation of the FWI method for velocity inversion using time imaging methods. I used a forward Kirchhoff operator for the prediction of shot records from a P-to-P reflectivity function and first order Born approximation for inversion of the velocity model. Estimation of the gradient function using PSTM is compared to PSDM approaches.

In chapter (4), formulations of Born approximation of Chapter (2) are related to the Bleistein's Kirchhoff approximation in the framework of FWI method. The importance of associated Boundary Condition (BC), the migration of P-to-P and P-to-S data and the estimation of gradient function of FWI approach using Born and Kirchhoff approximation are illustrated by simple numerical examples. Using analytical and numerical analysis in this chapter, I show that Kirchhoff approximation represents a more realistic and stable solution of the inverse problem compared with Born approximation, e.g. for the phase of supercritical angles.

In chapter (5), numerical example of FWI method using P-to-P and P-to-S synthetic and field data examples are presented. The examples are intended to show the efficiency of the method, problems in processing field data and suggest solutions for those problems.

In Chapter (6), I discuss the problems of the inversion using PSTM approximation and propose the solutions to improve it. Overall conclusion are presented in the last part of this chapter.

Chapter 2: Review of the iterative inversion method

2.1 Introduction

This chapter reviews the inverse problem for reflection seismic data. I start with an overview of the iterative least squares inversion. Then, I give a brief literature review of the inverse problem solution to seismic reflection data in relation to the iterative least squares method, referred to as the "FWI method". The inversion of the "full wavefield" is a difficult task. It would incorporate the solution of problem using a two-way wave equation forward model and migration operators. In present day applications, the "full wavefield" is included in the forward modeling operators and because of limitations in the imaging condition of the migration operators, the existing multiples in the data produce artefacts in the migration images. Moreover, current processing speeds constrain implementing the two-way wave equations inside the "FWI method" especially for 3D problems. Therefore, the one-way wave equation operators are used on data sets where multiples are removed.

Numerical comparison between PSDM and PSTM of diffraction data is included in this chapter. To conduct a numerical comparison, the Equivalent Offset Migration (EOM) method (Bancroft et al. 1998) is used for two reasons: first, the formulation of the Double Square Root (DSR) equation can be represented a single square root equation, making the mathematical expression of the diffraction traveltime into a simpler hyperbolic form. Second, the velocity analysis of Common Scatter Point (CSP) gathers in the EOM can be modified and implemented in the FWI approach (as shown in Chapter 3).

For an elastic medium, the Born approximation has played an important role in mathematical expressions of the FWI method. The last part of this chapter is about the Born approximation of the elastic wave equation. The focus will remain on the scattering potential of the P-to-P and P-to-S waves, as those wavefields are the main focus of multicomponent analysis.

2.2 Inverse problem by nonlinear least squares method

Let medium parameters are characterized by Lame´ parameters $\lambda(\boldsymbol{x})$, $\mu(\boldsymbol{x})$ and $\rho(\boldsymbol{x})$ which is function of subsurface points $\boldsymbol{x}$. The objective of seismic inversion is to obtain the earth model, $\boldsymbol{m}(\lambda,\mu,\rho)$, from the measured data, $\boldsymbol{d}$. The wave equation provides the relationships between model parameters, $\boldsymbol{m}$ and the measured waves, $\boldsymbol{d}$, at the receivers. We can approximate the seismic data, $\boldsymbol{d}$, from the forward modeling operator, f, on model parameters, $\boldsymbol{m}$, given by

$$f(\boldsymbol{m}_{true}) = \boldsymbol{d}_{true}. \tag{2.1}$$

Design of the forward operator, f, depends on the type of the waves to be investigated and the available computational power. We study the seismic traveltime, amplitude, and phase of the reflected wavefield, which the operator, f, can predict. In order to determine the physical properties of the subsurface, equation (2.1) is linearized, and then a direct inversion is used given by

$$\boldsymbol{m} = f^{-1}\boldsymbol{d}, \tag{2.2}$$

where f^{-1} is the inverse operator for f. If equation (2.2) is invertable, the solution is difficult for two main reasons. The first reason is that the model parameters are already embedded in f^{-1} and the relationship between seismic wavefield and the model parameters are nonlinear (Tarantola, 1984b, Virieux, 2009). A priori model, $\boldsymbol{m}_0$, cannot predict the true data, $\boldsymbol{d}_{true}$, as we have in general,

$$f(\boldsymbol{m}_0) \neq \mathbf{d}_{true}, \tag{2.3}$$

which creates the need for an iterative inversion. The second reason is that even if we assumed that this relationship is linear, then the inverse of f should be feasible and the computational time for f^{-1} is high (e.g., Pratt, 1999).

The objective of nonlinear inverse problem is to find a pair of $\boldsymbol{d}$ and $\boldsymbol{m}$ such that they have the closest distance to the pair of $\boldsymbol{d}_{true}$ and $\boldsymbol{m}_{true}$. The inverse of equation (2.1) is approximated using least square optimization approach. A misfit function, J, is defined by,

$$J = \frac{1}{2}\delta\boldsymbol{d}_k^{\,*}\delta\boldsymbol{d}_k, \tag{2.4}$$

where, $*$ denotes the adjoint operator , $\delta\boldsymbol{d}_k = \boldsymbol{d}_{true} - \boldsymbol{d}_k$ and the subscript k represents iteration number. From equation (2.4), the model parameter can be obtained by

$$\boldsymbol{m}_{k+1} = \boldsymbol{m}_k + \delta \boldsymbol{m}_k, \tag{2.5}$$

where, perturbation model vector $\delta \boldsymbol{m}_k$ is obtained by minimizing J function (Pratt, 1999,Virieux, 2009)

$$\delta \boldsymbol{m}_k = -\left[\frac{\partial^2 J(\boldsymbol{m}_k)}{\partial \boldsymbol{m}_k{}^2}\right]^{-1} \frac{\partial J(\boldsymbol{m}_k)}{\partial \boldsymbol{m}_k}. \tag{2.6}$$

Assuming the noise in the data are negligible, the gradient function $\frac{\partial J(\boldsymbol{m})}{\partial \boldsymbol{m}}$ is given by (Tarantola, 1984b)

$$\gamma = \frac{\partial J(\boldsymbol{m})}{\partial \boldsymbol{m}} = -[F^* \delta \boldsymbol{d}], \tag{2.7}$$

where F^* is the transpose of linear operator F as derivative f at point m given by

$$f(\boldsymbol{m} + \delta \boldsymbol{m}) = f(\boldsymbol{m}) + F\delta \boldsymbol{m} + o(\|\delta \boldsymbol{m}\|_2{}^2). \tag{2.8}$$

Although equations (2.4) to (2.7) are mathematical illustration of inverse problem. In this study, instead of forming matrix f and F^*, I used true amplitude Kirchhoff operator (Schleicher et al, 2007) for simulation of wavefield and migration / inversion for adjoint operator for F^*. As will be discussed in chapter 4, it requires a set of imaging and Amplitude versus Offset (AVO) inversion operators to produce gradient function γ. In addition, I assume that the measured data is complete, and for computational simplicity the operator $\left[\frac{\partial^2 J(\boldsymbol{m}_k)}{\partial \boldsymbol{m}_k{}^2}\right]$ is assumed to be scalar coefficient (see e.g., Nemeth et al., 1999). So, equation (2.6) reduces to

$$\delta \boldsymbol{m}_k \approx -\alpha_k \gamma_k. \tag{2.9}$$

where α_k is called step length in iteration k and the updating procedure uses the steepest decent method (Tarantola, 1984a). Note that linearized forward problem of (2.1) can be written as

$$\delta \boldsymbol{d} = \boldsymbol{d}_{true} - \boldsymbol{d}_0 = f\left(\boldsymbol{m}_0 + \delta \boldsymbol{m}\right) - f\left(\boldsymbol{m}_0\right) = f\left(\delta \boldsymbol{m}\right) = \mathrm{F}\,\delta \boldsymbol{m}, \qquad (2.10)$$

which infers that the inversion requires only one step to complete. In this study, I have used equation (2.10) to define the forward problem for seismic data using the first order Born approximation. However, the inverse problem is still non-linear for parametrization of input parameters. First, the operator, f and F^* are dependent on velocity model for traveltime and true amplitude approximations. Second, the forward modeling and inversion are based on the Kirchhoff approximation instead of the Born approximation that the forward modeling and migration/inversion operators are developed by AVO operators. The AVO operators dependent on the model parameters contrast across bedding interface. The average angles of reflected and transmitted waves create nonlinearity inside the linearized AVO operators (Innanen, 2012).

To reduce the computational burden for inversion of elastic properties from reflection data, the implementation of operators for f and F^* is reviewed upon the reflected waves, then the numerical aspects of PSTM method and PSDM method are studied.

2.3 Overview of inverse problem for seismic reflected data

Perturbation theory (see e.g., Morse and Feshbach, 1953) plays an important mathematical role in studying and understanding scattered waves. In essence, it finds the relationship between the difference of recorded wavefield d_{true} and modelled wavefield d_k, called the data residual δd, and the difference of their elastic properties, called perturbed model δm. Once the relationship is established, it performs the inversion of the perturbation from data residuals. In order to find a unique solution of the perturbed model, this method requires that the perturbation be small. As shown in equation (2.5), the inverted perturbed model is added to the initial background model to approximate the true solution.

In the framework of perturbation theory, several studies have linearized the nonlinear acoustic wave equation by Born approximation for direct inversion of subsurface properties. For example, Cohen and Bleistein (1979) used the Born approximation for direct velocity inversion of poststack data. Clayton and Stolt (1981) used Born and WKBJ approximations of prestack F-K migration for the direct inversion of density and bulk modulus. Beylkin (1985) presented a mathematical framework for migration/inversion of acoustic waves. Bleistein (1986) modified Beylkin's Born approximation of the forward problem using the Kirchhoff approximation. Bleistein (1986) showed that the amplitude of his inversion is the same as the angle-dependent geometric-optic reflection coefficient. Parson (1986) assumed that output of Bleistein's (1986) inversion is equivalent to the linearized reflection coefficient of Aki and Richard (1980) and showed the direct inversion of the relative change of elastic properties with a P-to-P survey. A major problem with a direct inversion method was that the inversion operators require reasonable a priori knowledge of the medium to produce accurate results. This created a need to iteratively update the inversion operators from the results of the previous steps.

Several authors addressed the iterative approach by the concept of nonlinear least squares for the inverse problem. In an acoustic Born approximation, Tarantola (1984) and later LeBras and Clayton (1988) showed that the inverse problem for linearized reflection data (i.e., multiple free) can be done using iterative use of F^* in the form of classical Kirchhoff migration and f in the form of Born forward modeling. Tarantola (1984b) provided an inversion strategy by iterative use of consistent f and F^*. Similar strategies were later presented for inversion of the elastic two-way wave approximation (Tarantola, 1986 and Mora, 1988). Gauthier el. al (1986) applied the numerical method of Tarantola (1984b) by FDTD operators to a synthetic data set.

Beylkin and Burridge (1990) derived f and F^* for the direct inversion of scattering potential of the Born approximation. From a numerical point of view, in order to include higher order terms to this approximation, one may implement two wave equation operators such as FDTD and RTM for f and F^* respectively. Numerically, the RTM approach creates artefacts due to the presence of multiples (Liu et al., 2011). It requires multiple prediction and elimination techniques as well as applying proper imaging condition since the crosscorelation of produced m-order multiples of forward propagation of the source with m- or less order multiples of backward propagated receiver data cannot produce a constructive image. Therefore, the multiple data are not imaged into the original reflectors only but also into different depth that downgoing and upgoing meet each other. A numerical example on this issue is presented in next section.

Besides FDTD, there were attempts to improve computational efficiency by implementing cheaper numerical schemes for forward modeling and migrations. Beydoun and Mendez (1989) and Jin et al., (1992) combined ray tracing and the Born approximation inversion of elastic waves for multiparameter inversion of elastic properties. The technique was used to reduce the computational cost associated with ray tracing and applied to a synthetic 3D survey on an SEG/EAGE overthrust acoustic model for velocity inversion (Thierry et al., 1999 , Lambare et al., 2003 and Operto et al., 2003). The results showed that asymptotic approximations are an efficient strategy in iterative inversion algorithms. Margrave et al., (2012) implemented one-way migration of Phase Shift Plus Interpolation (PSPI) approach for inversion and calibrated the inversion result with available control well similar to procedure of conventional impedance inversion.

Elimination of multiples is an essential part of current seismic processing schemes (e.g., Weglein et al., 1997, Verschuur and Berkhout, 2005, Hargreaves, 2006), so the computational cost of time-stepping methods for f and F^* can be reduced if replaced by ray based method. In areas with smooth lateral variation in elastic properties, the traveltime of events is approximate using the DSR equation of the PSTM method.

2.3.1 Direct inversion, perturbation and iterative inversions

Table 2-1 summarizes the relationship between direct inversion, perturbation and iterative inversion strategy. If f is a linear operator, the term $(f^* f)^{-1} f^*$ is known as least squares migration/inversion (Nemeth et al., 1999), which acts as an operator to map the data to its original scatter point. The general steps implemented in FWI methods are similar to the method of direct inversion, but the main difference is that we invert to get the model perturbation δm_k from the data perturbation δd_k (data residual). In addition all operator are updated in FWI approach. Use of equation (2.6) removes the need to find the scalar (step length α_k) to update the model parameters. Obtaining step length, α_k, requires performing the forward modeling, f_k, to test the misfit function of equation (2.4) such that minimum error in energy of the data residual is satisfied.

I performed a simple numerical simulation to illustrate the influence of model perturbation δm on data residual δd in perturbation theory as well as the inverse problem. I used the acoustic wave equation based on staggered grid, velocity-stress approach with Perfectly Matched Layer (PML) boundary condition (see e.g. Zhou, 2003) on all edges except the surface. The model is a 500×320

grid with grid spacing $D_x = 5$ m. A single source is in the middle of model at surface with all receivers at the top of the grid. The true, initial and perturbed velocity model is displayed in Figure 2-1. The simulated data are shown in Figure 2-2. As seen in true data, the perturbation δm influences the traveltime and amplitude and more reverberation of multiples compared to initial data. These changes are illustrated in the data residual panel which indicate the non-linear nature of wave equation operators. The corresponding RTM operator on the data residual is depicted in Figure 2-3. I used zero-lag crosscorrelation of the extrapolated source and receiver (e.g., Claerbout, 1985) and true velocity as an input. The non-linear behaviour of both forward source and backward receiver field creates artifacts in the image as both wavefields can meet each other on several places. Hence, both primary and multiple data are imaged in different position whereas only perturbation is expected to be imaged at depth ranges from 300 to 500 m. If we compare the image with AGC to one without AGC, most of these artefacts observed are small and ignored in many numerical studies. However, I emphasize that the type of imaging condition used in RTM requires modification to prevent wrong image of multiple data (e.g., Liu et. al., 2011) otherwise there is a need for preprocessing data sets by removing multiples. Additionally, if the input velocity model of RTM is smoothed then the imaging condition is similar to the first order Born approximation or simply on primary reflection data. Smoothing makes the reflectivity of subsurface smaller, the RTM output is created by imaging condition between only downgoing source and downgoing backpropagated receiver data which physically restricts the existence of two-way wave equations.

As shown in Figure 2-4 an iterative inverse problem typically uses a steepest descent algorithm with the following steps: 1) forward modeling: to evaluate the norm of data residuals obtained from updated model, i.e. δd to estimate the step length, α_k, and 2) inversion: using the migration/inversion operators on the data residuals to estimate gradient function, i.e. $\gamma = F^*(\delta d)$. The algorithm starts with simulating the initial model, which is close to the true model. The data residual is minimized by a series of iterations between migration of the data residual and forward modeling. The combination of the forward modeling and migrations are useful for both step length determination and inversion. More description of inversion operator is discussed in Chapter (4).

Table 2-1 Comparison of direct inversion and iterative inversion strategies in least square minimization using steepest descent method.

Direct inversion strategy	Iterative inversion strategy using perturbation theory
$f\mathbf{m} = \mathbf{d}$. Assuming linear operator	$f_k(\mathbf{m}_k) = \mathbf{d}_k$. (subscript k is iteration number)
$\mathbf{m} = (f^* f)^{-1} f^T \mathbf{d}$.	$\delta\mathbf{m}_k = (F_k^{\ *} F_k)^{-1} F_k^{\ *} \delta\mathbf{d}_k$, $\delta\mathbf{m}_k \approx \alpha F_k^{\ *} \delta\mathbf{d}_k$, Steepest descent method
$\mathbf{m} \approx \alpha f^* \mathbf{d}$.	$\mathbf{m}_{k+1} = \mathbf{m}_k + \delta\mathbf{m}_k$. One step if f is linear operator i.e. $f(\delta\mathbf{m}) = F\delta\mathbf{m}$, otherwise update the operator f_k and $F_k^{\ *}$ at each step .

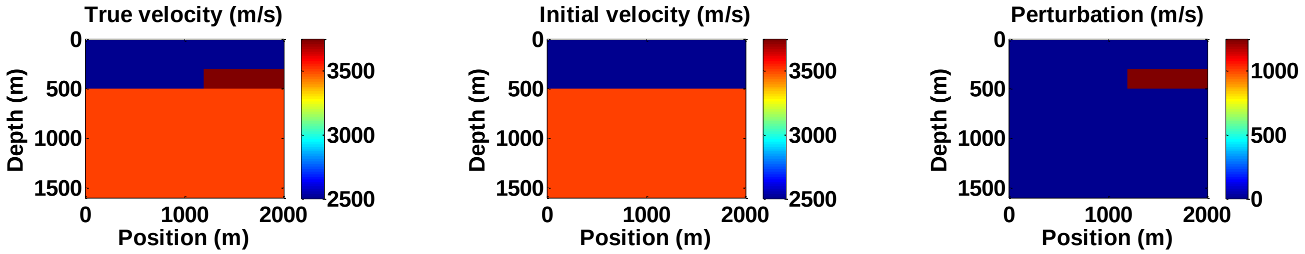

a) b) c)

Figure 2-1: General description of FWI in term of model perturbation. a) True velocity b) Initial velocity c) perturbation velocity.

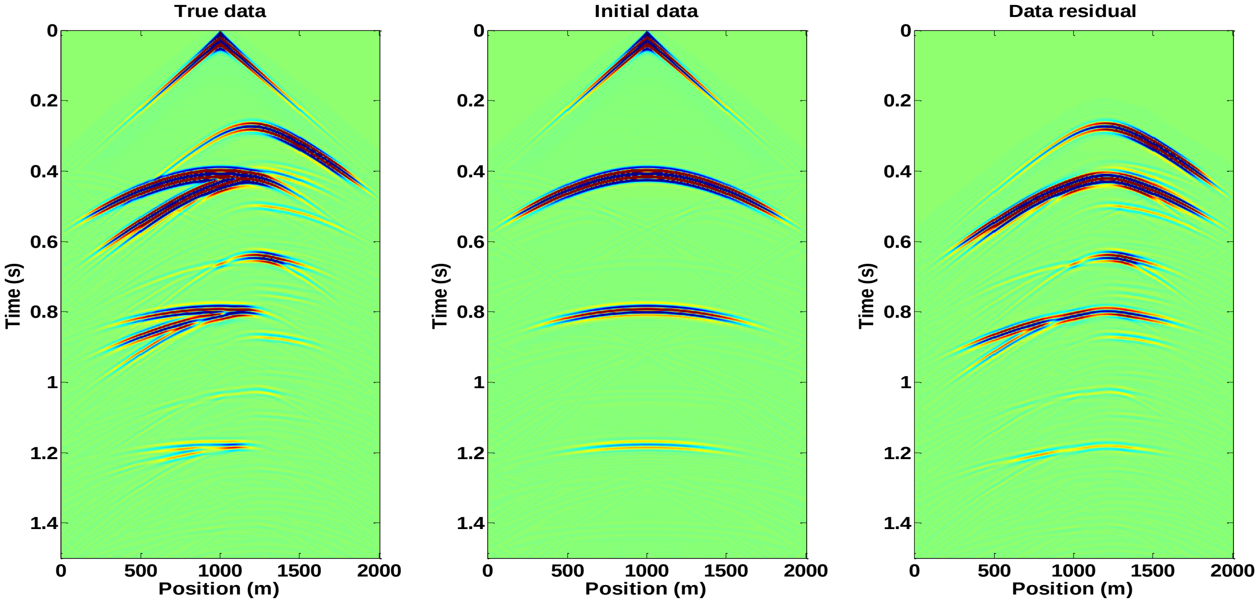

a) b) c)

Figure 2-2: General description of FWI in term of data residual. a) True data, b) initial data, c) data residual. The data residual illustrates the nonlinear behavior of wave equation in terms of traveltime, amplitude and multiple reflections due to perturbation.

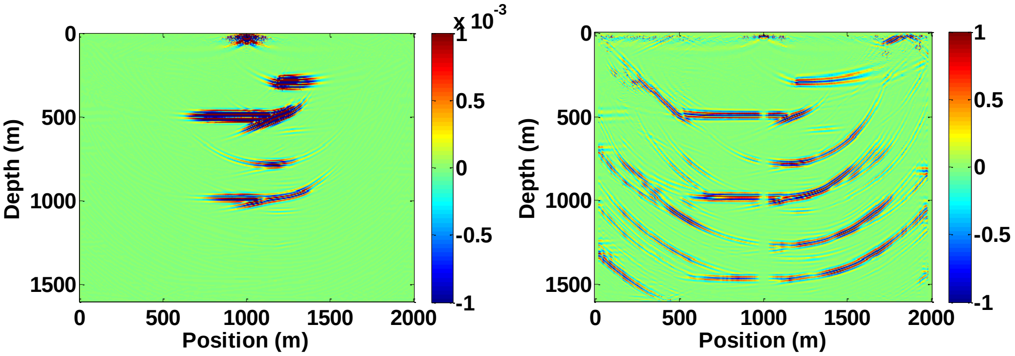

a) RTM image of true data using smoothed velocity. b) Applied AGC on (a)

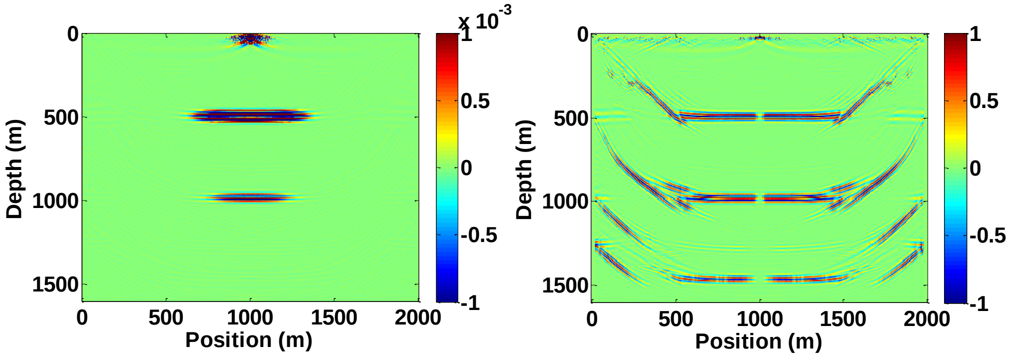

c) RTM image of initial data using smoothed velocity. d) Applied AGC on (c)

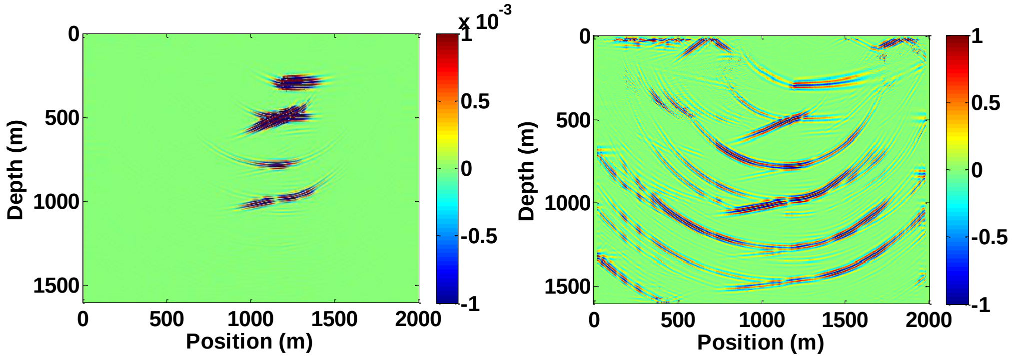

e) RTM image of data residual using smoothed velocity. f) Applied AGC on (e)

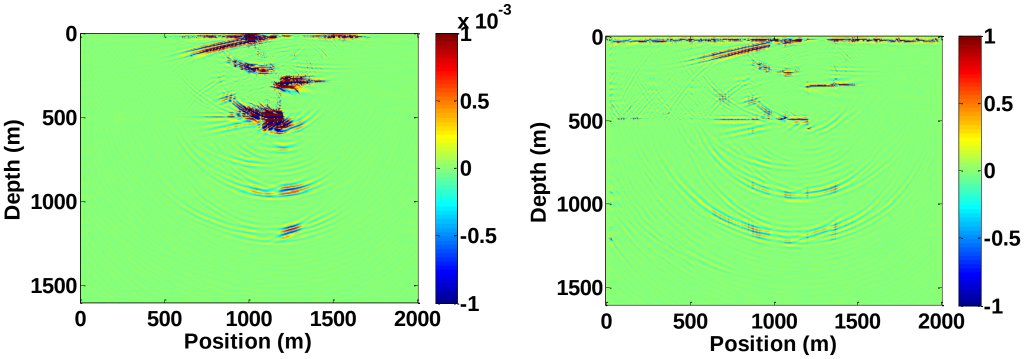

g) RTM image of data residual using true velocity. h) Applied AGC on (g)

Figure 2-3: General problem of RTM based in terms of input model and poor imaging condition for the full wavefield of Figure 2-2. Note the multiples are imaged in several depths.

2.4 Assumptions used

For a successful inversion the following assumptions are essential:

1- The source signature is known and can be removed from the data.

2- The wave equation explains all physics of the wave propagation from earth model.

The source can be thought of as causing pulses or disturbances in the medium. It has a range of frequencies which simultaneously oscillate and propagate through subsurface medium and are recorded at the receivers, in accordance to the wave equation. If the source signature is removed from the data, then the measured waves are predominantly reflectivity responses from changes in the earth elastic properties.

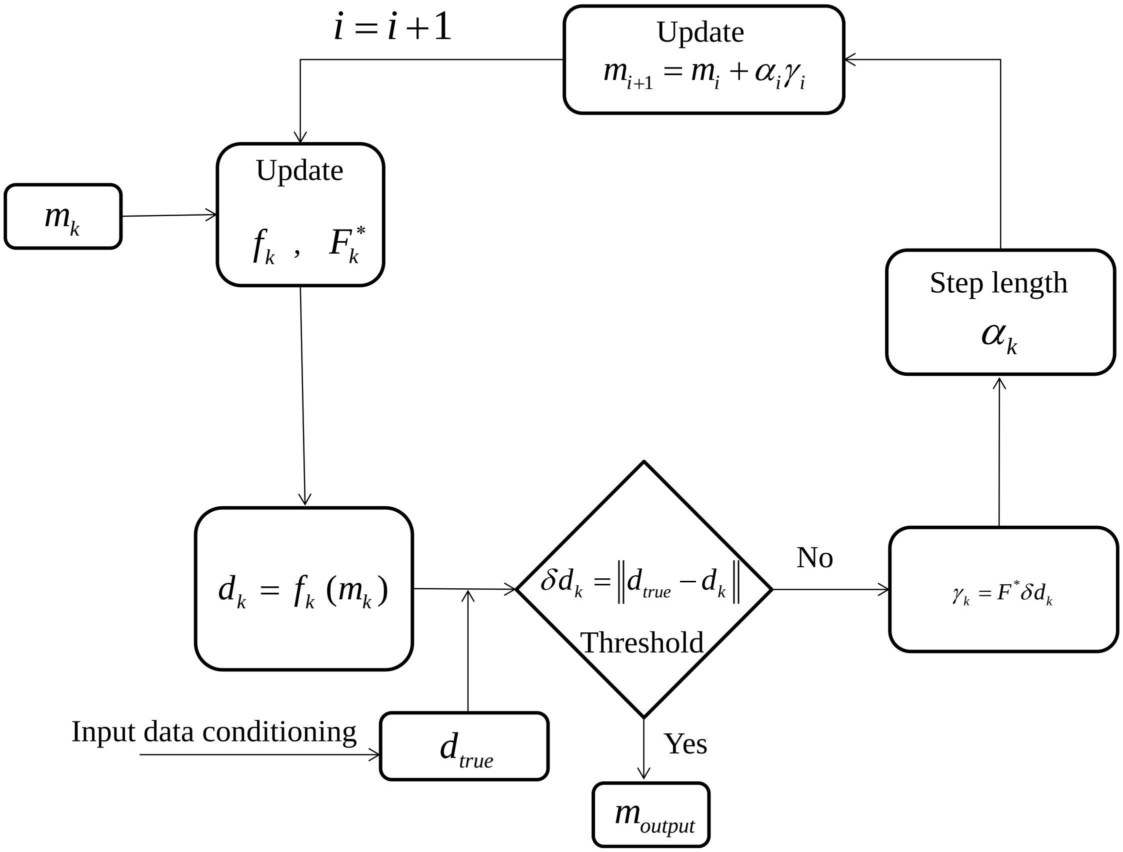

Figure 2-4: Simplified workflow for updating model $\boldsymbol{m}$ in steepest descent algorithm. The superscript F^* is the migration/inversion operator.

2.5 Numerical comparison of PSTM and PSDM approaches

In exploration seismology, it is assumed that depth migration gives more accurate images than time migration. Implementing depth imaging is a challenging task because of the computational cost and the need for a priori knowledge of velocity models. Time migrations have less computational costs but it cannot be as accurate as depth imaging for “complex models”. Complexity of the model can influence the ray path, and the traveltime of scattered waves. My goal is to mitigate the computational costs of FWI method for models that the performance of time migration is efficient. The comparison of the final images from depth and time migration has been published by several authors (see e.g., Claerbout, 1985). I use numerical examples to compare the consistency of three techniques of seismic modeling and imaging, namely, time migration, ray-based depth migration, and FDTD modeling methods. Figure 2-5 shows the Marmousi velocity model, which contains relatively high complexity in the middle of the model (i.e. 4500 - 6000m), but smooth lateral variations on both sides of the model. Figure 2-6 is the result of an RTM operator applied to its data. Given the Marmousi velocity as the input velocity model to RTM, most of the features of the model are constructed. Figure 2-7 shows the result of a PSTM operator on the same data set given the RMS velocity estimated from true velocity of the model. The coherency of the images along the smooth areas of the sides of the model is comparable to corresponding RTM image. The coherency is higher on the right side of the image because of the flat geological setting compared to dipping layers in the left side of the model. As shown in Figure 2-8, to compare the kinematics of the PSTM and RTM imaging methods, I compare the modeled scatter point response using a ray-tracing method with finite difference simulation. For illustration purposes both ray-traced data and finite difference data are mapped to a CSP gather, which is an intermediate PSTM gather of Equivalent Offset Migration (EOM) (Bancroft et al., 1998). The formation of the CSP gathers is based on the Prestack Kirchhoff Time Migration (PSTM) as the traveltime formulation of CSP gathers assumes a straight ray path. The primary application of the CSP gather is for velocity analysis from the hyperbolic travel time of the scatter points on a time section. Here, the modeling and migration processes of CSP gathers are illustrated to show the conditions where one can successfully reduce the computational effort commonly associated with depth migration. In Chapter (3), I show that the comparison between the PSTM and ray tracing modeling gives an intuitive insight to improve the coherency, as well to enhance the velocity analysis of the images under dipping layers (such as left side of Marmousi model) in PSTM.

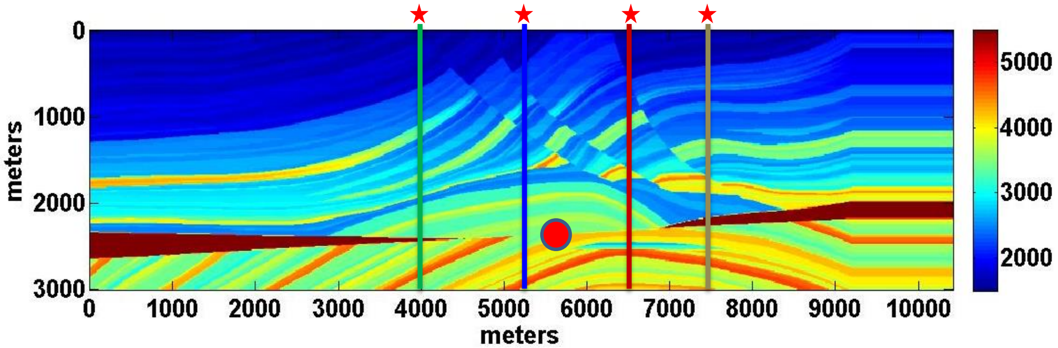

Figure 2-5: Marmousi model and the well location chosen for CSP analysis.

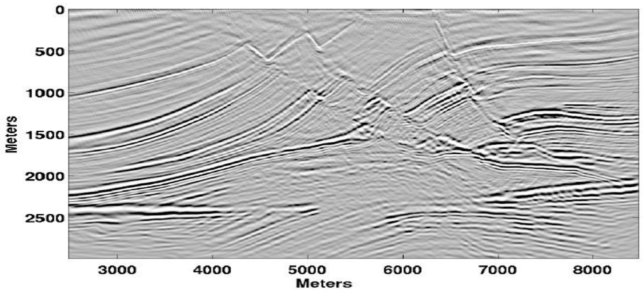

Figure 2-6: An image of the Marmousi data set using second order time and fourth order space explicit finite difference RTM. Image captured from Wards et al., (2008).

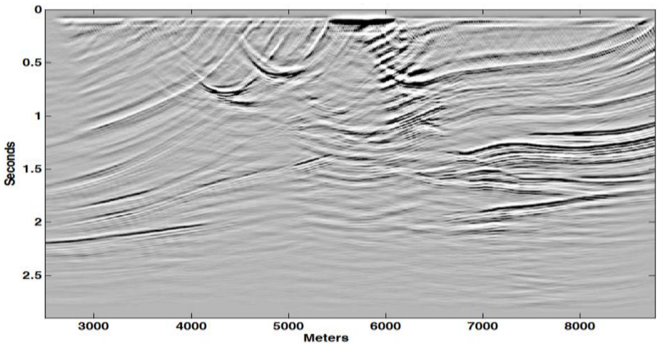

Figure 2-7: An image of the Marmousi data set using PSTM. The migration algorithm is based on the method of EOM.

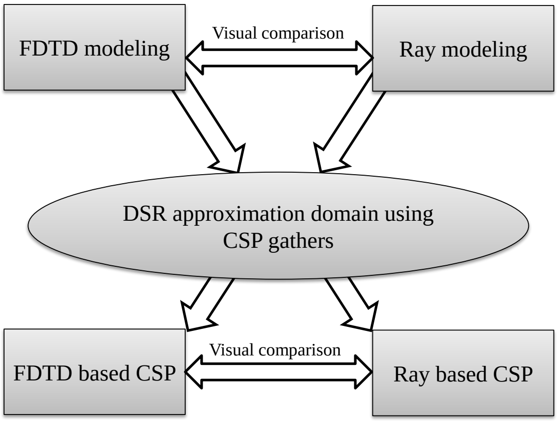

Figure 2-8: A general approach for optimizing imaging threshold of using PSTM instead of PSDM.

2.5.1 Scatter point response and Kirchhoff migration

Figure 2-9 shows the relationship between reflection and diffraction travel time surfaces in a common shot configuration. It shows that two scatter points R_1 and R_2 on the reflector surface create two diffraction curves which are tangent to the reflection travel time surface. The tangency between diffraction and reflection travel time surface is a constructive interference and is sometimes referred to as the stationary phase approximation (Bleistein, 2001). This is the basis for Kirchhoff migration algorithms (Claerbout, 1985, Yilmaz, 1987). The prestack Kirchhoff migration approach assumes the location of scatter points within the geological model, and then gathers all appropriate diffracted energies from all available input traces and relocates it to the position of the scatter points (Bancroft, et al., 1996).

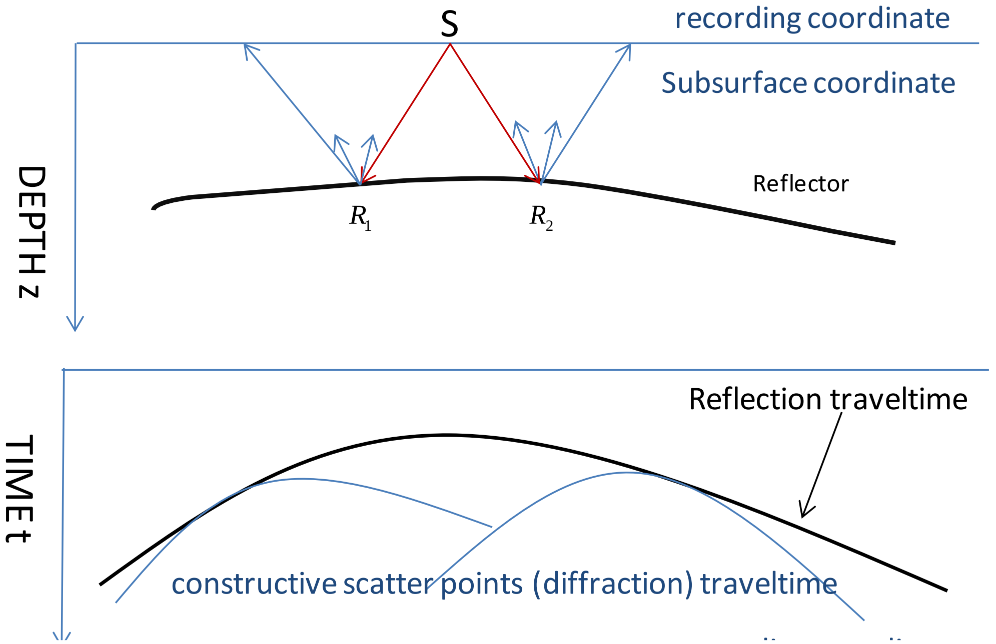

Figure 2-9: Relationship between the reflection and the diffraction travel time surfaces in a common shot configuration. Two scatter points in the subsurface have a constructive surface at the tangency point with reflection surfaces.

Figure 2-10 shows the relationship between FDTD-based techniques and the Kirchhoff approach using scatter point responses. In Figure 2-10a snapshot of the wavefield propagation after 1 s in a geological model is shown. The recorded wave field is shown in Figure 2-10c. Figure 2-10b shows a snapshot of the wave field at 1 s in the same model, but with seven scatter points instead of a continuous reflector. The reflected waves from the scatter points have a constructive surface at the reflection travel time. An increase in the number of scatter points can cancel the non-reflection part of the diffractions and construct the reflection data. Study of scattered waves from scatter points is the basis for study of reflection data. The complexity of models influence the traveltime of scatter points, hence the choice of forward modeling of reflection data and the migration is a challenging task. In the following, these challenges are illustrated using numerical examples.

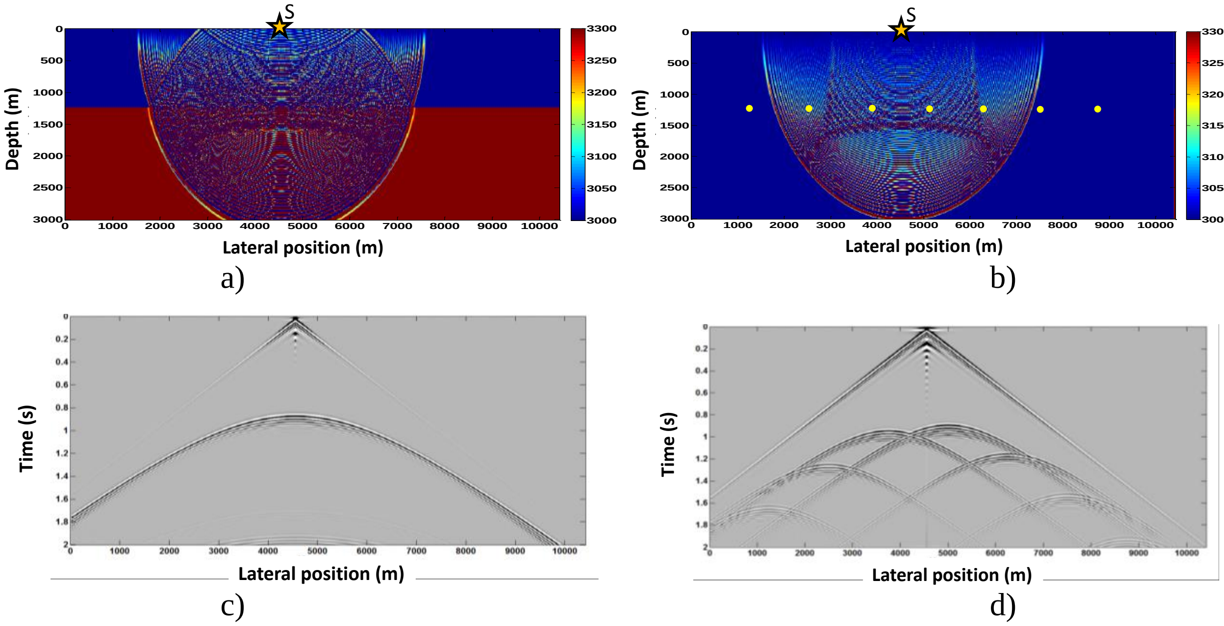

Figure 2-10: comparison of solution of wave equation using FDTD and scatter point response. a) A time snapshot at 1 s obtained from an acoustic FDTD response in a velocity model. b) A time snapshot at 1 s obtained from an acoustic FDTD response to scatter points instead of an interface. c) The recorded wavefield of (a) at the surface. d) The recorded wavefield of (b) at the surface.

2.5.2 Scatter point response and ray-based modeling

Prediction of the diffraction travel time response depends on waves propagating from source location S to the scatter point R, and from scatter point R to the receivers. In complex structures, prediction of diffraction travel time curves is a challenging problem that can be approximated by ray tracing methods. One of the concerns in the ray-based methods is that the fundamental assumption of the ray-tracing technique is based on the high frequency limit of wave. Therefore, to be able to model seismic signals by ray tracing, the spatial variation of velocity and its derivative should be small with respect to the wave length of the signal under consideration (Gray, 2000, Gajewski, et. al., 2002). This usually requires smoothing of the model. In data domain, the smoothing is a process which occurs in the propagation of real seismic waves, since the earth serves as a low pass filter during propagation (Gajewski, et. al., 2002). Thus an optimum smoothing of the velocity model is required to maintain consistency between the ray-based data and the real seismic data.

A scatter point located at coordinates (5500, 2450) m in the Marmousi velocity model (see Figure 5-2) is chosen as an example. This scatter point is located within a highly complex structure zone of the model. The following steps are performed in Figure 2-11:

1- Using the finite difference algorithm, three propagating wave fronts are computed from the scatter point for the times 0.3, 0.6 and 0.9 s. After applying a trapezoid band pass filter in the range of frequencies of (0, 10, 35, 55) Hz, they are overlain on the velocity field in Figure 2-11.

2- The wave fronts based on the traced rays initiated from the scatter point are constructed. Scatter point responses were modeled using rays that depart from the scatter point in different directions (i.e. at equal angles from -90 to +90 degrees with respect to the depth axis); then their travel times were recorded when the rays reach the surface.

3- The ray tracing process was done by applying Gaussian smoothing operators with lengths of 50, 150, 250 and 500 m to the reciprocal of the velocity model (i.e. 1/v). The grid size of the velocity model was 12.5 m in both depth and lateral directions.

Figure 2-11 compares ray-based travel times using four differently smoothed media. It shows that an optimum length of 250 m is obtained and that fluctuations of modeled travel times are less when compared to 50 and 150 m. Modeling with a large smoothing operator length of 500 m is not desirable because it causes a loss of accuracy in the velocity model and reduces resolution in the modeled travel time. Figure 2-12 shows only the constructed wavefronts using ray tracing. The recorded traveltime is displayed in Figure 2-13. The strong variations of traveltime in different smoothed models indicate that high frequency approximations of the wavefront are limited by the complexity of the models. In Figure 2-14, traveltime of the one-way diffraction curve is modeled using a 250 m smoothing length and overlain with the FDTD result. As shown, the diffraction of the FDTD method contains both primary and reverberations which is caused by nonlinearity of the two-way wave equations. The amplitude of multiple data are usually smaller than primary data because of subsurface reflections and propagations, otherwise elimination of multiples is a necessary part of migration and inversion using the one-way wave equation.

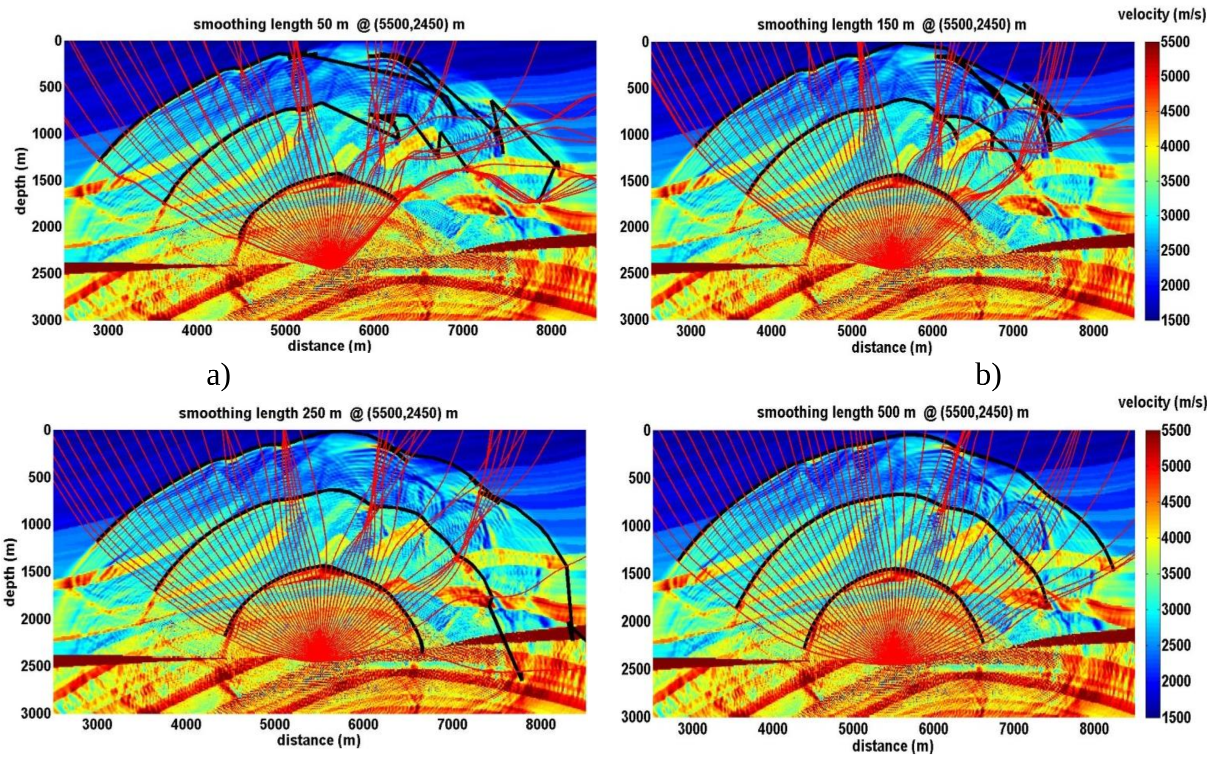

a) b)

c) d)

Figure 2-11: Comparison of wave field propagation modeling using FDTD and ray tracing approaches in several smoothed medium with a) 50 m smoothing length b) 150 m smoothing length c) 250 m smoothing length and d) 500 m smoothing length.

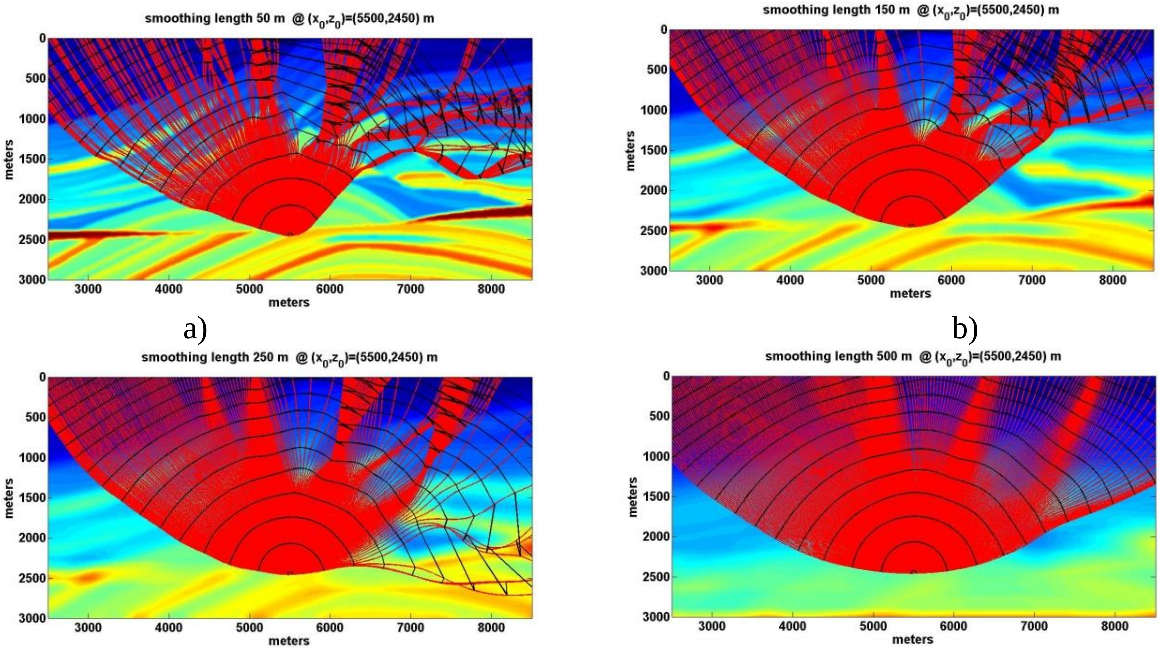

a) b)

c) d)

Figure 2-12: Wave field propagation modeling using ray tracing approach in several smoothed models with a) 50 m smoothing length b) 150 m smoothing length c) 250 m smoothing length and d) 500 m smoothing length.

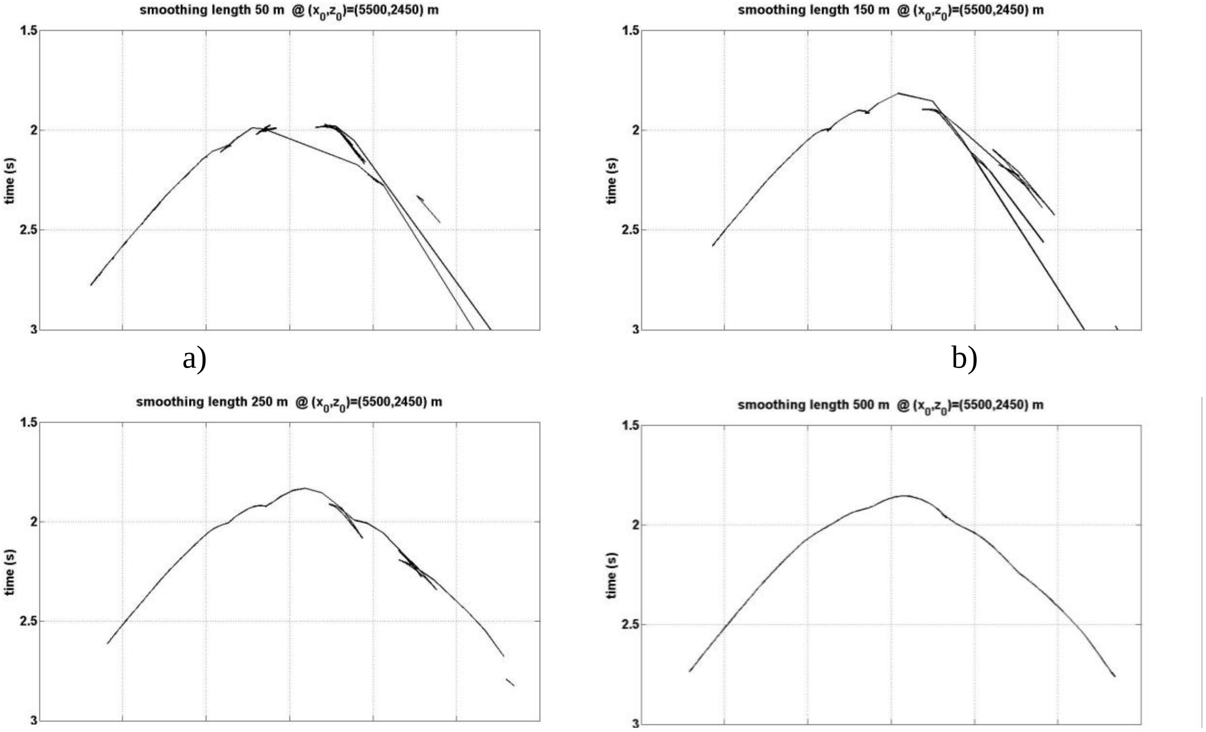

a) b)

c) d)

Figure 2-13: Travel time of recorded wave field at surface modeled using ray tracing in several smoothed media with a) 50 m smoothing length b) 150 m smoothing length c) 250 m smoothing length and d) 500 m smoothing length.

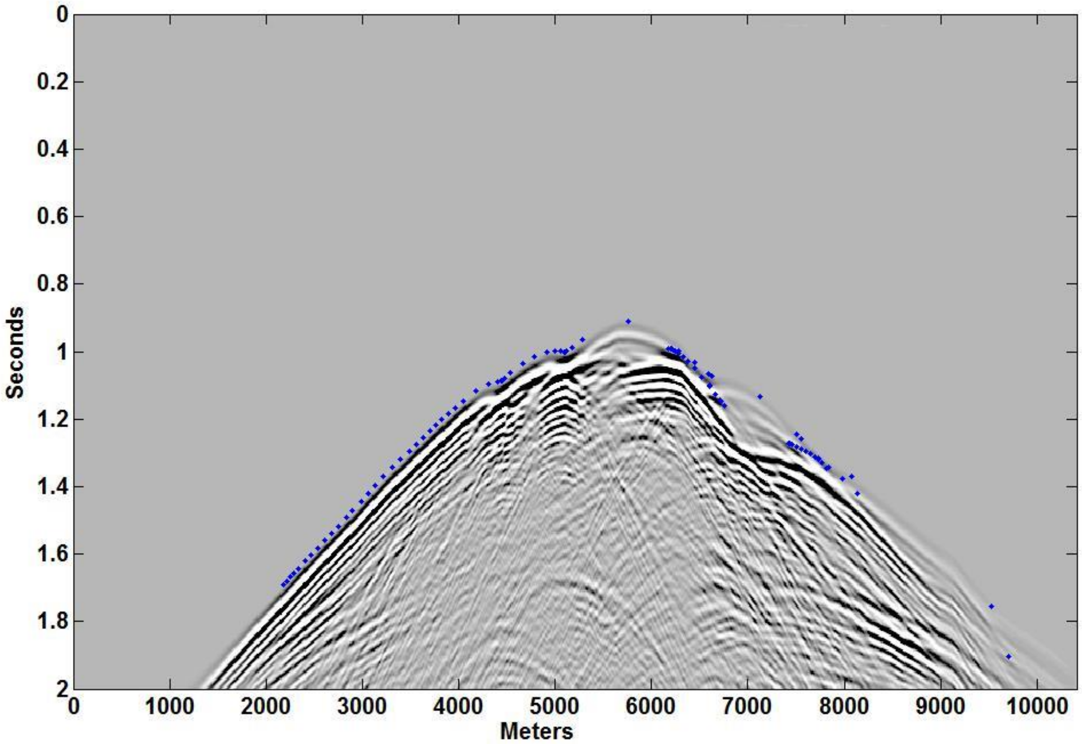

Figure 2-14: Comparison of ray tracing and FDTD. An optimum smoothing of 250 m for ray tracing is used.

2.6 DSR approximation and the CSP gather formulation

An example of the downgoing and upgoing rays and wavefronts are simulated over Marmousi 2-D velocity model. Assume that a model has negligible lateral velocity variation which is similar to having flat reflectors. In the general case where the subsurface velocity is varying smoothly, the Double Square Root (DSR) equation serves as a starting point for total travel time approximation in PSTM. This includes the time from the source to the scatter point plus the time from the scatter point to the receiver and is given from

$$t = \tilde{\phi}^P + \widehat{\phi}^P = \frac{\|\boldsymbol{x}_s - \boldsymbol{x}\|}{v} + \frac{\|\boldsymbol{x} - \boldsymbol{x}_r\|}{v}, \tag{2.11}$$

where $\tilde{\phi}^P$ and $\widehat{\phi}^P$ are traveltime of downgoing and upgoing P-wave respectively, $\boldsymbol{x} = (x, y, z)$ is subsurface coordinate, $\boldsymbol{x}_s$ and $\boldsymbol{x}_r$ are source and receiver coordinates. In 2D time migration it is expressed by (Yilmaz, 2001)

$$t = \sqrt{\frac{\tau^2}{4} + \frac{\left(x_m + h\right)^2}{v_m^2}} + \sqrt{\frac{\tau^2}{4} + \frac{\left(x_m - h\right)^2}{v_m^2}}, \tag{2.12}$$

where, τ is the zero offset two-way travel time, h_{offset} is the half source/receiver offset, x_m is the distance from the source/receiver midpoint to the lateral coordinate of the scatter point, and v_m is the migration velocity. The DSR equation can be simplified into different forms (Fowler, 1997). Bancroft et al. (1998) introduced Equivalent Offset Migration (EOM) as a PSTM method that transformed the DSR domain from $\left(x_m, h_{offset}, \tau\right)$ to an equivalent offset $\left(h_e\right)$ domain defined by:

$$h_e = \operatorname{sgn}\left(X\right)\left[x_m^2 + {h_{offset}}^2 - \left(\frac{2x_m h_{offset}}{tv_m}\right)^2\right]^{1/2}. \tag{2.13}$$

Here, the term Common Scatter Point (CSP) gather is used for the data mapped in h_e domain. Hence, the new travel time equation is hyperbolic and useful for velocity analysis (Bancroft et al., 1998, Margrave et al., 2001). Once the CSP gather is formed, to create a final migrated image, it only requires a NMO stacking path.

$$t = \left[\tau^2 + \left(\frac{2h_e}{v_m}\right)^2\right]^{1/2}. \tag{2.14}$$

Note that, if the geological model has a strong lateral velocity changes, equation (2.14) is not necessarily valid, but if it is valid, the travel time in equivalent offset domain will be aligned on a hyperbolic path. In Figure 2-15 the wavefront is originated from the source x_s in Marmousi velocity model. Three rays in blue color originated from the source and is close to scatterpoint R are illustrated. The scattered rays is illustrated in red color. Due to complexity of velocity models caustics are observed in this figure. Computation of both downgoing and upgoing waves are an essential task for seismic imaging problems. In the next section, this task is numerically studied using DSR approximation of CSP gathers.

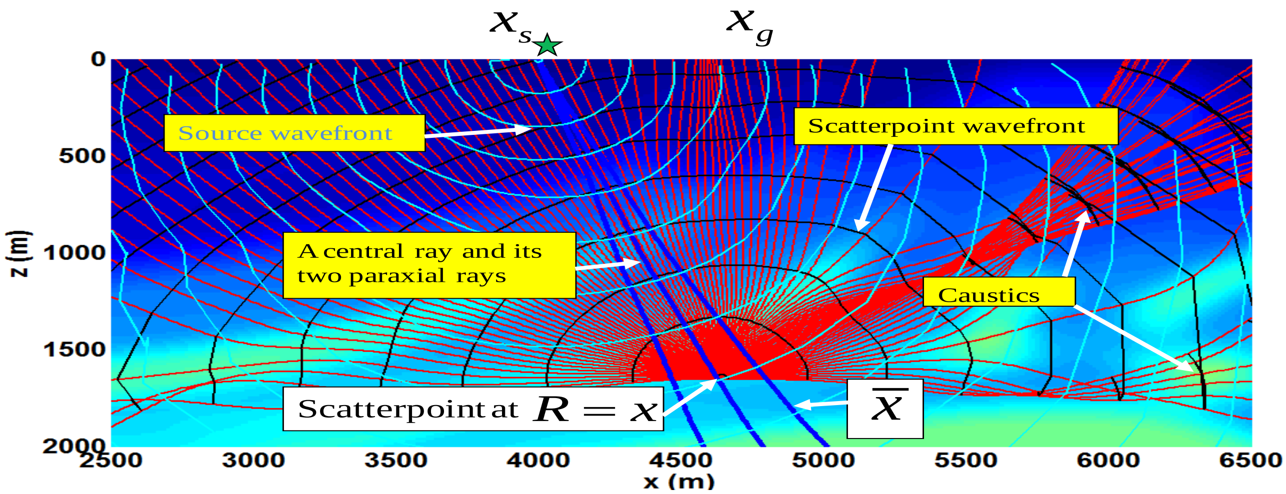

Figure 2-15: Simulation of the ray paths and wave fronts of a wave that initiates from a source then diffracts to the receivers. The velocity is taken from the Marmousi model and smoothed using 250 m smoothing operator. Note the behavior of the wave fronts and the resulting caustics that can influence the approximation of traveltime.

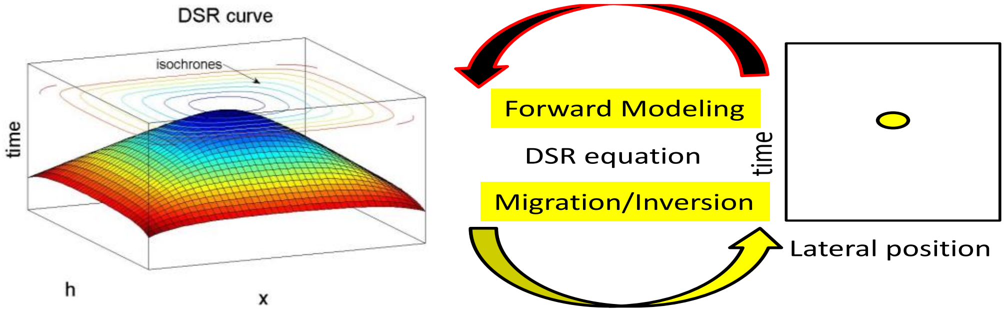

Figure 2-16: The relationship between the forward modeling of prestack volumes from DSR curve and the equivalent offset migration method. The scatterpoint response on the right side is mapped to the equivalent offset domain without traveltime shifting which makes the DSR to be aligned in a hyperbolic path.

2.6.1 Mapping the ray-tracing travel time into CSP modeling

The CSP gathers were simulated by converting the travel times of the scatter points to the equivalent offset domain of equations (2.13) and (2.14). If a scatterpoint is located in a constant velocity model, then the shape of diffraction energy from a scatter point is identical in all the shot records, but they have different arrival times due to the traveltime from the shot to the scatter point. For these models (having negligible lateral variation in velocity), all of the equivalent offset domain data lie on the hyperbolic NMO path; but in the case of strong lateral velocity variation, the definition of equivalent offset (i.e., the collocation of the sources and the receivers) is approximate and the event coherency is reduced. In fact two sources of error reduce the accuracy of forward modeling. The first is the travel time from scatter point to the receivers (see e.g., Figure 2-15) that determines the shape of diffraction curve as well as the effects of caustics. The second reason is the travel time to the scatter point from the sources.

To demonstrate the feasibility of the CSP modeling, the ray-tracing travel time with a 250 m smoothing operator is used. Figure 2-17a shows the modeled scatter point response from four different shot records are plotted on the receiver locations (i.e., stacked). In Figure 2-17b, the shot data are mapped to the equivalent offset domain located at the scatterpoint. Note the complex data tend to have hyperbolic shape in Figure 2-17b. In the left side of gather it has smaller fluctuation compared to the right side of the gather. Here, for observing the coherent event, the left side of the CSP gather is more reliable because of associated downgoing and upgoing rays traveled through less complexity of left side.

2.6.2 Coherency of image construction

To compare the diffraction curve of Figure 2-17 to FDTD data the following procedure is used. 50 shot records around the scatter point is chosen. Figure 2-18 to Figure 2-20 show the corresponding CSP gather. In these figures, the four scatter points are modeled and their travel times are plotted as blue dots. The Amplitude Gain Control (AGC) is applied to the gather for illustration. The amplitude differences of the two sides of the CSP gathers happen for two reasons. The first reason is because of the acquisition parameters: the survey was an “off-end” survey, with receivers to the left of the source. So, to the right of the sources, there is no receiver to record the scattered energies that arrives at the surface. The second reason is that the behaviour of wavefronts has significant impact on the amplitude. Because of the complex model, the rays and wavefronts experience more caustics (i.e., the rays cross) and shadow zones (i.e., the areas where the density of rays arriving at the surface is low) on the right side of the scatter points. Once the CSP modeling has been performed, we are able to compare it with the real data and then obtain an optimum fit between them. In general, it is expected that the DSR approximation of traveltime meets a threshold criteria in terms of smoothness and complexity of velocity model.

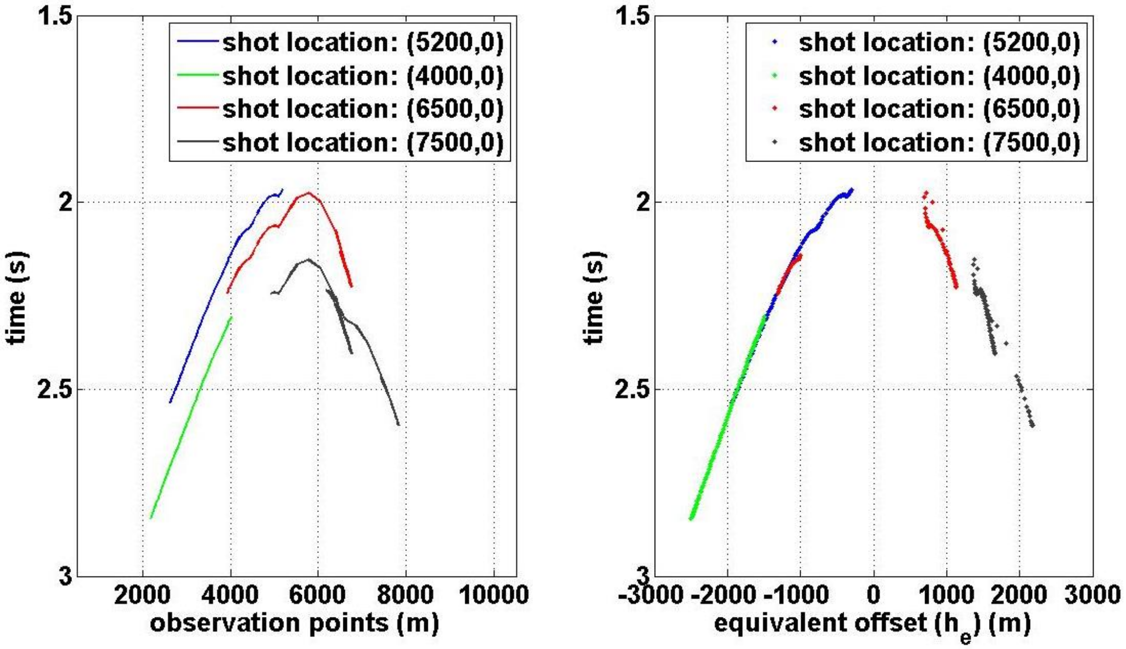

a) b)

Figure 2-17: CSP gather modeling in a complex structure. One scatter point response at (5500, 2450) m of the model in four shot records by (a) receiver location converted to (b) equivalent offset (h_e) domain at the scatterpoint location.

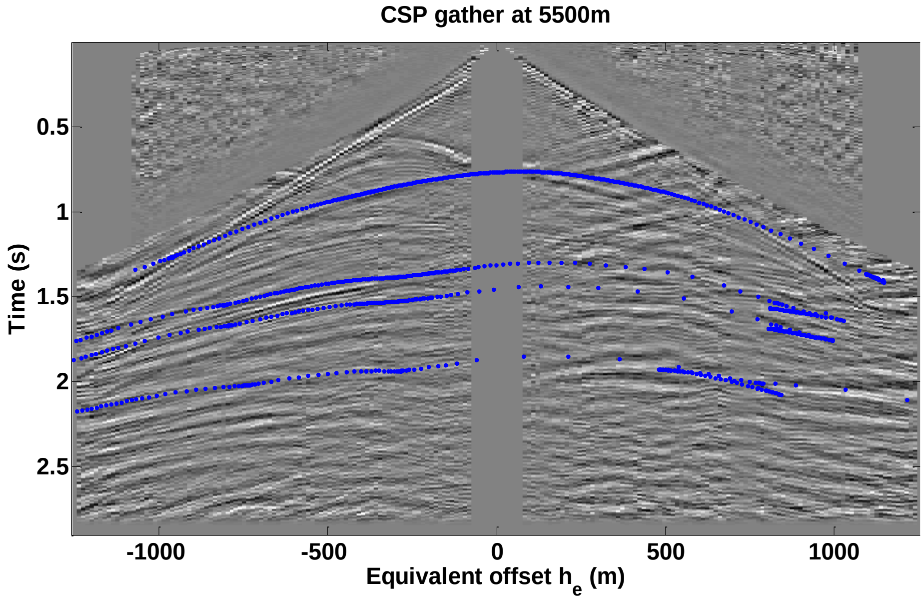

Figure 2-18: Modeled travel time and CSP gather formed at 5500 m from the left edge of the model. The blue travel time curves are computed from scatter points located at depths of 790 m, 1550, 1755 and 2450m.

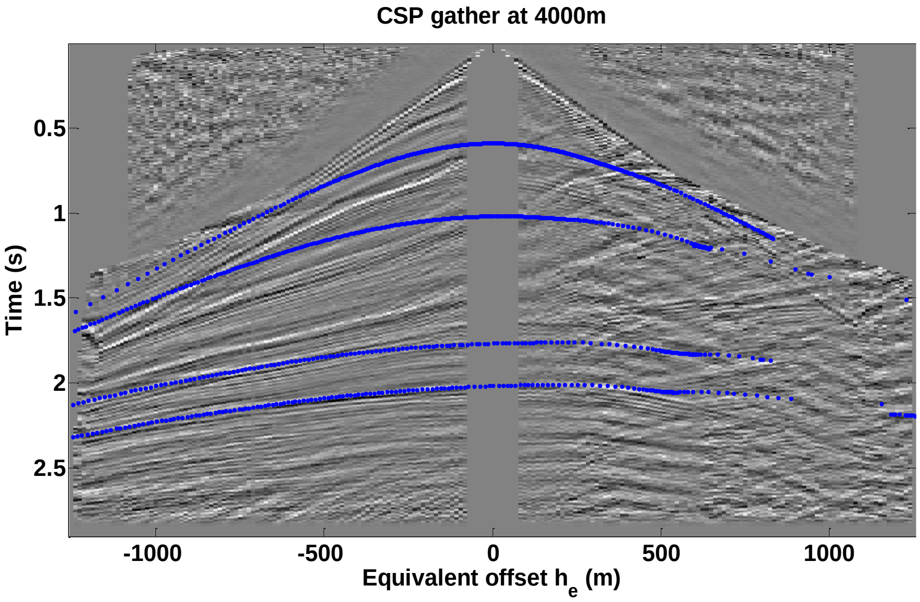

Figure 2-19: Modeled travel time and CSP gather formed at 4000 m from the left edge of the model. The blue travel time curves are computed from scatter points located at depths of 500 m, 950 m, 2000 m and 2335 m.

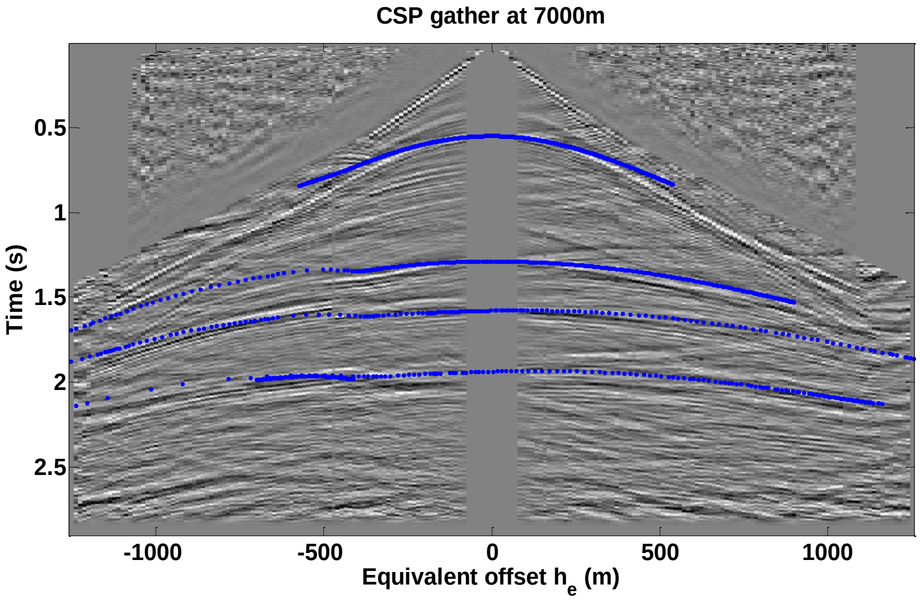

Figure 2-20: Modeled travel time and CSP gather formed at 7000 m from the left edge of the model. The blue travel time curves are computed from scatter points located at depths of 470 m, 1335 m, 1800 m and 2320 m.

2.7 Born approximation and scattering potential of elastic waves

After the illustration of traveltime in previous sections, the amplitude of the waveform is discussed in following section. The formulation is primarily based on the insightful paper of Beylkin and Burridge (1990) on the subject of perturbation theory for the derivation of a scattered wave field in an elastic medium. Figure 2-21 shows a continuous elastic model that contain particles connected to each other through springs. Each particle has a mass and every springs responds to both compression and shear stress imposed to the model by Lame´ constant.

The equation of motion in an elastic solid is governed by the coupling of the elastic stress-strain relationship (i.e., Hook's Law) and Newton's second law in the following forms

$$\rho\ddot{u}_i - (c_{ijkl}u_{k,l})_{,j} = 0, \tag{2.15}$$

where $u_i = u_i(\boldsymbol{x},t)$ is the ith component of the displacement vector, $\rho = \rho(\boldsymbol{x})$ is the density $c_{ijkl} = c_{ijkl}(\boldsymbol{x})$ are the elastic constants of the medium at the point $\boldsymbol{x} = (x_1, x_2, x_3)$. In equation (2.15) the superscript "$\ddot{\ }$" stands for $\partial^2/\partial t^2$ and "$, j$" for $\partial/\partial x_j$ and a repeated index implies summation with respect to this index. Obtaining the elastic constants c_{ijkl} of the medium and the density ρ is the objective of the inversion.

In general form, they can be represented by their perturbed quantities and a reference medium

$$\left(c_{ijkl}(\boldsymbol{x})\right)_{true} = \left(c_{ijkl}(\boldsymbol{x})\right)_0 + \delta c_{ijkl}(\boldsymbol{x}), \tag{2.16}$$

where δ represents a small perturbation. Similarly, for ρ we have

$$\rho_{true}(\boldsymbol{x}) = \rho_0(\boldsymbol{x}) + \delta\rho(\boldsymbol{x}), \tag{2.17}$$

where the subscript `true` refers to the true model to be found and the subscript `0` refers to the initial model to be updated. Other formulations of the perturbation of model parameters are available. For example, the true elastic property $\boldsymbol{m}_{true}(\lambda_{true}, \mu_{true}, \rho_{true})$ can be decomposed into an initial model $\boldsymbol{m}_0(\lambda_0, \mu_0, \rho_0)$ and a perturbation $\delta\boldsymbol{m}(\delta\lambda, \delta\mu, \delta\rho)$.

The components of $\boldsymbol{m}_{true}(\lambda_{true}, \mu_{true}, \rho_{true})$ are given by

$$\lambda_{true}(\boldsymbol{x}) = \lambda_0(\boldsymbol{x}) + \delta\lambda(\boldsymbol{x}),$$
$$\mu_{true}(\boldsymbol{x}) = \mu_0(\boldsymbol{x}) + \delta\mu(\boldsymbol{x}),$$
$$\rho_{true}(\boldsymbol{x}) = \rho_0(\boldsymbol{x}) + \delta\rho(\boldsymbol{x}). \qquad (2.18)$$

where $\lambda(\boldsymbol{x})$ and $\mu(\boldsymbol{x})$ are elastic constants of stiffness tensor of the model c_{ijkl}. In Born approximation, initial model has the low frequency component of the true model and is assumed to be close to the true model. The variable $\boldsymbol{x} = (x, y, z)$ is the subsurface coordinate. The terms $\delta\rho$, $\delta\lambda$ and $\delta\mu$ are the perturbations of the elastic properties which contain the higher frequencies of the true model, and in our problem are assumed to generate the perturbation of the total scattered elastic wavefield $\delta d\left(\boldsymbol{x}_s, \boldsymbol{x}_r, t\right)$ from the medium. The variable $\boldsymbol{x}_s$ and $\boldsymbol{x}_r$ are the source and receiver locations. It is assumed that the traveltime of the wavefield traveling through the initial model is close to the true model.

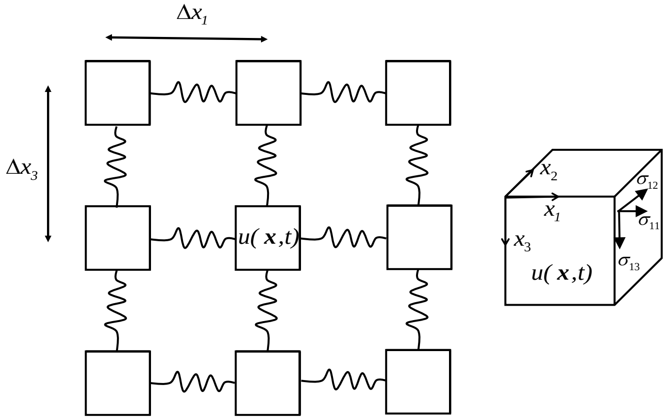

Figure 2-21: General description of elastic medium and equation of motion. The left 2D network correspond to the displacement $u(\boldsymbol{x},t)$ in (x_1,x_3) plane. The right cube is the particle model.

The time-harmonic scattered wave field at the receiver $\boldsymbol{x}_r$ from a volume of scatterers D, embedded in a background medium characterized by equation (2.15) is given by

$$\delta d_{jk}(\boldsymbol{x}_s, \boldsymbol{x}_r, t) = -\int_D \left[\delta\rho \partial_t^2 \tilde{G}_{jl} *_t \hat{G}_{kl} + \delta c_{lmpq} \tilde{G}_{jp,q} * \hat{G}_{kl,m} \right] d\boldsymbol{x}, \qquad (2.19)$$

where, signs "$\tilde{G}$ " and "$\hat{G}$ " refers Green's function for the downgoing and upgoing waves, "$*_t$ ' denotes convolution in time, and the subscripts jk refers to the displacement in the $k-$direction due to a point force in the $j-$direction. Equation (2.19) is the basis for scattered elastic waves that needs a Green's function, G, to describe different wave types. The total scattered wavefield, δd_{jk}, is the superposition of conserved and converted waves as follows

$$\delta d_{jk} = \delta d_{jk}^{PP} + \delta d_{jk}^{PS} + \delta d_{jk}^{SP} + \delta d_{jk}^{SS}. \tag{2.20}$$

In 3D models, δd_{jk}, consists of nine components which are the result of combining the three components from the acquisition source with three components receivers. Although the inversion approach presented here is applicable to all wavefields in equation (2.20), due to the low Signal to Noise Ratio (SNR) of the amplitude information observed in the used field data and the acquisition source type deployed, in this study the wavefields δd_{jk}^{SP} and δd_{jk}^{SS} have been ignored. In addition, for analysing P-to-P and P-to-S data with an eighteen components resultant wavefield, two configurations of the vertical component source for vertical (for P-to-P wavefield) and radial components (for P-to-S wavefield) are considered.

Generally, the single scattered wavefield components of elastic waves can be expressed by (Beylkin and Burridge, 1990)

$$\delta d_{jk}^{IR} = -\partial_t^2 \int S_{lm}{}^{IR} A_{jl}^{I} A_{km}^{R} \delta(t - \phi^I - \phi^R) d\vec{x}, \tag{2.21}$$

where, S_{pl}^{IR} is the scattering matrix, the superscript I and R are related to incident and reflected waves. The parameters A_{ij} and ϕ are the amplitude and travel time terms respectively which characterizes the Green's function by

$$G_{ij} = A_{ij}\delta\left(t - \varphi\right). \tag{2.22}$$

Additionally, the parameters A and ϕ satisfy the transport and Eikonal equations derived for a specific type of wave. For example for incident P-wave it is defined as $A_{jl}^{I} = h_l{}^{I} A_j{}^{I}$ and $A_{km}^{R} = h_m{}^{R} A_k^{R}$ with h the polarization unit vector then the equation (2.21) changes to

$$\delta d_{jk}^{PP} = -\partial_t^2 \int S^{PP} A_j^{I} A_k^{R} \delta(t - \phi^{IP} - \phi^{RP}) d\,\boldsymbol{x}, \tag{2.23}$$

where, S^{PP} is defined as

$$S^{PP} = \rho^0 \left(\frac{\delta\lambda}{\lambda + 2\mu} + \frac{\delta\rho}{\rho} \cos\theta^{PP} + \frac{2\delta\mu}{\lambda + 2\mu} \cos^2\theta^{PP} \right), \tag{2.24}$$

Generally, the derived angle-dependent scattering potentials, S, has the form

$$S^{IR}(x) = h_k^I S_{ki}^{IR} h_i^R, \tag{2.25}$$

where, h refers to polarization vector, and S_{ki}^{IR} is defined as (see e.g., Ursin and Tygel, 1997)

$$S_{ki}^{IR} = \frac{\delta\rho(x)}{\rho_0(x)} \delta_{ik} + \frac{\delta c_{ijkl}(x)}{\rho_0(x)} p_j^R p_l^I, \tag{2.26}$$

where p is slowness unit vector parallel to the path of the rays. In Figure 2-22, a downgoing plane wave with frequency ω, traveling with velocity v_i in direction of its wavenumber vector, $k_i = \omega\hat{k}_i / v_i$, incident on a scatter point. The scattered waves travel with velocity v_r in direction of wavenumber, $k_r = \omega\hat{k}_r / v_r$. The reflecting surface Σ has normal vector in direction of $\vec{n} = \frac{k_r - k_i}{|k_r - k_i|}$. In Figure 2-2, the wavenumber k_i^P corresponds to incident P-wave, k_r^P and k_r^S correspond to scattered P- and S-waves respectively. The opening angles θ^{PP} and θ^{PS} are defined by $\theta^{PP} = \theta^i + \theta^P$ and $\theta^{ps} = \theta^i + \theta^s$, where angles θ^i, θ^P and θ^S are incident, scattered P-wave and scatterd S-wave angles respectively.

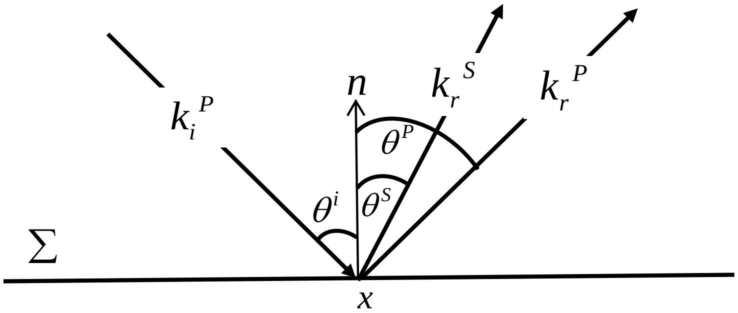

Figure 2-22: Beylkin and Burridge's (1990) elastic Born approximation angles. The reflection surface is shown by Σ (Modified from Stolt and Weglein, 2012).

Equation (2.26) is a general description of scattering potential for the various types of waves. Coupling the definition of the stiffness c_{ijkl} for as particular model (e.g. elastic, isotropic and anisotropic), the slowness, p, as well as the polarization vectors, h, of the incident and scattered waves have been the basis for modeling and inversion from the amplitude radiation patterns of the wavefields (Shaw and Sen, 2004). The derived angle-dependent scattering potentials of S^{PS} from Beylkin and Burridge (1990) are, in terms of Lame's constants, expressed in equation (2.26) and given by

$$S^{PS}(\Delta\mu, \Delta\rho) = \rho^0 \left(\frac{\delta\rho}{\rho} \sin\theta^{PS} + \frac{\delta\mu}{\mu}\frac{v_S}{v_P} \sin 2\theta^{PS} \right). \tag{2.27}$$

For an isotropic model, one can change the variables of the scattering potential of (2.31) to the perturbation of P-wave velocity v_P and S- velocity v_S by combining Snell's law with the differential operator for first derivative along bedding interface, Δ, as follows,

$$\Delta\lambda = \Delta(\rho {v_P}^2 - 2\rho {v_S}^2), \tag{2.28}$$

$$\Delta\mu = \Delta(\rho {v_S}^2), \tag{2.29}$$

to get

$$S^{PP}(\Delta v_P, \Delta v_S, \Delta\rho) = \rho \left(2\frac{\Delta v_P}{v_P} - 4k^2 \sin^2\theta^{PP} \frac{\Delta v_S}{v_S} + \left(2\cos^2\theta^P - 4k^2 \sin^2\theta^P \cos^2\theta^P \right) \frac{\Delta\rho}{\rho} \right). \tag{2.30}$$

A similar equation exists for S^{PS}

$$S^{PS}(\Delta v_S, \Delta\rho) = \rho \sin\theta^{PS} \left(\left(4k\cos\theta^P \cos\theta^S - 4k^2 \sin^2\theta^P \right) \frac{\Delta v_S}{v_S} + \left(1 + 2k\cos\theta^P \cos\theta^S - 2k^2 \sin^2\theta^P \right) \frac{\Delta\rho}{\rho} \right), \tag{2.31}$$

where $k = v_S / v_P$ (e.g. Mora, 1987 and Jin et al., 1992) . Applying the differentiation operator, Δ , and the Snell's law infer that the boundary across bedding interfaces are used on scattering potential. As shown in equation (2.19) the perturbation of elastic properties act as a virtual source in the model when the integration is on the scattering volume D. For considering the layer boundary, while the Born approximation is useful but the Kirchhoff approximation is a better alternative. In wave equation the boundary conditions plays an important role in characterizing the wave propagation, e.g., Snell’s law and reflection. Numerically this problem is illustrated in Figure 2-2 where a bottom and top of non-smoothed perturbation creates the reflection and transmissions. In chapter (4), the scattering potential from equations (2.30) and (2.31) are analytically compared to the Aki and Richard (1980) reflectivity functions. The boundary condition associated with Aki and Richard (1980) is based on layer boundary which is consistent with Kirchhoff approximation. In an iterative scheme the linearized AVO operators are used for both the forward modeling and inversion algorithm to provide the solution of a more realistic problem if compared to the Born approximation.

It should be noted that the source signatures are absent here, but in practice appropriate phase corrections and deconvolution schemes can be employed to remove the effects of the source. More details about these steps are provided in chapter 5 where I go through numerical field data examples.

2.8 Conclusions

The objective of this chapter is to visualize the numerical calculations of the estimated travel times by seismic modeling and imaging using Kirchhoff time migration, Kirchhoff depth migration, and FDTD methods. I enumerate the following limitations and advantages of Kirchhoff-based methods:

1- The assumption of high frequency on which ray theory modeling requires the grid size to be sufficiently small to accurately calculate the velocity gradient perpendicular to bedding interfaces (Wilson et al., 2010).

2- Optimum smoothing is an alternative procedure to alleviate the computational costs of the fine grids. It requires comparing the true data which contain band-limited frequency data with modeled data obtained from the ray-based method.

3- The PSTM one-way wave modeling and migration algorithms assume the straight ray path approximation. This creates restrictions in terms of accurate angle of incidence and multiple predictions, both of which influence the amplitude calculation.

4- Most of current standard processing methods are based on one-way solutions of the wave equation. As such, various multiple elimination, well log and VSP data calibration techniques have been made available to help processors account for the errors that result from multiple prediction and elimination to get true amplitude calculation. Hence, assigning the one-way operators for forward modeling and inversion is reasonable approximation.

5- In the FWI algorithm, the method requires an iterative use of forward modeling and migration. The advantage of ray-based methods is the lower computational cost and readily available software for commercial processing, compared to more expensive two-way operators such as FDTD methods.

6- I used CSP gathers to compare the numerical implementation of PSTM and PSDM with complex and smoothed structures. The method of FWI using PSTM is fast compared to the corresponding PSDM technique in forward and inverse iterations; however, since we are doing time migration, we are limited to models with moderate complexity.

7- The Born approximation has played an important role in designing the inversion of elastic properties. The formulation of the Born scattering potential is discussed here and in Chapter (5) and will be compared to the Kirchhoff approximation. The Born approximation is based on the perturbation of stiffness tensors δc_{ijkl} and density $\delta\rho$ for the particles which is desired to be inverted given data residual δd . The problem with Born approximation is that once the perturbation is added to the continuous elastic medium, it acts as body of the model and its boundaries with surroundings creates additional reflection and transmissions. This problem is illustrated in numerical example of Figure 2-2 . It shows that the top, bottom and edges of perturbation can also create scattering. An alternative formulation is surface integral Kirchhoff approximation which is based on perturbation of δc_{ijkl} and density $\delta\rho$ along the reflection surface. The approach is similar to linearization of reflectivity function of Aki and Richard (1980) that in Chapter (5) I will use it for iterative inversion.

Chapter 3: P-to-P velocity inversion in acoustic approximation

3.1 Introduction

I illustrate that PSTM and forward modeling can be implemented within the framework of iterative inversion schemes for models with smoothed lateral variation in elastic properties. This chapter is motivated by the formulation of DSR equation in CSP gather of Equivalent Offset Migration (Bancroft et. al., 1998) as a time imaging approach for P-to-P data and the associated technique for extracting the velocity information. The objective of this chapter is to enhance the inversion of velocity of CSP gathers using two strategies. The first strategy is to use only traveltime information to form the CSP gather. I include the influence of tilt for models with dipping interfaces to enhance the velocity inversion and to improve the image of migration result. This approach provides the low frequency component of geological models which can be used as an initial model for FWI methods (see e.g., Tarantola, 1984b). The second strategy is to implement and describe the FWI scheme using the PSTM and corresponding forward modeling. The result of the inversion provides the higher frequency component of subsurface compared to conventional CSP gather velocity analysis.

3.2 Enhancing the inversion of PSTM velocity by correction of tilt effects in CSP data

In this part, I show that the travel time response of scatter points beneath a dipping interface experiences an additional linear time shift proportional to offset. This shift happens because the rays bend as a consequence of velocity change. The normal hyperbolic shape of travel time in CSP gathers becomes tilted and causes inaccuracy in velocity analysis, since the right- and left-sided CSP gathers demonstrate different velocities in semblance plots. We improve the focusing of the separated energy in the semblance plots by removing the tilt effects. As a result, the accuracy of migration velocity inversion is enhanced and the focusing of the output image of time migration is improved.

3.2.1 Tilt and linear time shifts

The problem of lateral velocity variation for mispositioning of the apex of scatter point responses (diffraction curves) in PSTM has been analytically addressed by Black and Brostowski (1994). They derived a system of equations by analyzing the ray path geometry of image rays. Here, we approach the problem by geometrical analysis of the rotation of the velocity model toward the angle of the bedding interface and its wavefront.

Figure 3-1 shows a simple model with a horizontal interface that separates two layers with two different velocities. Wavefront propagation from the scatter point **R** at 4000 m from the left edge of this model and at a depth of 2500 m is simulated by connecting the isochrones of traced rays. Note that the wave front time interval is constant. To simply show the possible response from a scatter point **R** beneath the dipping interface with dip angle of β, Figure 3-1 is rotated by β degrees counterclockwise, as depicted in Figure 3-2. Consider two receivers a and b in Figure 3-1 that are symmetric around the z axis (i.e. $aO = Ob$). The recorded times on both a and b are equal because they lie on the same isochrones. This observation implies that the travel time response on the recording surface is symmetric. In Figure 3-2, the old aO and Ob are transformed to $a'O'$ and $O'b'$ respectively. The triangles $a'O'a$ and $b'O'b$ (the shaded areas) are isosceles because the points a and b on the recording surface are selected such that $aO' = a'O'$ and $O'b = O'b'$. From the geometrical analysis of the isosceles triangle the added time (Δt) along the recording surface (x) is approximated as

$$\Delta t = \frac{2\sin\left(\frac{\beta}{2}\right)}{v_{ave}(x,t)} x, \tag{3.1}$$

with $v_{ave}(x,t)$ being the average velocity and β being the geological dip. Assuming small variations in v_{ave}, equation (3.1) shows that the gradient of Δt is proportional to x. Hence, the travel time response can be approximated by adding a linear time shift to the normal hyperbola. In other words, since the recording surface records the asymmetric wavefront with respect to z' axis, the recorded travel time is an asymmetric and tilted hyperbola.

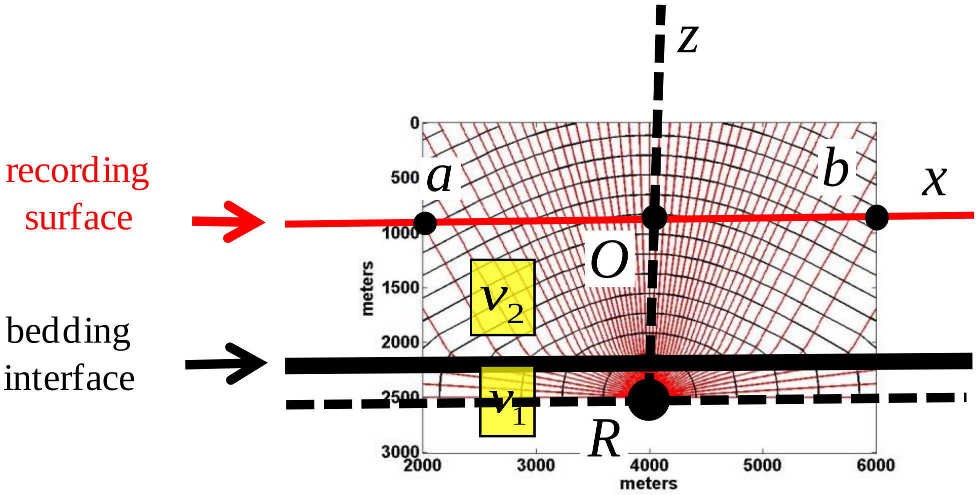

Figure 3-1: Scatter point response below a horizontal interface

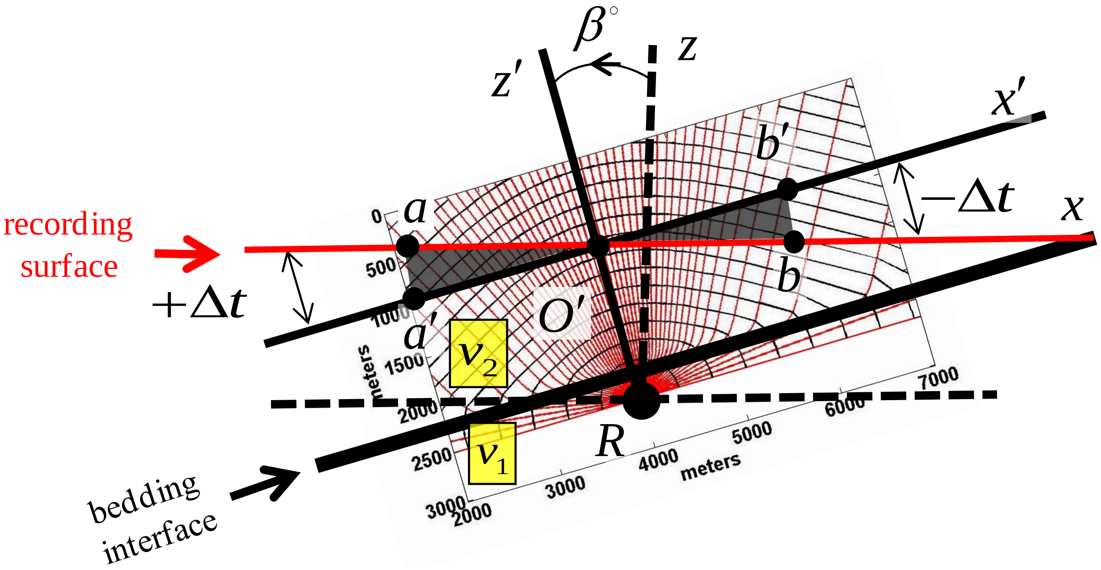

Figure 3-2: Scatter point response below a dipping interface

3.2.2 Tilt in CSP data

Figure 3-3 displays a dipping reflector velocity model. A scatterpoint wavefront is simulated using ray tracing approach. Inspired from the effects of equation (3.1) on CSP data, the CSP response of the numerical model is simulated. In Figure 3-3b, the recorded traveltime response from the scatter point (blue dotted curve) and the corresponding normal symmetric hyperbola (red curve) are compared. Figure 3-3c shows the difference between two curves. The difference curve indicates an approximate linear time shift at small equivalent offsets as

$$t_{tilted} \approx t_{normal} + \alpha h_e \ , \qquad (3.2)$$

where, t_{normal} is the traveltime of a normal hyperbola corresponding to the diffraction rays passing through a horizontal interface (as shown in Figure 3-3a), and t_{tilted} is the real travel time in the form of the tilted hyperbola. The parameter α (s/m) is the tilt coefficient that needs to be estimated using the slope of time difference curve (i.e., slope of curve in Figure 3-3c).

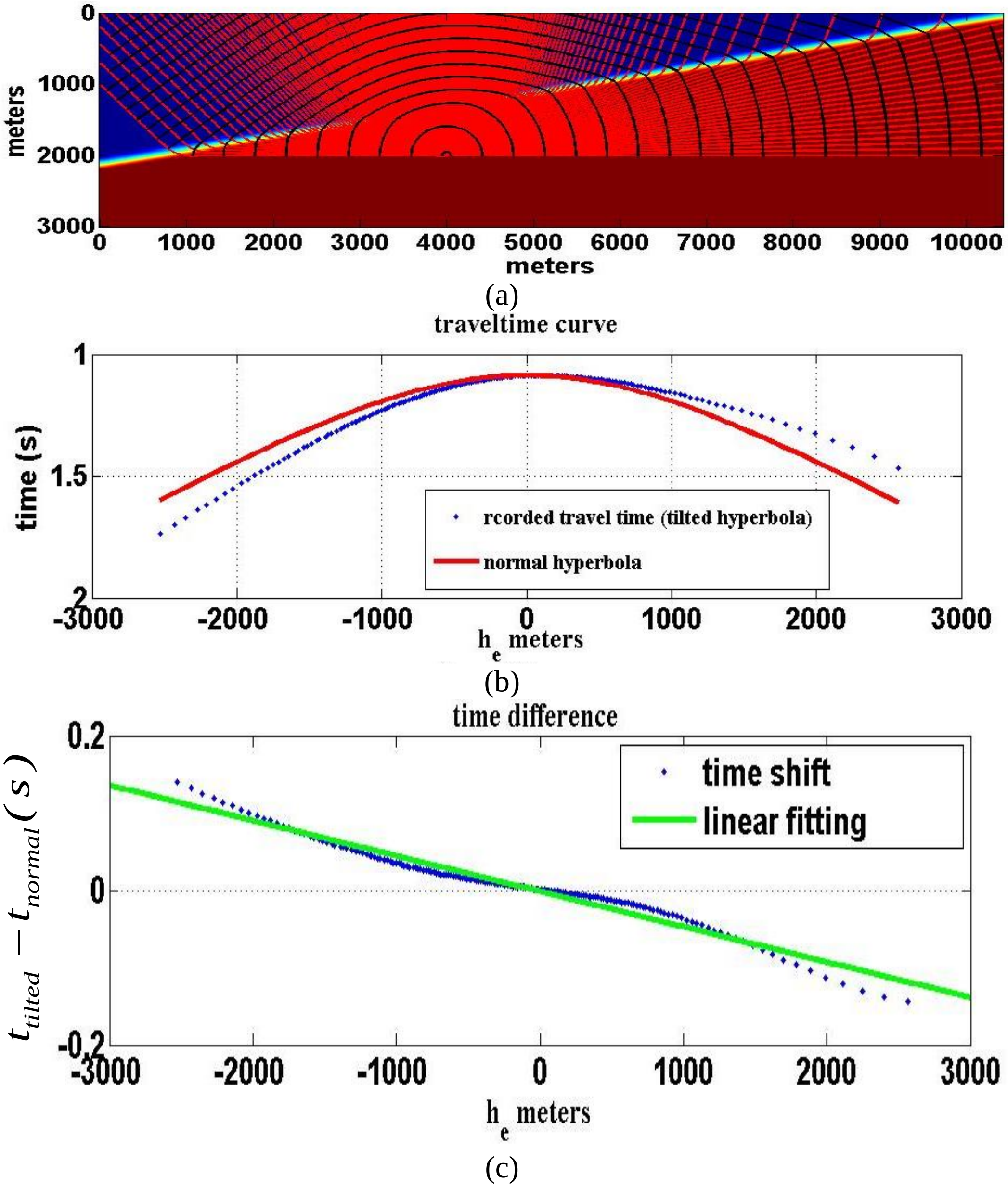

(a)

(b)

(c)

Figure 3-3: Travel time simulation (a) rays and wave front construction of a diffraction of a scatter point under a simple dipping interface (b) recorded travel time in equivalent offset domain (blue) with normal hyperbola (red) (c) the time shifts.

3.2.3 Marmousi data set example

The Marmousi complex model contains dipping interfaces with lateral velocity variations. The Marmousi data set consists of 240 shots spaced at 25 m. The spread has 96 receivers separated by 25 m at an offset of 200 m from the shot (Versteeg, 1994). A scatterpoint at the $x = 3200m$ coordinate of the model is selected for analysis. In Figure 3-4 the rays and wave front behavior from scatter points **A** and **B** at the depths of 1500 m and 2400 m are simulated. The ray-tracing travel times are converted to the equivalent offset domain using equations (2.13) and (2.14). As shown in Figure 3-5, the modeled CSP gather of $x = 3200$ m shows a reasonable fit with the real CSP gather obtained from synthetic data.

The effect of tilt on the resolution of the semblance plot is a function of the separation of the energy on the left side of the CSP data (i.e., $h_e < 0$) and the right side of the CSP gather (i.e., $h_e > 0$). Figure 3-6 compares the semblance plot of the left-sided with the right-sided gather. For scatter points **A** and **B**, the velocity contrast is around 200 m/s. We used two methodologies to resolve this problem.

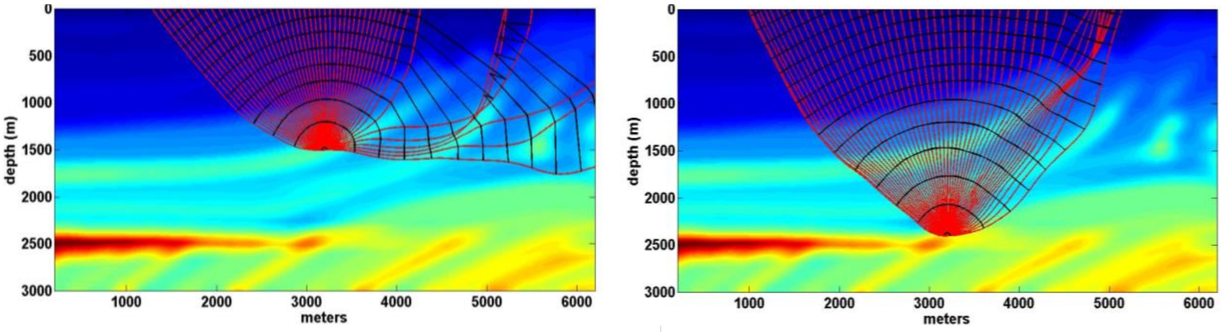

(a) (b)

Figure 3-4: Two scatter point responses and their wave front construction at the 3200 m lateral coordinate of the Marmousi model at depths of (a) 1500 m and (b) 2400 m .

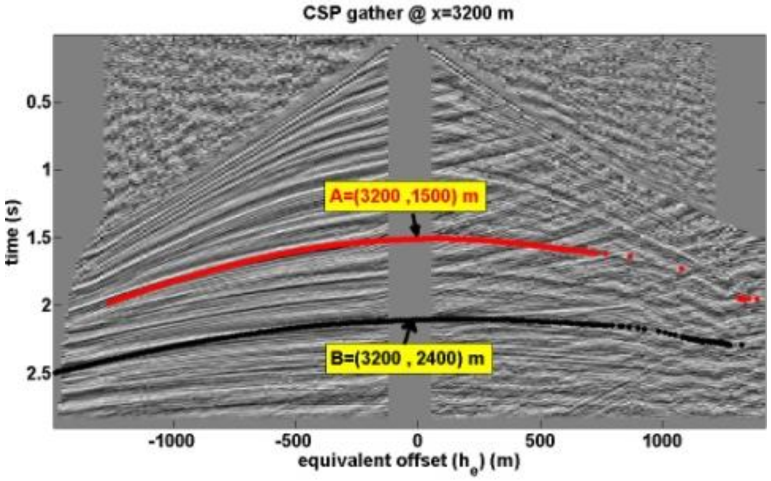

Figure 3-5: Comparison of modeled scatter point responses from Figure 3-4 in the equivalent offset domain and in the CSP gather.

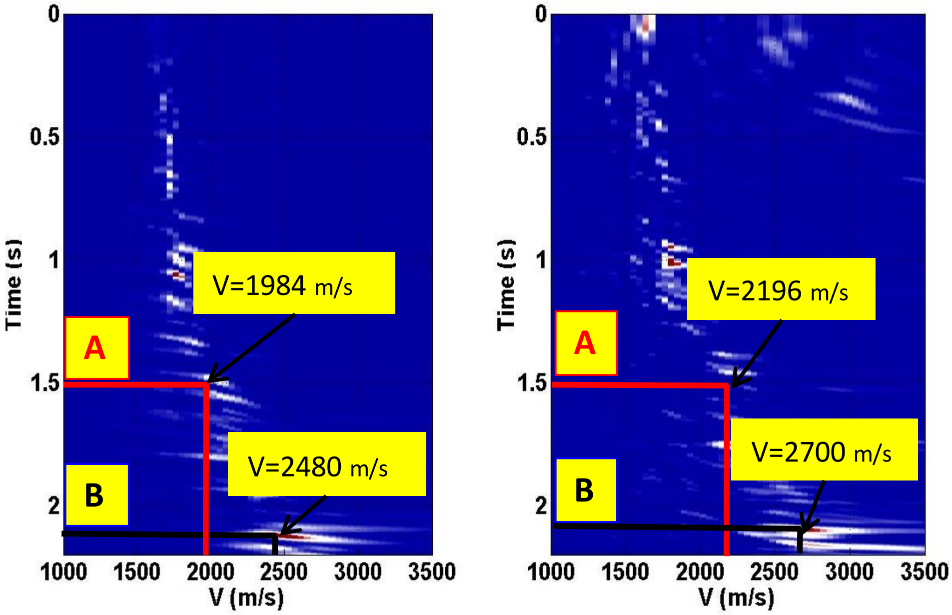

(a) (b)

Figure 3-6: Semblance plot for (a) the left-sided and (b) the right-sided CSP gather

3.2.4 Method (I): Application of Hyperbolic Least Square Fitting

Given *n* points of the CSP events, i.e., (h_e, t), the equation of the hyperbola. The purpose of least squares fitting is to determine the values of the coefficients, i.e., the coefficient vector, which minimizes the sum of the squares of the errors. In this study, the method proposed by Leary (Leary, 2004) is used which finds the equation of non-symmetric hyperbolae by a least squares fitting using a generalized eigenvectors approach.

If the parameters of the hyperbolic equation of the CSP data are determined, then it is possible to find its other properties, such as the tilt and the principle axis. Then we are able to rotate its principle axis to the vertical and to determine its velocity. In Figure 3-7, the modeled travel time of two events **A** and **B** at zero offset times of $\tau = 1.5$ s and $\tau = 2.1$ s are analyzed. The blue curves show the original time in the equivalent offset domain. The normal hyperbola after removing the tilt from blue curve by least squares is shown by red curve. Comparing original times with the normal hyperbola, the tilt coefficients for scatter points **A** and **B** are determined to be $\alpha = -2.23 \times 10^{-5}$ (s/m) and $\alpha = -2.3 \times 10^{-5}$ (s/m) respectively. This is an accurate approach, and its efficiency requires picking scattered events appropriately.

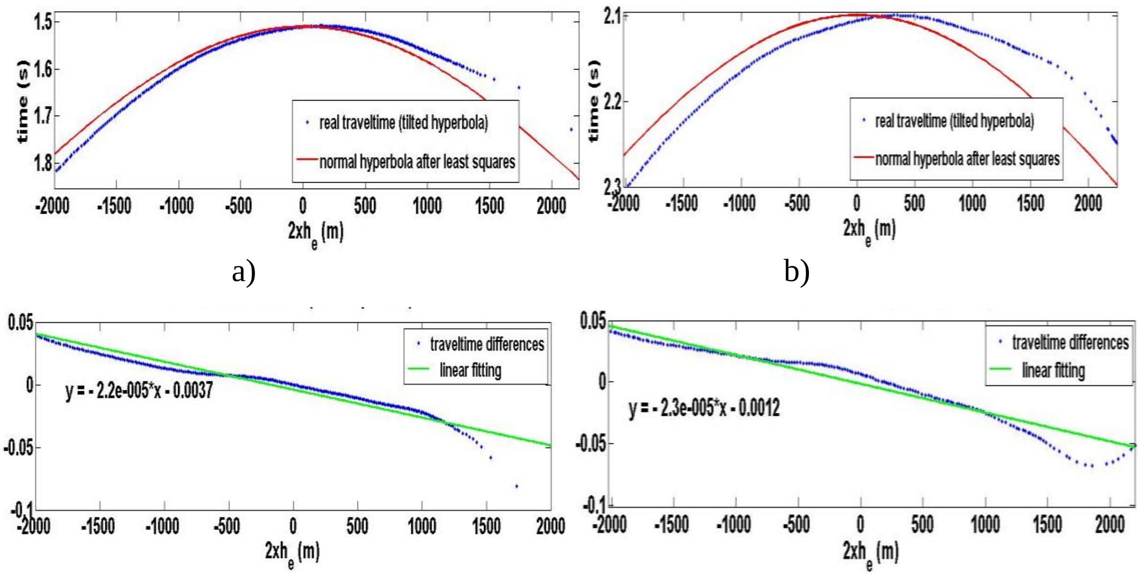

a) b)

c) d)

Figure 3-7: Modeled travel time analysis of CSP gather (a & b) comparisons of travel times of scatter points **A** and **B** with its normal hyperbola (c & d) the linear time shifts. The vertical axis of (c & d) represents traveltime hift.

3.2.5 Method (II): Linear Time-Shifted Hyperbolic Radon Transform

In order to map the hyperbolic event to a focused point in the hyperbolic Radon domain, we use a Linear Time-Shifted Hyperbolic Radon Transform (LTSHR) transform that operates on the travel time path defined by equation (3.2). Let d represent a seismic signal in a CSP gather. The stacking path in the Radon formula is defined as:

$$d\left(\tau, v_m, \alpha\right) = \int_{\alpha}\int_{h_e} d\left(t = \left[\tau^2 + \left(\frac{2h_e}{v_m} \right)^2 \right]^{1/2} + \alpha h_e, h_e \right) dh_e \, d\alpha \quad , \tag{3.3}$$

with *t* being the two-way travel time and v_m the migration velocity. The algorithm for creation of the LTSHR domain is similar to the hyperbolic Radon transform, with an additional loop introduced for different tilt coefficients α. This forms a 3D semblance cube of CSP gather with dimension $\left(\tau, v_m, \alpha\right)$ as shown in Figure 3-8. The left face of the cube represents the regular semblance plot. From the left face to the right, semblance plots correspond to increased values of the tilt coefficient, α. As seen inside the cube, the defocusing of energy due to tilt in the hyperbola is corrected if compared with $\alpha = 0$. This can be seen in two semblance time slices for scatter point **A** and **B** in Figure 3-8b and Figure 3-8c as the base of the slice represents the regular semblance plot. The black curve in the semblance cube indicates the picked optimum values of α at every interval. Finally, for migration velocity, semblance values of optimum α were picked as shown by the red curve of Figure 3-8a.

Figure 3-9 compares the regular semblance plot with the modified semblance plot obtained with the optimum α and t_{tilted} corrections of equation (3.2). As highlighted with circles, comparing the focusing of semblance values shows that the accuracy of velocity picking has increased in this model due to focusing of energy of scatterpoint. Although ray tracing can estimate more accurate traveltime of the scatterpoint using ray tracing, however, tilt approximation of dipping layers models is useful when the ray tracing is not available. The appropriate NMO on the CSP gather enhanced the output image of the EOM process. As shown in Figure 3-10, it increases the image quality by focusing the scattered energies and reducing the mispositioning errors due to the tilt effect.

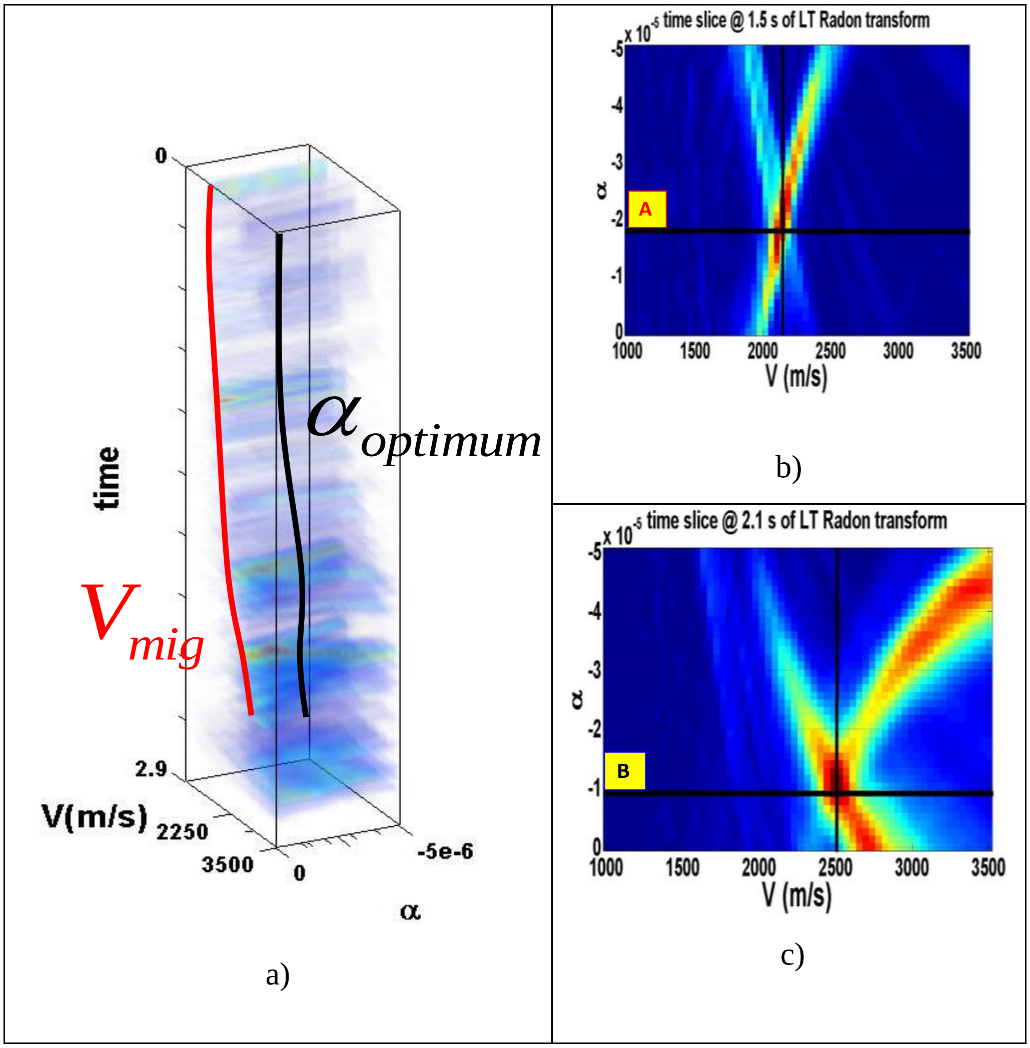

a)

b)

c)

Figure 3-8: LTSHR transform of CSP gather. a) The semblance cube computed based on (b) The time slice for scatter point **A**, with optimum $\alpha = -2.1 \times 10^{-5}$ (s/m), (c) the time slice for scatter point **B**, with optimum $\alpha = -1.3 \times 10^{-5}$ (s/m).

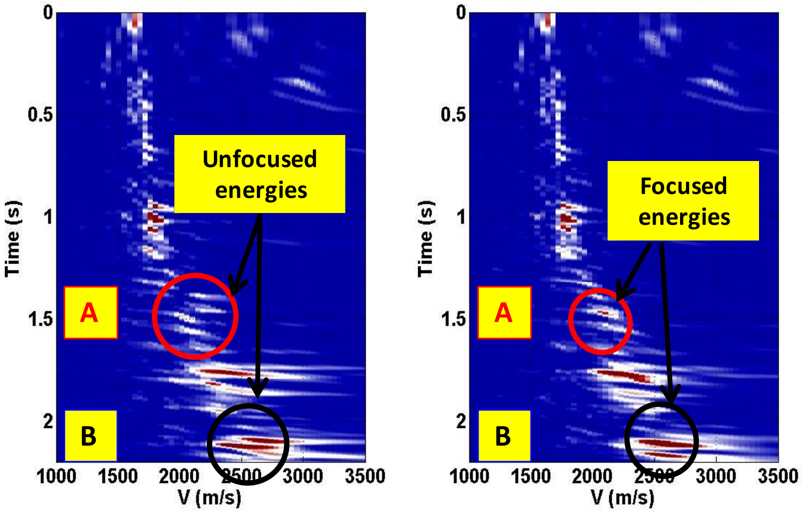

a) b)

Figure 3-9: Comparison of (a) regular semblance plot with (b) semblance according to linear time shift hyperbolic Radon transform with optimum α .

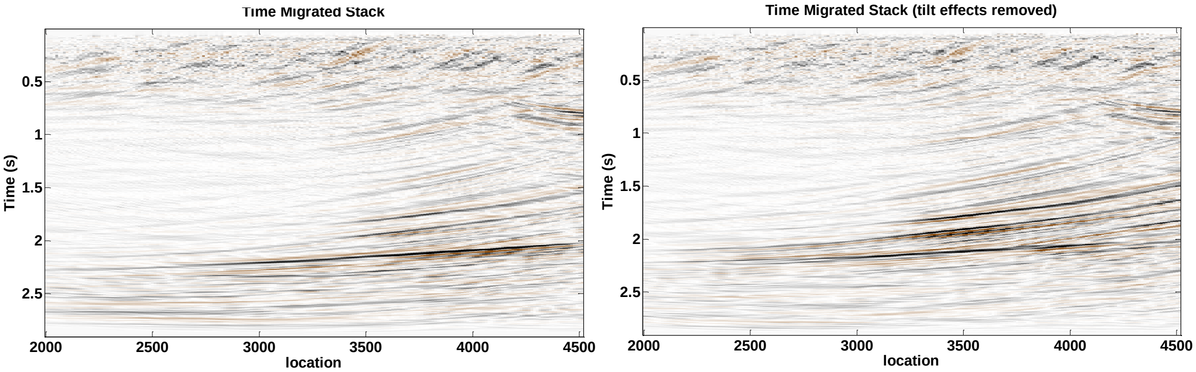

a) b)

Figure 3-10: Image construction using: a) regular PSTM and b) Removed tilt PSTM.

3.3 Acoustic FWI method for P-to-P velocity inversion using time imaging

In this section, the implementation of the FWI algorithms for velocity inversion using PSTM methods is discussed. A forward Kirchhoff operator for the prediction of shot records from the reflectivity function is used. The relationship between the perturbed shots and the velocity model is used to facilitate the estimation of the gradient function using Prestack Kirchhoff Time Migration (PSTM) and its associated forward operator for the updating process. The data is obtained using forward Kirchhoff operator from the acoustic synthetic model on the left side of Marmousi where the lateral variation in velocity is small.

3.3.1 Theory

Acoustic Born integral solution to the wave equation formula can be written in the form of (Beylkin and Burridge, 1990 and Kroode, 2012)

$$\delta d(\boldsymbol{x}_r,\boldsymbol{x}_s,t)=\frac{\partial^2}{\partial t^2}\int dx^3 G_0(\boldsymbol{x}_r,\boldsymbol{x},t)S(\boldsymbol{x},\theta)G_0(\boldsymbol{x},\boldsymbol{x}_s,t), \tag{3.4}$$

where, $S(\boldsymbol{x},\theta)$ is angle dependent scattering potential function defined by

$$S(\boldsymbol{x},\theta)=\frac{2}{\rho_0 v_0^2}\left(\frac{\Delta v(\boldsymbol{x})}{v_0(\boldsymbol{x})}+\frac{\Delta\rho(\boldsymbol{x})}{\rho_0(\boldsymbol{x})}cos^2\theta\right), \tag{3.5}$$

and θ is the angle between incident and reflected waves, G_0 is the Greens function satisfying acoustic wave equation. In this chapter, the density variation is assumed to be constant, and the density term in equation (3.5) is ignored.

The velocity perturbation $\delta v(\boldsymbol{x})$ is given by (Tarantola, 1984)

$$\delta v(x)=\int_{x_s}\int_{x_r} d\boldsymbol{x}_r d\boldsymbol{x}_s \tilde{A}^*(\boldsymbol{x}_s,\boldsymbol{x})\widehat{A}^*(\boldsymbol{x},\boldsymbol{x}_r)\left(\delta d(\boldsymbol{x}_r,\boldsymbol{x}_s,t-\tilde{\phi}^P-\widehat{\phi}^P)*\ddot{s}(-t)\right), \tag{3.6}$$

where, $\tilde{A}(\boldsymbol{x}_s,\boldsymbol{x})$ and $\widehat{A}(\boldsymbol{x},\boldsymbol{x}_r)$ are the true amplitude term of downgoing and upgoing wave respectively, the superscripts $*$ are corresponding adjoint amplitude operators. s is the source signature. Equation (3.4) serves as a forward operator that distributes the energy of the scatter point to model the shot records. The migration operator is the diffraction stack integral in equation (3.6) that sums the distributed energy and locates it on the subsurface coordinate. Equation (3.6) indicates that velocity perturbation is obtained by migration and deconvolution with the source function.

The Computational burden is a problem for implementation because equations (3.4) and (3.6) require ray tracing as the subsurface coordinate is defined in depth. To have cheaper computational time, PSTM and corresponding forward modeling is used. This states that without the loss of generality, depth domain z of the model parameters are transformed to τ domain. So, if the structure of $\delta v(x,z)$ and the formulation of forward modeling and migration can be adjusted to a time imaging approach, then we can estimate $\delta v(x,\tau)$ using the framework of FWI algorithms that are commonly used for inversion. For forward modeling of equation (3.4), the Kirchhoff operator is used, and for inversion of equation (3.6), the EOM approach of Bancroft et. al., (1998) is used. All operators and velocity models are updated during the iteration procedure.

Figure 3-11and Figure 3-12 show a two-layer medium containing velocities v_1 and v_2 and illustrate the kinematical difference of the algorithms in depth (z) and time (τ) Figure 3-11a shows a simple velocity model where the velocity changes from v_1 to v_2 at z_1. The initial velocity model, Figure 3-11b, is assumed to change from v_1 to v_2 at z_2. For simplicity, assuming true amplitude and multiple-free data the analytical estimated gradient $\gamma(z)$ is a boxcar function given by (Innanen and Margrave, 2011)

$$\gamma(z) = K\left(H(z-z_1) - H(z-z_2)\right), \tag{3.7}$$

where H is the step function and K contains true amplitude and velocity and density of background model. This is also shown in Figure 3-11c. By combining the initial model and gradient function, after the first iteration, the inversion for the true velocity model is complete. Given equations (3.4) and (3.6), without the loss of generality, the time domain gradient $\gamma(\tau)$ in Figure 3-12c will be scaled (and integrated in time) and have a similar shape to equation (3.7) as denoted by

$$\gamma(\tau) \propto K\left(H(t-\tau_1) - H(t-\tau_2)\right). \tag{3.8}$$

The shape of velocities is the same in time as in depth, however the main difference between equation (3.7) and (3.8)is that in time, stretching effects occur as a result of depth-to-time conversion.

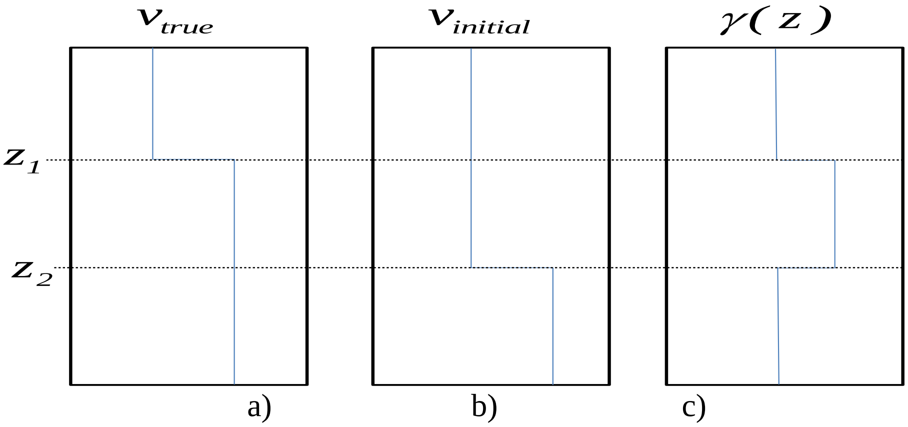

Figure 3-11: Kinematics of FWI using depth migration. a) Plot of a velocity model $v(z)$ versus depth z, b) starting velocity model and c) the gradient of the misfit function $\gamma(z)$ in the first iteration.

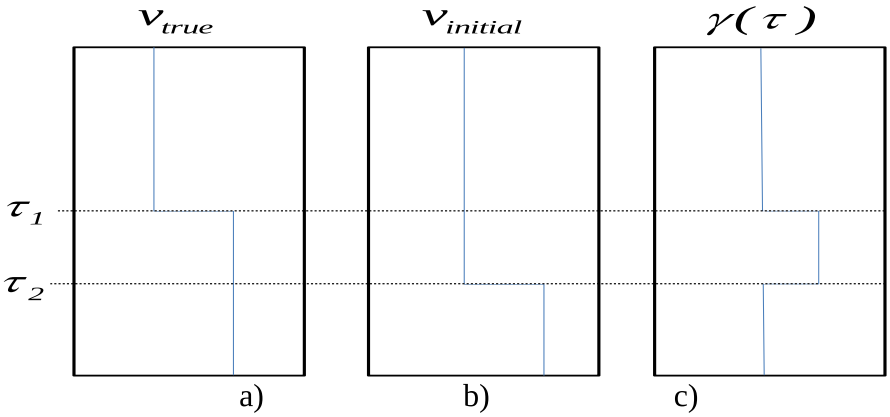

Figure 3-12: Kinematics of FWI using time migration. a) Plot of the velocity model in Figure 3-11 versus time τ, b) starting velocity in time and c) the gradient of misfit function $\gamma(\tau)$ in the first iteration.

The starting velocity model can be obtained from smoothed true velocity and is used to initiate the FWI process. The workflow for the FWI algorithm using PSTM is summarized in Figure 3-13 as follows:

1. Establish the starting velocity model.
2. Run the forward model of the shot records using equation (3.4).
3. Compute the gradient of the misfit function with $\gamma(x,\tau)$ using equation (3.6).
4. Search for the optimum step length α in the steepest descent method.
5. Updated the model $v(x,\tau)$.

6. Convert $v(x,\tau)$ to $v_{rms}(x,\tau)$ in preparation for the next iteration migration and forward modeling.

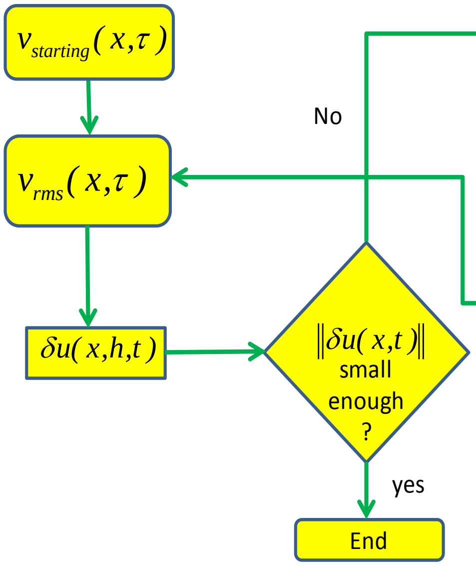

Figure 3-13: Simplified workflow for updating the velocity model using the time migration FWI algorithm.

3.3.2 Numerical example:

As shown in Figure 3-14a, a synthetic numerical model from Marmousi's left side model (with small lateral variations in the velocity) was selected. The density is assigned to be constant. The starting model was defined by applying a 2D Gaussian smoother of 700m length to the true model (i.e., Figure 3-14c). The Kirchhoff operators for the forward modeling produced 21 shots records, each with 201 receivers in split spread configuration with receiver spacing of 12.5m. The inversion implemented to a range 5-12 Hz frequencies. A number of wavelets were employed, with minimum phase and a range of dominant frequencies that was arbitrarily chosen to vary from 5 to 12 Hz. To match the frequency range of the "true" data to the modeled data, same bandpass filters were applied to model data. For convergence criterion, the iteration began with a 5Hz wavelet in the modeled shot records and allowed its frequency to increase to a maximum of 12 Hz, with increments of 0.5 Hz. The iterations performed on the starting velocity model ultimately gave an approximation of the true model. Figure 3-14d compares the true model with the inverted model after 45 iterations. Figure 3-14a is the velocity in depth domain that transformed to P-to-P time in Figure 3-14b. All iterations update the velocity to P-to-P time giving consistent inversion output with the true model. For comparison, Figure 3-15 shows the vertical profile of an updated velocity at the 1800m lateral position (black line) within the model and gives the overall reconstruction of the true model. Figure 3-16 shows the trend of the updating process versus iteration numbers. The first iteration number corresponds to initial model and the last one is the output of the algorithm. The trend shows that after 20 iterations the model construction accelerates because of the least square fitting associated with the event at $\tau = 1.75s$.

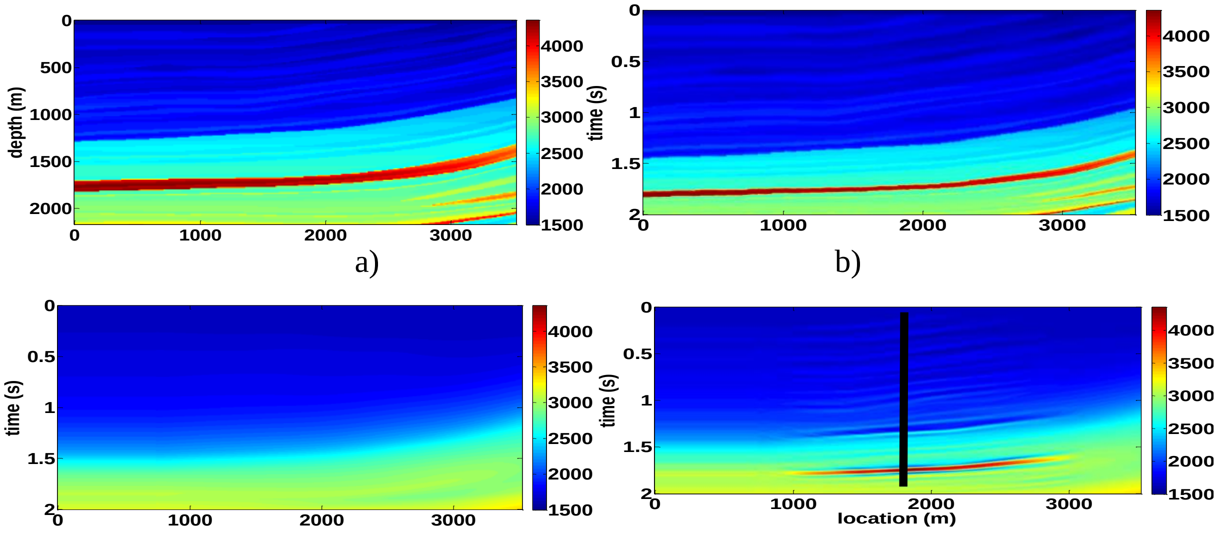

a)

b)

c)

d)

Figure 3-14: Numerical example of FWI using PSTM a) True velocity vs depth b) True velocity vs time c) starting velocity obtained by a 700m Gaussian smoothing operator d) The inverted velocity after 45 iterations. Color scale is the velocity and the vertical line in (c) indicates the well location at 1800m.

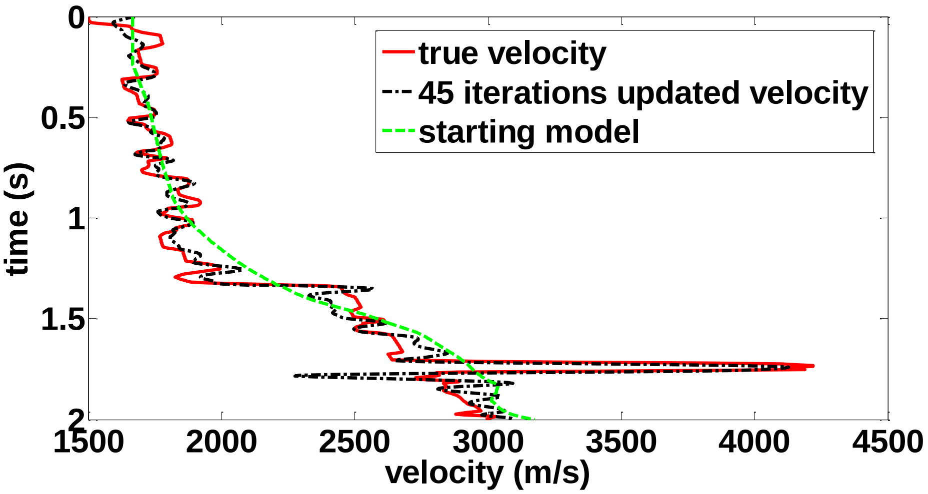

Figure 3-15: Comparison between the true velocity model (solid red) the starting model (green dashed) and the FWI model (dashed dot black) at 1800m lateral position.

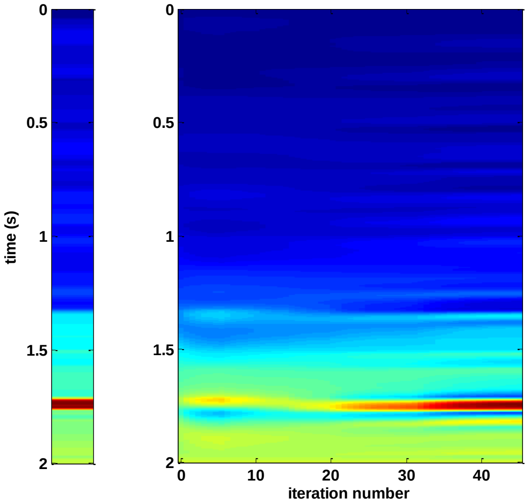

a) b)

Figure 3-16: FWI inversion updating trend of vertical profile at 1800m lateral position. a) The true velocity of a well profile. b) Velocity updates vs. iteration number of this well profile.

3.4 Conclusions

By wavefront numerical analysis, a relationship is established between the tilted 2-D hyperbolic travel time responses of scatter points below dipping interface with that from a constant lateral gradient model. It is shown that a similar tilt effect exists on the CSP data. This causes a lack of clarity and accuracy in velocity picking using the semblance plots. We proposed two remedial approaches to determine the optimum tilt coefficient. Removing of the tilt leads to focusing of energies in CSP data and to increasing the resolution of semblance plots. We showed that removing of tilt can enhance the imaging output by focusing the energy.

In case of geological structure with small lateral velocity variation, the linearized solution of the seismic reflection inverse problem can be obtained using the Prestack Kirchhoff Time Migration (PSTM) and corresponding forward modeling. It requires updating the velocity in time and it incorporates accurate diffraction stack weighting of the PSTM data.

The implementation of PSTM and corresponding forward modeling in the FWI algorithm for velocity inversion of isotropic and acoustic medium is demonstrated. The advantage of the method is its low computational cost compared to corresponding PSDM techniques. In PSTM approach, the traveltime is approximated from the Double Square Root (DSR) equation. For geologically complex structures, due to the limitations of forward modeling and its migration operator, the inversion procedure is not accurate compared to the use of depth migration that requires ray tracing algorithms.

Chapter 4: Iterative multiparameter elastic waveform inversion using Kirchhoff approximation

4.1 Introduction

Chapter 2 explains the procedure of FWI and the concept of scattering waves based on the Born approximation solution of the wave equation. Chapter 3 gives numerical insight into the solution of the inverse problem where the time imaging method. The method presented in Chapter 3 is applicable for all types of Kirchhoff based time migrations. In this chapter, communication between the Born and Kirchhoff approximation is used. Forward modeling and migration/inversion is applied to the elastic FWI method according to surface integral Kirchhoff approximation (Figure 4-1). Here, Kirchhoff migration combined with the approximation of the DSR equation is used for migration/inversion. The inversion of elastic properties from P-to-P and P-to-S waves using DSR migration is illustrated numerically. The advantage of Kirchhoff approximation over Born approximation are illustrated using associated boundary conditions and numerical examples.

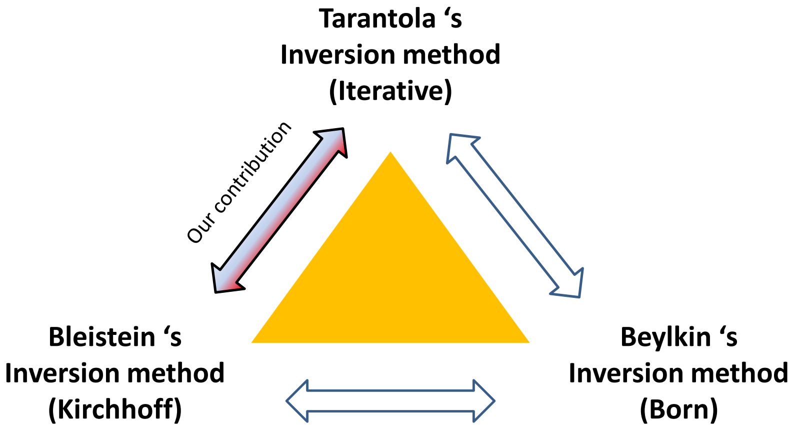

Figure 4-1: Relationship between the Kirchhoff migration/inversion and FWI method

4.2 Relationship between the Born and Kirchhoff approximation

Formulation of Born and Kirchhoff approximation are asymptotically similar given a smooth error (Beylkin and Burridge, 1990, Jaramillo and Bleistein, 1999, Shaw and Sen, 2004 and Kroode, 2012). Their difference comes from their model perturbation shapes and associated boundary condition. In contrast with Born approximation, where $\delta\boldsymbol{m}$ has Heaviside-type singularity, in Kirchhoff approximation, the singularity of $\delta\boldsymbol{m}$ is defined by a delta function in a coordinate orthogonal to the reflector, $\chi_{\mathrm{R}}(x)$, and the boundary condition given by

$$\frac{\partial}{\partial n}\delta\boldsymbol{m}(\boldsymbol{x}) = \Delta\boldsymbol{m}(x)\chi_{\mathrm{R}}(\boldsymbol{x}), \tag{4.1}$$

which after substituting into equation (2.21) transforms the volume integral to the surface integral (see e.g. Kroode, 2012). Ursin and Tygel (1997) interpret the Kirchhoff surface scattering integral by applying the divergence theorem to the Born scattering volume integral. Figure 4-2 defines a surface, $\sum$, along which the medium, m, varies steeply, e.g. equation (4.1). The gradient of surface, $\sum$, is parallel to the gradient direction of m. Now, we have

$$\boldsymbol{m}_{\text{true}} = \begin{cases} \boldsymbol{m}_0 + \Delta\boldsymbol{m}^{+}, & \text{above } \Sigma \\ \boldsymbol{m}_0 + \Delta\boldsymbol{m}^{-}, & \text{below } \Sigma \end{cases}, \tag{4.2}$$

where m_0 is a function in D and $\Delta\boldsymbol{m}^{\pm}$ are smooth functions (i.e. perturbations) above and below, $\sum$, respectively. As shown in Figure 4-2b, if the integration domain is divided into the upper and lower hemispherical volumes D^{+} and D^{-} respectively, then we can decompose the total volume integrals of equations (2.21) over D into two volume integrals over D^{-} and D^{+}

$$\delta d = \int_{D} S(\boldsymbol{x})e^{i\omega\phi}d\boldsymbol{x} = \int_{D^{-}} S(\boldsymbol{x})e^{i\omega\phi}d\boldsymbol{x} + \int_{D^{+}} S(\boldsymbol{x})e^{i\omega\phi}d\boldsymbol{x}. \tag{4.3}$$

The $S(x)$ and ϕ can be scatter potential and traveltime respectively. The asymptotic approximation of the Fourier integral shows how to decompose a volume integral into a surface over ∂D (with a normal vector $\vec{n}$ as seen in Figure 4-2a) and a volume integral over D is as follows (Bleistein, 1984)

$$\delta d = \int_D S(\boldsymbol{x}) e^{i\omega\phi} d\boldsymbol{x} = \frac{1}{i\omega}\left\{ \int_{\partial D} S(x) \frac{\vec{n}.\vec{\nabla}\phi(\boldsymbol{x})}{\left|\vec{\nabla}\phi(\boldsymbol{x})\right|^2} e^{i\omega\phi} d\sigma - \int_D \nabla . \left[\frac{S(\boldsymbol{x})\vec{\nabla}\phi(x)}{\left|\vec{\nabla}\phi(\boldsymbol{x})\right|^2} \right] e^{i\omega\phi} d\boldsymbol{x} \right\}. \tag{4.4}$$

For the case of volume integral in Figure 4-2a, the supporting scattering is inside the volume, D, and because of the Sommerfield radiation conditions, the contribution of the integration over the surface, ∂D is small compared to the total volume D. For the case of surface integral in Figure 4-2b, the surface integrals are the dominant contributors. This is because the ∂D surface $\sum$, which is the main contributor to both region integrals, belongs to the surface ∂D^-. The Sommerfield radiation condition applies to boundaries and total integral contributions are

$$I^- = -i\omega \int_\Sigma S^-(\boldsymbol{x}) \frac{\vec{n}.\vec{\nabla}\phi(x)}{\left|\vec{\nabla}\phi(x)\right|^2} e^{i\omega\phi} d\sigma, \tag{4.5}$$

and

$$I^+ = i\omega \int_\Sigma S^+(\boldsymbol{x}) \frac{\vec{n}.\vec{\nabla}\phi(\boldsymbol{x})}{\left|\vec{\nabla}\phi(\boldsymbol{x})\right|^2} e^{i\omega\phi} d\sigma. \tag{4.6}$$

Using (2.29) , (2.30), (4.5) and (4.6) we have scattering operator as

$$S(\boldsymbol{x}) = [\frac{\Delta\rho^+(\boldsymbol{x}) - \Delta\rho^-(\boldsymbol{x})}{\rho_0(\boldsymbol{x})}\delta_{ik} + \frac{\Delta c^+_{ijkl}(\boldsymbol{x}) - \Delta c^-_{ijkl}(\boldsymbol{x})}{\rho_0(\boldsymbol{x})} p^R_j p^I_l] h^I_k h^R_i, \tag{4.7}$$

Equation (2.25) expresses the radiation pattern of the scattering potential of the Born approximation as step-like, whereas equation (4.7) displays that of the Kirchhoff approximation as spike-like, which is a result of singularities over the surface $\sum$ (i.e. steep gradient of elastic properties). A continuum elastic model is displayed in Figure 4-3. A typical perturbation $\delta\boldsymbol{m}$ is considered. Note that here, $\delta\boldsymbol{m} = \boldsymbol{m}_{true} - \boldsymbol{m}_{background}$ where, $\boldsymbol{m}_{background}$ is a background model. As seen in Figure 4-3a, the first order Born approximation consider the perturbation independently from its surroundings which infers that although the background model of Born approximation is continuous, however, the continuity of the perturbed model with its surrounding is neglected at bedding interfaces. Continuity of perturbation across the bedding interface is considered in the Kirchhoff approximation as illustrated in Figure 4-3b, where the differential of both particles δm^+

and $\delta \boldsymbol{m}^{-}$ with respect to layer boundary, i.e., $\delta \boldsymbol{m}^{+} - \delta \boldsymbol{m}^{-}$, is considered. Hence, for this perturbation the surface integral Kirchhoff approximation considers the bedding interfaces within the perturbed model. In iterative inversion algorithm, after the first iteration, the background model parameters are updated which produce the reflection boundaries. In this situation, Kirchhoff approximation is more useful for forward modeling. Consistent with forward modeling, the inversion is based on reflectivity function of Zoeppritz equations (Aki and Richards, 1980). Therefore, the boundaries of updated model produces reflection to be used in estimation of gradient function. In the next section, the linearized reflectivity function of Zoeppritz equations is compared to scattering potential of Born approximations, then the algorithm used for iterative inversion is illustrated using numerical examples.

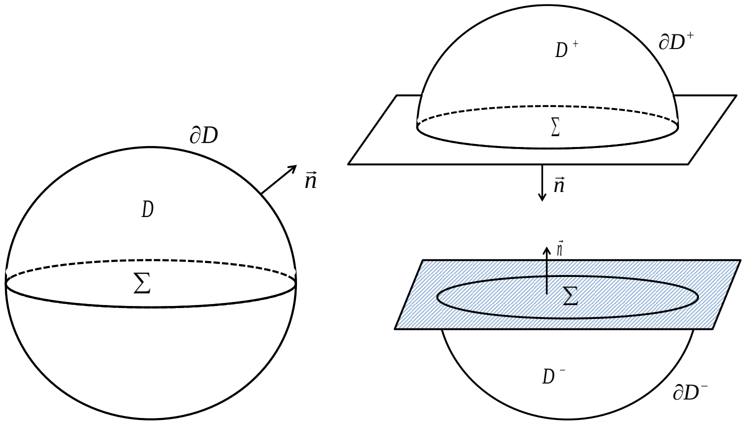

a) b)

Figure 4-2: The relationship between the Born approximation (volume integral) and the Kirchhoff approximation (surface integral). Adapted from Bleistein et al. (2001).

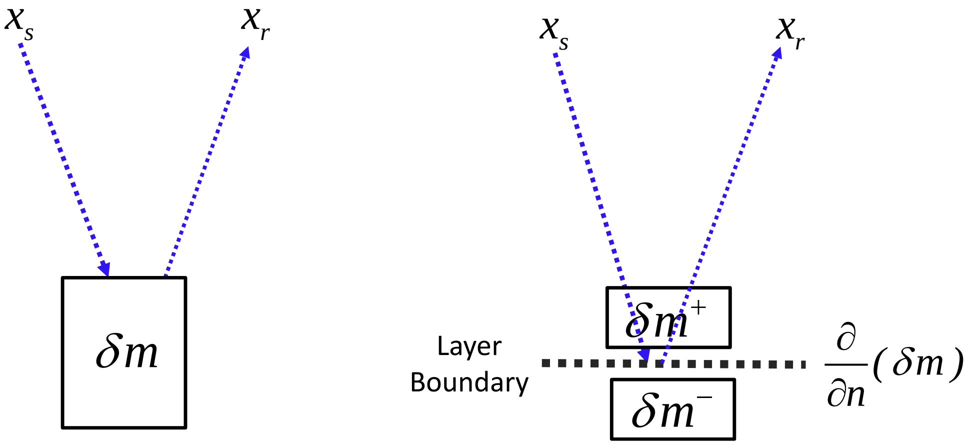

a) b)

Figure 4-3: The illustration of the perturbation of a continuous elastic model using: a) the Born approximation and b) the Kirchhoff approximation.

4.3 Scattering potential of Born approximation vs reflectivity function of Kirchhoff approximation

The Zoeppritz reflectivity functions of P-to-P, R^{PP} and P-to-S, R^{PS}, waves are related to equations (2.26) and (2.27) by (Shaw and Sen, 2004 and Ursin and Tygel , 1997)

$$R^{PP} = \frac{1}{4\rho_0 \cos^2 \theta^P} \frac{\partial}{\partial n} S^{PP}, \tag{4.8}$$

and

$$R^{PS} = \frac{\tan \theta^S}{2\rho_0 \sin(\theta^{PS})} \frac{\partial}{\partial n} S^{PS}. \tag{4.9}$$

Hence, instead of scattering potential of Born operators, the iterative scheme uses Kirchhoff operator with Zoeppritz reflectivity functions (Aki and Richards, 1980) for forward modeling and the migration operators. The simple example in Figure 4-3 illustrates that the derivative operator $\frac{\partial}{\partial n}$ changes the shape of a perturbed model. A well log data in Figure 4-3a is smoothed as an initial model. The difference of initial and true model is the perturbation to be found by inversion. The shape of perturbation is consistent with the Born inversion but the shape of the derivative of perturbation is consistent with Kirchhoff approximation. Both perturbation and its derivative are normalized and depicted in Figure 4-3b. In practice, when using Kirchhoff operators, the optimum weight function A can be assigned to account for several amplitude factors such as attenuation, reflection, transmission and geometrical spreading factor. In the next section, numerical examples will show the iterative inversion process and the DSR traveltime approximation techniques for models with smoothly varying elastic properties.

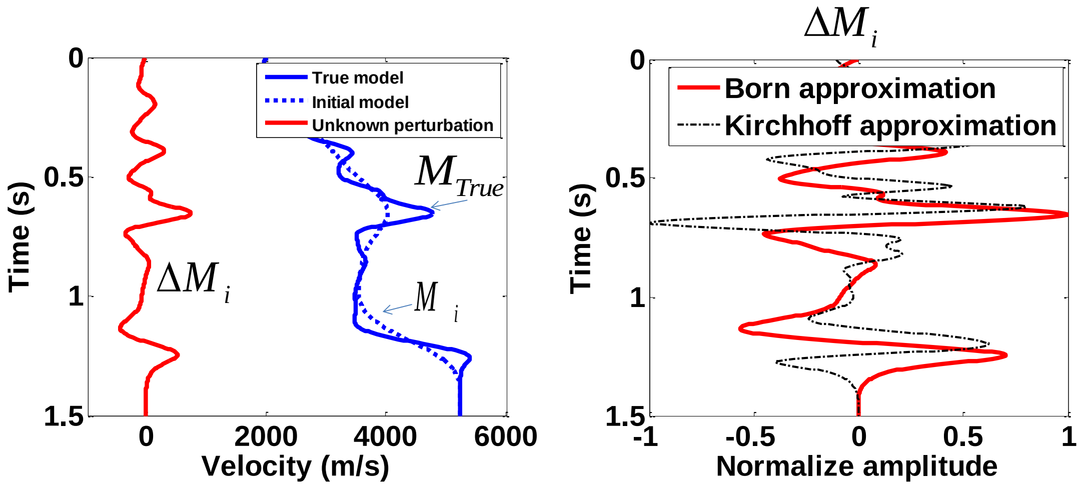

a) b)

Figure 4-4: a) An example of the shape of model perturbation from a true velocity. b) Comparison between the shape of normalized model perturbation in the normalized inversion using the Born and Kirchhoff approximations.

4.4 Travel time considerations for simultaneous inversion of P-to-P and P-to-S data

In PSTM approximation the associated travel times are calculated from the Root Mean Square (RMS) velocity of P-wave $v^P{}_{RMS}$ and S-wave $v^S{}_{RMS}$. The amplitude function is obtained using an estimation of the reflectivity function obtained from the Zoeppritz solvers (Aki and Richards, 1980). In the forward modeling, the travel time for P-P data is approximated by

$$t^{pp} \approx \phi^P(s,x)+\phi^P(x,r)=\frac{r(s,x)}{v^P{}_{RMS}}+\frac{r(x,r)}{v^P{}_{RMS}}, \tag{4.10}$$

and the travel time for the P-S data is obtained by

$$t^{ps} \approx \phi^P(s,x)+\phi^S(x,r)=\frac{r(s,x)}{v^P{}_{RMS}}+\frac{r(x,r)}{v^S{}_{RMS}}. \tag{4.11}$$

To study the different methodologies for converted wave data processing and migration, the reader is referred to Mi and Margrave (2001). A common approach for time migration of P-to-S data is to find the image based on Common Converted Point (CCP), which ultimately maps the energy on P-to-S time. This procedure is useful during imaging if the shear velocity of the subsurface is unknown. This is displayed graphically in Figure 4-5a using synthetic model where the v_P and v_S of the medium are plotted versus t^{PP} and t^{PS} respectively. Figure 4-5b shows the migrated section of the P-to-P and P-to-S data obtained from the model Figure 4-4a. This shows that the P-to-S data space is mapped to the model space in t^{PS} coordinate, inferring that after imaging both P-to-P and P-to-S waves, a P-to-P and P-to-S registration are required to identify the events for interpretation.

In this thesis, the associated travel times are approximated by Dix's equation(Dix, 1955). The term $\phi^{P}(s,x)$ is the common travel time for both P-to-P and P-to-S data, and is used to form prestack volumes of the input elastic properties. For migration of P-to-P and P-to-S data, the algorithm sums the hyperbola corresponding to t^{PP} and t^{PS}, respectively and maps the result to P-to-P zero offset time τ. For forward modeling of P-to-P and P-to-S data, the algorithm distributes the energy of model in P-to-P zero offset time τ to the path estimated by hyperbola corresponding to t^{PP} and t^{PS}. For inversion the image gathers are required to perform AVO inversion. Combination of both operation is called migration/inversion F^{*} as discussed in equation (2.8). For P-to-P data the weight function of Bleistein (2001) and for P-to-S data the derived weight function of Cary and Zhang (2011) is used.

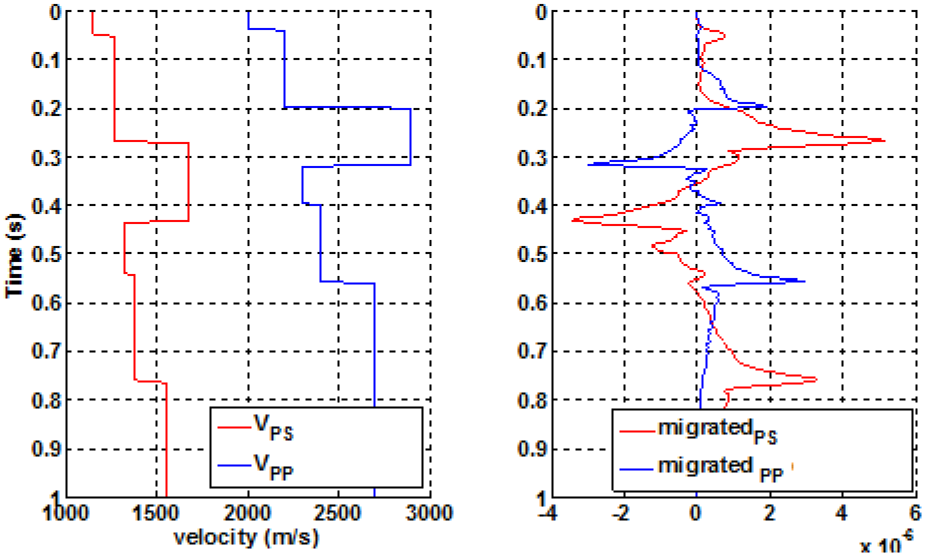

a) b)

Figure 4-5: Inconsistency between time of velocity model vs migrated CCP section. a) Velocity profile of P and S waves in P-P and P-S time respectively. b) Migration of P-to-P and P-to-S data in P-to-P and P-to-S time.

4.5 Description of workflow for iterative inversion

The workflow for inversion of elastic properties using the method of steepest descent is summarized in Figure 4-5. As in the inversion strategy proposed by Tarantola (1986), we can first invert for more contributing model parameters m such as Δv_p and Δv_s, then invert for $\Delta\rho$. The starting v_p and v_s can be obtained by conventional velocity analysis such as prestack migration gathers or available well log information. The updated model is used to update the forward modeling operator f and F^* to improve the travel time in each step. This is done using the relationship between the updated interval velocity to RMS velocity (Dix, 1955).

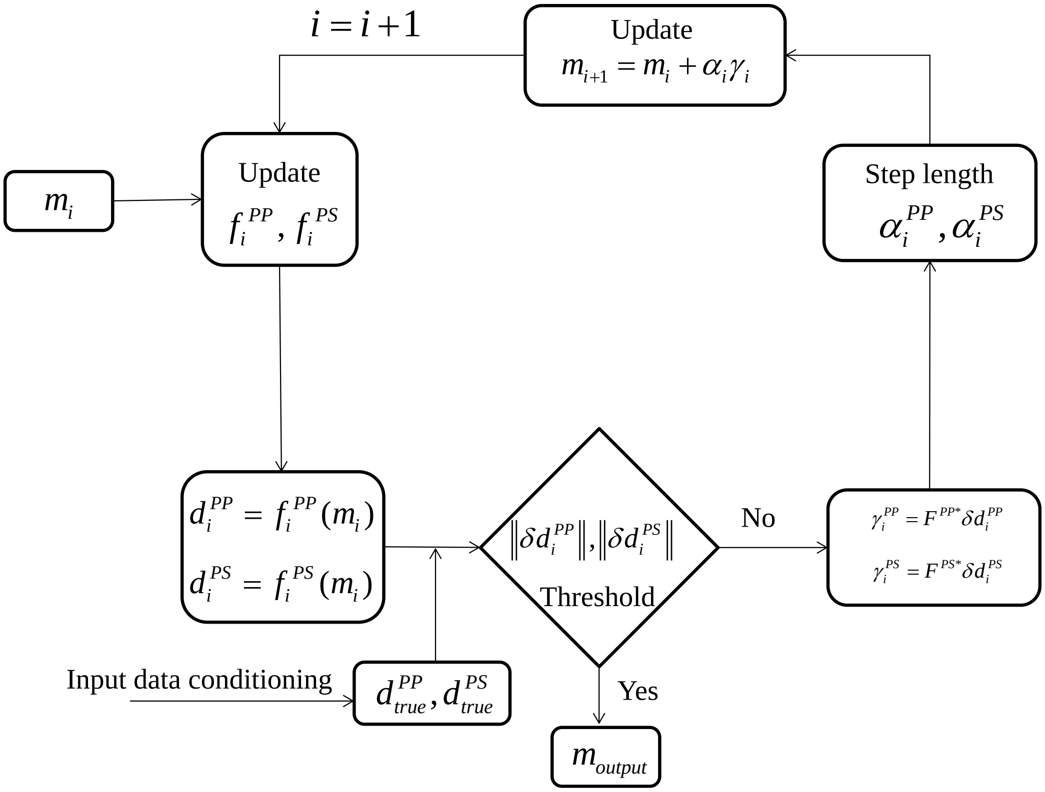

Figure 4-6: Simplified workflow for updating the elastic model $m(v_P, v_s, \rho)$ using the PSTM method. The superscript * is the migration/inversion operator.

4.6 Numerical implementation for gradient estimation

Figure 4-6 shows a geological model where the elastic properties vary in different depth. The model is mapped to P-to-P time. The source and receivers are on the surface. Figure 4-7 demonstrates the different radiation patterns and reflectivity of scattered P-to-P and P-to-S wave fields. For all individual shot records, each scatter point response is migrated to its P-to-P time (e.g., Figure 4-4). By gathering all migrated shot data, we are able to sort all individual scatter point responses to form a common image gather. Since the algorithm is based on the common travel time of scatter points, the travel time acts as a pseudo-depth and removes the need for ray tracing. For complex structures one may add the ray tracing to the algorithm.

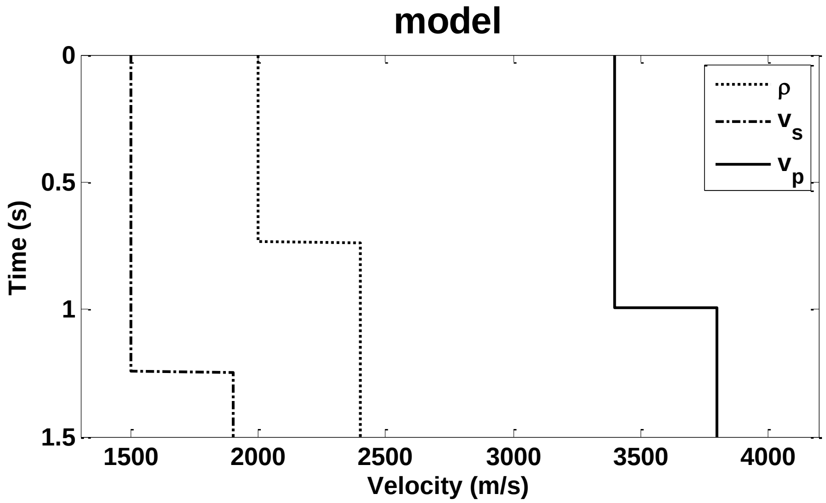

Figure 4-7: Geological model having changes in elastic properties at three different depths. The unit for density is kg/m^3.

The multiparameter gradient function is obtained in a similar way to conventional AVO inversion. For each scatter point, two systems of equations are formed for P-to-P (to solve for three unknowns Δv_P, Δv_S and ρ) and for P-to-S (to solve for two unknowns Δv_S and ρ). An example of this operator at 0.75 s is shown in Figure 4-9. The initial model operators coefficient is produced from smoothed model. The comparision of the operators from smoothed and true model shows that the operator for the inversion is more dependent on the knowledge of the velocity field at far offsets. In addition, note the similarity of inversion operators of Δv_P and $\Delta\rho$ for P-to-P wavefield and Δv_S and $\Delta\rho$ for smaller incident angles. This creates a deficiency in rank of the inversion matrix. For this problem, we need to identify the density field in the real data to enhance the gradient functions.

The inversion of P-to-P and P-to-S data can be done separately or simultaneously; however, simultaneous inversion is more stable because the results can be combined and compared with well log data. Note that the term “simultaneous inversion” refers to the travel time; it is different from other authors' s terminology, which assumes a relationships between v_P , v_s and ρ to reduce equations (4.8) and (4.9) to two equations and two unknowns. Examples of their strategy vary from Garner's relationship (Smith and Gidlow; 1987, Stewart, 1990) or a constant v_P to v_s ratio. Without loss of generality, we can implement them in the frame of FWI for gradient calculations.

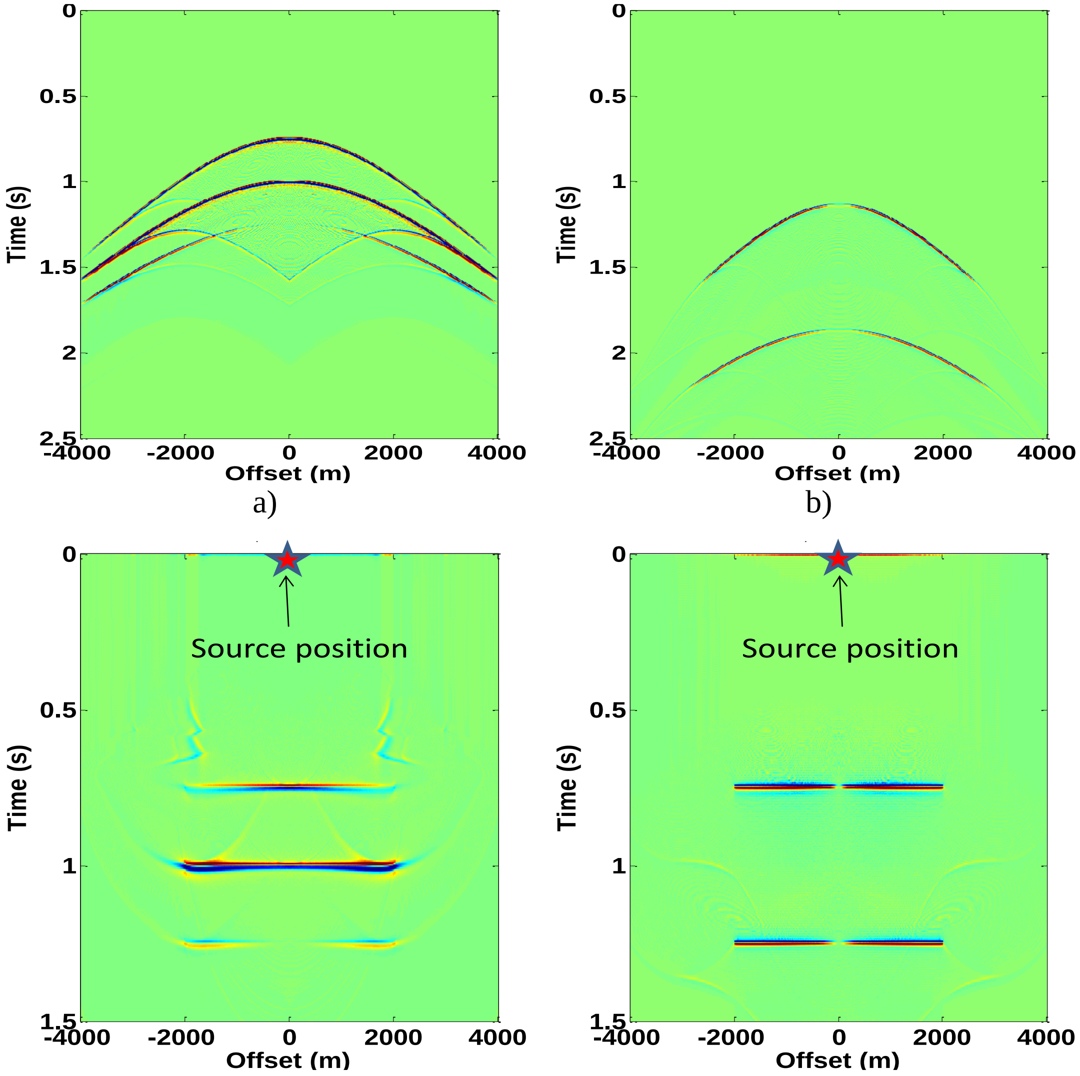

a) b)

c) d)

Figure 4-8: Radiation patterns and reflectivity of a scattered wave field recorded at surface. The model is shown in Figure 4-6 and the offset corresponds to the source position. a) The vertical component of a shot record of P-to-P data. b) The horizontal component of a shot record of P-to-S data c) The migration of (a) with true amplitude correction d) The migration of (b) with true amplitude correction.

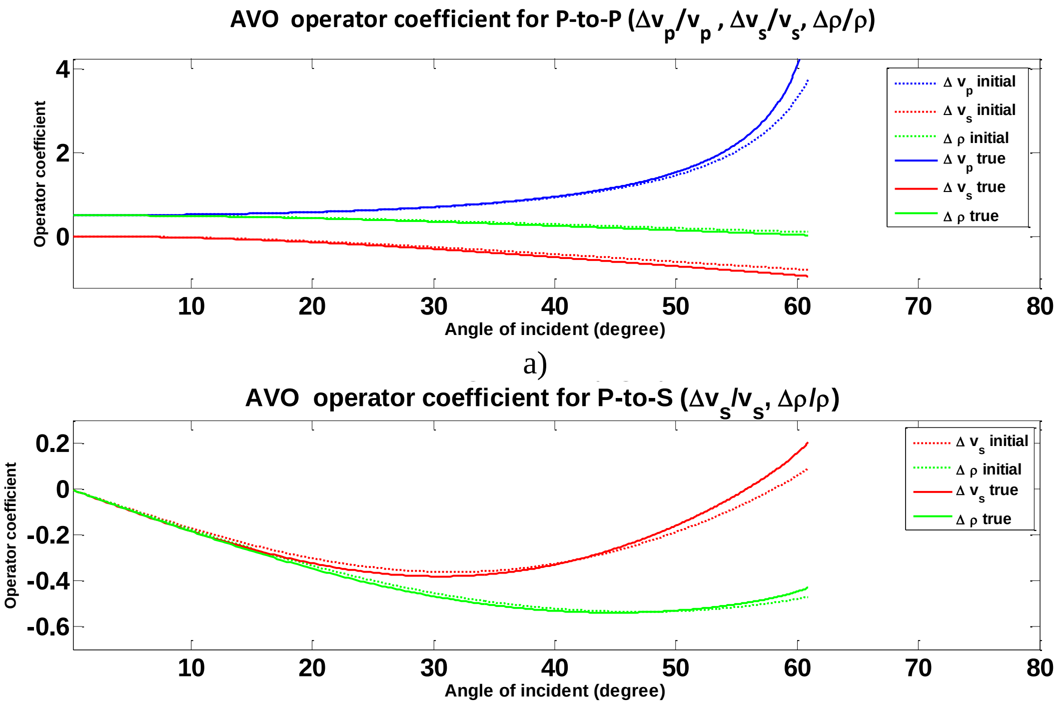

a)

b)

Figure 4-9: A sample scatter point: the angle-dependent matrix operator coefficient (linearized AVO matrix) based on Aki and Richard (1980) for: a) P-to-P radiated waves b) P-to-S radiated waves. Note that the legend shows that dotted lines are initial models.

4.7 Description of the inversion process

In this section, the estimation of gradient function using reflectivity function is illustrated by numerical examples. Figure 4-10 displays a numerical estimation of the P-to-P and P-to-S reflectivity data from a single shot in a 1-D geological model with an upper horizontal layer with $v_p = 3000$ m/s, $v_S = 1500$ m/s and $\rho = 2000$ kg/m3 and a lower horizontal layer that has $v_p = 4000$ m/s, $v_s = 2000$ m/s and $\rho = 2300$ kg/m3. For demonstration purposes let us assume that the final output of the migration/inversion is a delta function with the amplitude of the reflectivity. Figure 4-10a and Figure 4-10c show the migrated/inverted data residual between the true data reflectivity of the P-to-P and P-to-S waves (R_{pp}^{true} and R_{ps}^{true}) located at the true depth z^{true} and the modeled reflectivity R_{pp}^{m} and R_{ps}^{m} located at initial depth z^{m}. The angle-dependent elastic parameters for calculation of the P-to-P data residual $\mathrm{I}_{pp}^{residual}$ from the Zoeppritz equations can be written as

$$\mathrm{I}_{pp}^{residual} = R_{pp}^{true} - R_{pp}^{\mathrm{m}}(\Delta v_p, \Delta v_s, \Delta\rho), \tag{4.12}$$

which is defined for P-to-P wave. In the shot record, for normal incident P-wave, the contribution of Δv_s is neglected. Similarly, for the P-to-S wave at an arbitrary non-normal angle of incidence $\theta = 20^\circ$ we have

$$\mathrm{I}_{ps}^{residual} = R_{ps}^{true} - R_{ps}^{\mathrm{m}}(\Delta v_s, \Delta\rho), \tag{4.13}$$

where for $\mathrm{R}_{ps}^{\mathrm{m}}$, the reflectivity has been scaled to a non-normal angle of incidence ($\theta^{ps} = 20^\circ$). An integration of the data residual (Figure 4-10b & Figure 4-10d) is equivalent to the gradient for all parameters. The P-to-P wave is expressed as

$$\delta\boldsymbol{m}(\delta v_p, \delta v_s, \delta\rho) = \alpha^{pp}\int \mathrm{I}_{pp}^{residual}(z)dn \tag{4.14}$$

Similarly for P-to-S wave we have

$$\delta\boldsymbol{m}(v_s, \rho) = \delta v_s(z) + \delta\rho(z) = \alpha^{ps}\int \mathrm{I}_{ps}^{residual}(z)dn, \tag{4.15}$$

where for a flat reflector, n is the z direction. Note that in equations (4.14) and (4.15) , the variables z and τ are interchangeable using depth-to-time (or time-to-depth) conversion techniques (e.g., Hubral, 1997).

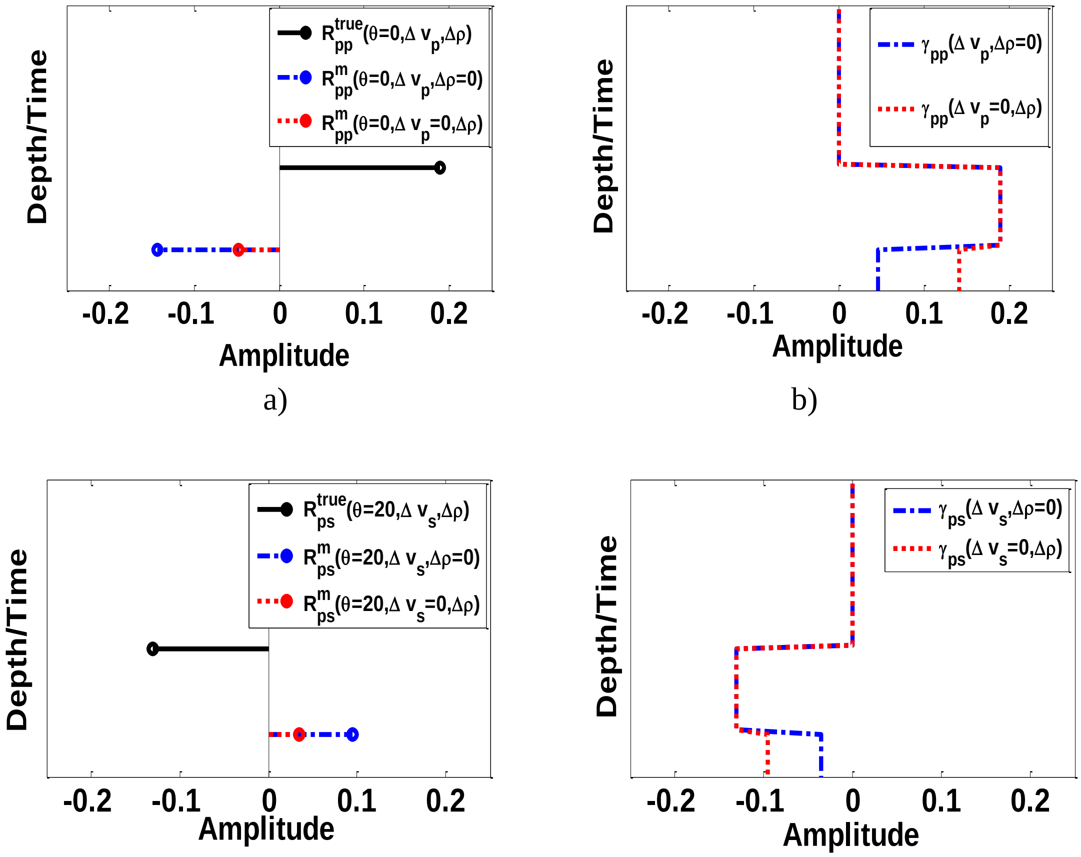

a) b)

c) d)

Figure 4-10: A numerical example of FWI and the contribution of elastic properties to the gradient calculation. a) The true amplitude migrated P-to-P data residual after removal of the source signature (assuming full band reflectivity is a spike). b) Integration of Figure 4-10a to give the gradient function of P-to-P data. c) The true amplitude migrated P-to-S data residual after removal of the source signature (assuming full band reflectivity is a spike). d) Integration of Figure 4-10c to give the gradient function of P-S data.

4.8 The effects of data noise and band limitation on FWI

Figure 4-11 demonstrates the effects of low SNR and limitation of frequency bands of the signal which are two common problems found in recorded data. The blue curve in Figure 4-11a is a data residual signal to be added to the noise with a Gaussian distribution as shown by the brown curve. The integration of the noisy residual is shown by the dotted black curve. The integration of Gaussian distribution produce fluctuation on the shape of gradient function but it does not have strong effect on its shape. Tarantola (1984) suggested using appropriate smoothing operators to improve the inversion result. In this study, for the available recorded field P-to-S data that has low

SNR, all the data are migrated and visual comparison is used to determine the step length. Further discussion on this issue is found in our field data example. We also note that the reflectivity functions of field data are band-limited. Figure 4-11b is compares the integration of reflectivity R with the integration of bandlimited R within range of 5 Hz to 45 Hz. The band-limited reflectivity functions produce artefacts in the inversion. The lack of zero frequency causes the integral output of equations (4.14) and (4.15) to not produce an accurate gradient function, which should be a perfect step function as in Figure 4-11b. For more examples of artefacts on band limitation, the reader is referred to Bleistein et al. (2001), Innanen (2011) and Kroode (2013).

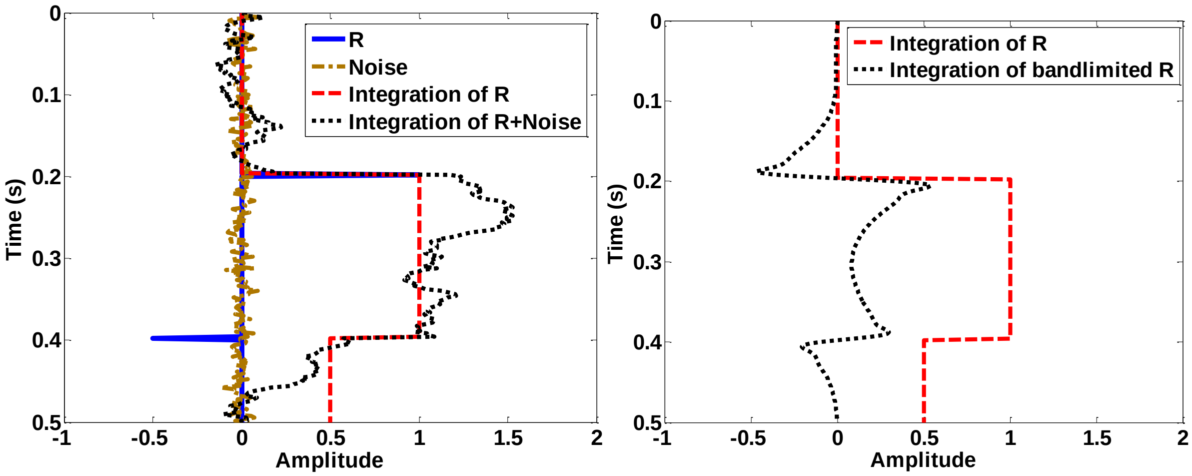

a) b)

Figure 4-11: Numerical considerations of FWI. a) The influence of random noise on the gradient function. b) The influence of band limitation (low cut 5Hz filtered data residual) on the gradient function.

4.9 The initial model and data conditioning

As in the inversion strategy proposed by Tarantola (1986), we can first invert for Δv_p and Δv_s, then invert for $\Delta\rho$. The starting v_p and v_s can be obtained by conventional velocity analysis such as prestack migration gathers or available well log information. The updated model is used to update the forward modeling operator f and its migration/inversion F^* to improve the travel time in each step. This is done using the relationship between the updated interval velocities to RMS velocity (Dix, 1955). The data conditioning of the full wave field examples were studied by several authors (e.g., Sears et al., 2008 and Warner et. al., 2013). However, in time imaging techniques, the procedure of waveform inversion is slightly different because it is based on the linearization of seismic reflection data (primary reflection data). Therefore, in real field data we will have to eliminate noise and preserve true amplitude in order to minimize the objective function. Noise in this case is any signal that is not a reflected wave and is not included in the forward modeling. Examples of noise are multiples, surface waves, surface related noise, and dead traces. The effects of the source wavelet should be removed from data residuals by appropriate deconvolution methods prior to calculating the gradient function. As previously stated improvements in the bandwidth of the signal can improve gradient functions.

4.10 Conclusions

An inversion method based on Kirchhoff approximation (e.g., Bleistein, 1984) has been developed. The advantage of the Kirchhoff approximation is that both of forward and inverse problem deal with change of elastic properties across bedding interfaces compared to the Born approximation that consider variation of model parameters. Consequently, the shape of scattering potential of Born approximation is step-like while the shape of reflectivity functions of Kirchhoff approximation is spike like with respect to reflectors normal vector (see e.g., Beylkin and Burridge, 1985, Jaramillo and Bleistein, 1999, Kroode, 2013 and Shaw and Sen , 2004). The method is more stable than the Born approximation because the output of the inversion of spike-like properties provide more stable tie with well control for band limited data (Bleistein, 1987). The Kirchhoff approximation is applied in the framework of FWI in the steepest descent inversion scheme and the gradient functions are obtained by AVO inversion of data residual and integrating in the direction of the vectors perpendicular to the reflectors (i.e., normal rays). The gradient is scaled and used for updating the current model, forward, migration with AVO inversion operators. To overcome with large computational burdens of elastic wave solutions, the forward modeling and inversion operators are based on time imaging methods. It requires updating the model in time and it comprises diffraction stack weighting of PSTM that is formulated by Double Square Root (DSR) equation. The approach is efficient for smoothly lateral variation of model, however, for the geologically complex structures the ray tracing techniques can be used to enhance the overcome the limitation of forward modeling and its migration operators.

Chapter 5: Numerical examples of multiparameter elastic waveform inversion

5.1 Introduction

The inversion result of synthetic and field data examples are presented to demonstrate the efficiency and limitation of FWI method for different data sets. I first show the successful inversion result of multicomponent P-to-P and P-to-S data obtained from a simple model that has a layer with constant P-wave velocity but with change in S-wave velocity. In the subsequent example, I use a more complicated model obtained from a real well log data set. I show that the forward modeling provides the radiation pattern of the forward modeling that can be visible in the migrated image as real and imaginary component used in waveform inversion process. The first field data example consists of a Nexen Energy ULC multicomponent data set (e.g., vertical and radial components) with limited offset. The second field example is provided with long offset but only the vertical component is available. The third example is inversion result of low SNR of a SH-to-SH data obtained from lateral component of a wavefield that has shear source. Most of the processing steps have been performed with Matlab programming codes. In addition, Vista processing software was used for true amplitude compensations such as attenuation of field data.

5.2 Synthetic numerical example: P-P and P-S blocky model

The true, starting, and inverted velocity, for the P- and S- waves of a 1D synthetic geologic model are shown in Figure 5-1. The second layer has no change in P-wave velocity, but an increase in S-wave velocity. The inversion scheme considers the mode-converted P-to-S waves that form at interfaces. The dominant frequencies of the minimum phase wavelets employed are 5-13 Hz. P-wave velocity are inverted from P-to-P data and S-wave velocity is obtained from P-to-S data. Both P-wave velocity and S-wave velocity inversions performed well, recovering the main features of the model, including the low impedance contrast of the S-wave in the second layer.

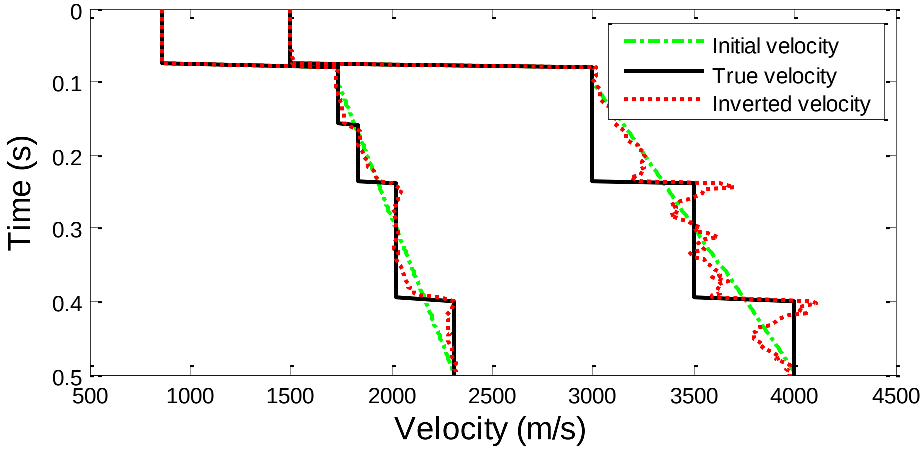

Figure 5-1: Velocity inversion result of a synthetic blocky model using P-to-P and mode converted P-to-S data for P- wave velocity and b the S-wave velocity.

5.3 Synthetic numerical example: P-P and P-S well log model

A synthetic numerical model (Figure 5-2a) was created from an available well log measured in North East British Columbia (NEBC). The Kirchhoff operators for the forward modeling produced a single shot record, with a maximum of 4000m offset in split spread configuration with a receiver spacing of 12.5m. A minimum phase wavelet with a dominant frequency of 45 Hz was arbitrarily chosen. The Kirchhoff and Zoeppritz approximation are based on boundary conditions at reflection surface as shown in Figure 4-1. The changes of velocity, density and angle of incident and transmitted waves at reflection boundary facilitate modeling for rays beyond the critical angle which enhances the forward modeling and AVO inversions (Simmons and Backus, 1996 and Downton and Ursenbach, 2006). The phase variation with offset is a part of reflectivity function of Kirchhoff approximation and as shown in Figure 5-3 can be estimated using the modeled data. Figure 5-3 is produced by applying PSTM operator on data from Figure 5-2. Hence, using phase estimation of forward modeling the true data can be corrected in phase and be used for inversion. Making use of the radiation pattern of scatter points, two least squares engines are implemented in each step for P-to-P and P-to-S data. Figure 5-4 compares the differentiated true model, which is convolved with a wavelet and scaled, with the inverted reflectivity. The good a match with the true model is obtained because of consistent forward modeling and inversion operators.

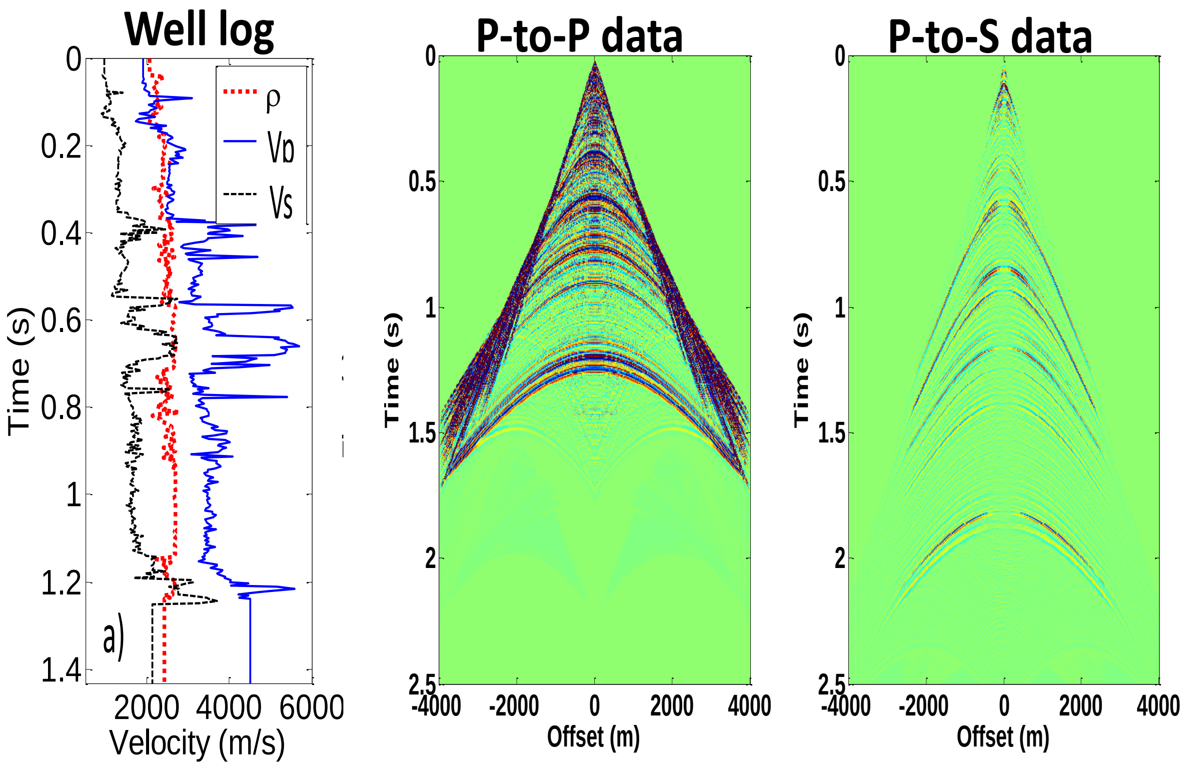

a) b) c)

Figure 5-2: Radiation patterns and reflectivity of scattered wave field modeled from a real well log data using Kirchhoff operator. a) Well log data. b) The vertical component of shot record of P-to-P data c) Shot record showing the horizontal component of P-to-S data.

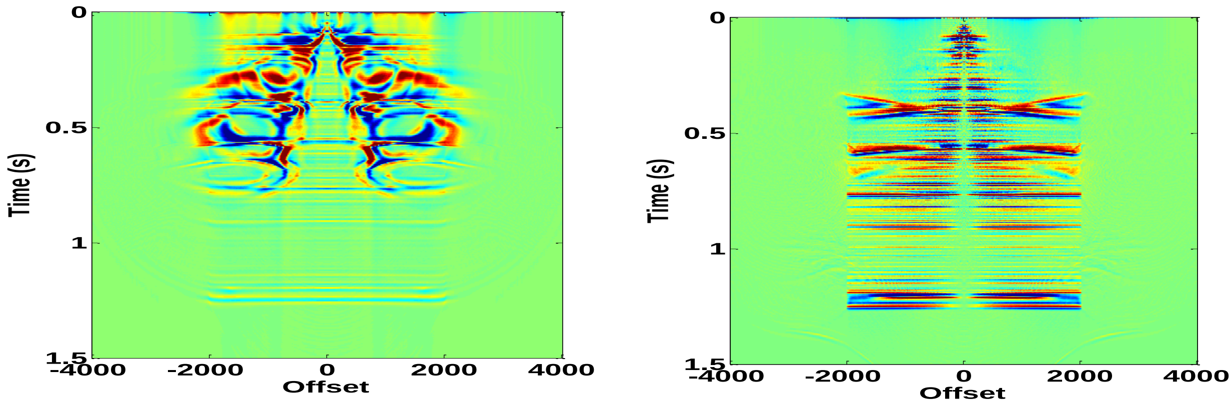

a) b)

Figure 5-3: Radiation patterns of a scattered wave field in prestack gathers. a) the migration of real part of Figure 5-3b. b) The migration of real part of Figure 5-3c.

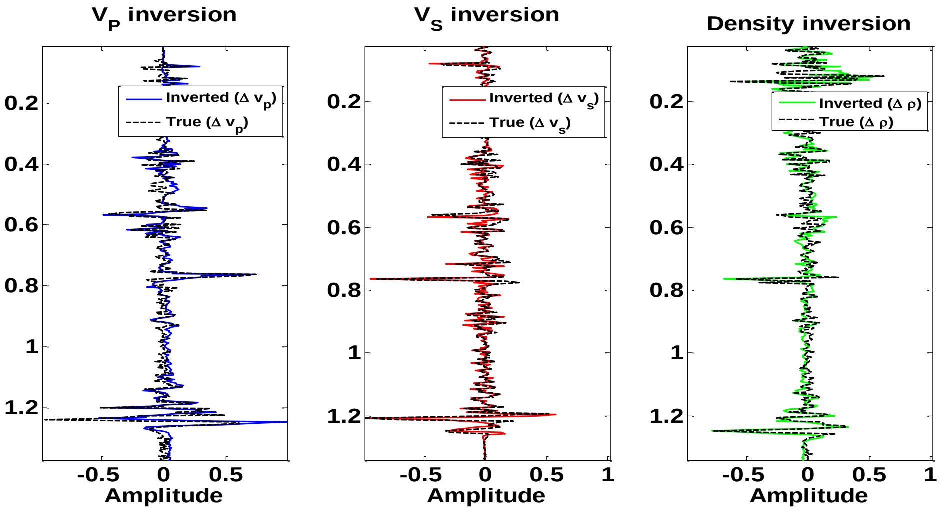

a) b) c)

Figure 5-4: Synthetic model multiparameter inversion. a) Inverted P-wave velocity. b) Inverted S-wave velocity. c) Inverted density. Corresponding well log data are plotted as dotted lines. To perform a comparison the well data is differentiated and convolved with a suitable wavelet.

5.4 A field data example: velocity inversion (NEBC)

In this part, I apply FWI method on the real data sets obtained from a geological model of NEBC. Since the elastic properties of the model have smooth lateral variation, the traveltime estimation for both of forward modeling of shot records and the migration/inversion of data are based on DSR approximation. The vertical and radial component of data is available for inversion process, but the maximum offset and incident angle of the reflected waves are limited to 1000-1500m for example. Due to this limitation, I performed P-wave velocity inversion from P-to-P data and S-wave velocity inversion from P-to-S data.

5.4.1 Data set and basic processing steps

We chose 51 shot records that were acquired by Nexen Energy ULC in the Northeast British Columbia (NEBC) region of Canada. The receiver spacing is 10 m and the source spacing is 60 m. The source type was Vibroseis used in vertical vibration mode. The sample rate was 4 ms and the maximum offset for P-to-P and P-to-S data are arbitrarily chosen to be 1000 m and 1500 m, respectively. The vertical and radial components of the 3C geophones were employed and are assumed to contain predominantly P-to-P and P-to-S waves, respectively. For the limitation of offset in our data a reliable density could not be reconstructed, so we aim to invert for V_P from P-to-P and V_S from P-to-S data.

Well log information in the study area is shown in Figure 5-2a. To obtain the true amplitude of P-to-P data, transmission loss and spherical divergence are considered in the forward modeling. Attenuation compensation (Kjartansson, 1979) with Q=80 for shallower events (0-0.7 s) and Q=120 for deeper (0.7-1.5 s) was applied to the data. For the P-S data, attenuation compensation with Q=45 for shallow (0-1 s) and Q=80 for deeper events (1-2 s) was applied. Spherical divergence (Miao et al., 2005) and transmission loss compensation have been applied on P-to-S forward modeling. A typical raw source record of vertical component data in Figure 5-5a is compared with the processed data in Figure 5-5b. The P-to-S data has smaller SNR compared to P-to-P data. In Figure 5-6a, the radial component shot record is compared with processed radial component data in Figure 5-5b. because of the low SNR the expected reflection events are shown by its synthetic P-to-S data in Figure 5-5c.

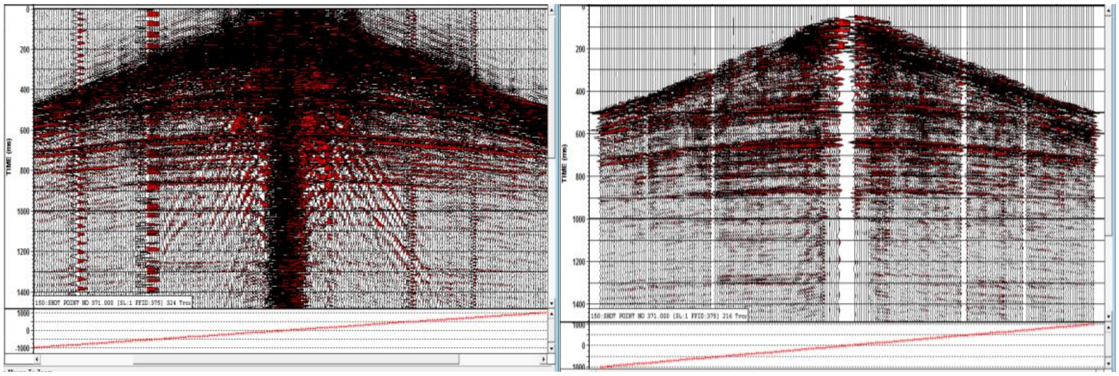

a) b)

Figure 5-5: P-to-P shot record processing a) Vertical component of a sample raw shot record data b) processed shot record

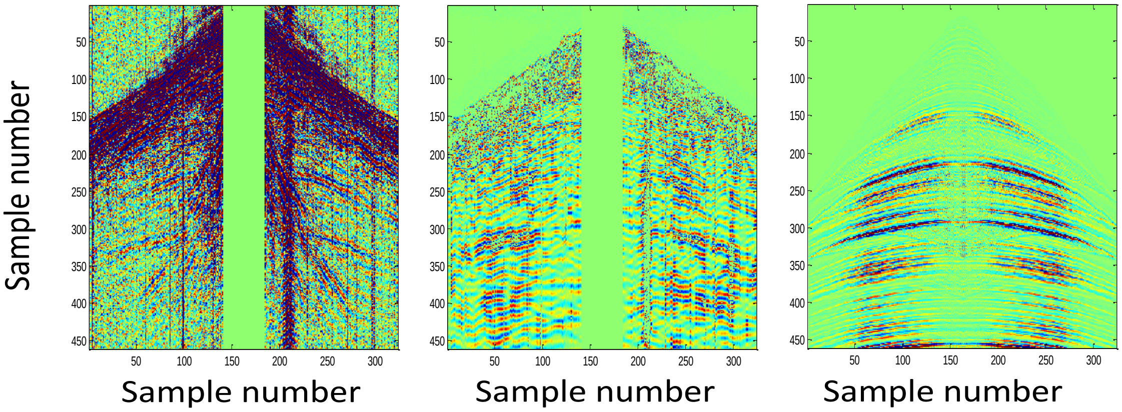

a) b) c)

Figure 5-6: P-to-S shot record processing a) radial component of a sample raw shot record. b) processed shot record. c) corresponding forward modeling. Vertical and horizontal axis are sample numbers in time and space respectively, with $\Delta t = 4$ ms and $\Delta x = 10$ m.

5.4.2 Inversion procedure

To perform quality assurance on the forward operator, the results of forward modeling of all shots are migrated and then compared with the migrated section of real data (see Figure 5-7 and Figure 5-8). Figure 5-7a and Figure 5-7b are the PSTM of 51 field and modeled P-to-P records respectively. Figure 5-7c and Figure 5-7d are the PSTM of 51 modeled and field P-to-S records respectively. The PSTM imaged the events to P-t-P time which is similar to P-to-P images. Higher amplitude compensation at the time $\tau = 1.0$ s in Figure 5-8d is due to the attenuation (Q) logarithmic factor applied to field shot records to be calibrated to the modeled data in Figure 5-8c.

Given the low SNR of the field data, we can visually compare the migrated residuals to find an optimum α. Mathematically, this means that for the purpose of quality assurance the objective function of equation (2.4) is coupled with $\|\Delta m\|^2$ such that

$$\min J = \|\delta d\|^2 + \mu_{reg} \|\Delta m\|^2 . \tag{5.1}$$

where μ_{reg} is the regularization parameter. Equation (5.1) is similar to the objective function of Tarantola (1984) that include the regularization based on model perturbation; however, the slight difference is that instead of δm the differentiated Δm, which is a spike-like function of migrated/inverted reflectivity function, is used. Here, to overcome the problem of numerical convergence of equation (5.1), the band-limited spike-like reflectivity is used for visual comparison as it is easier to identify (see e.g., Figure 4-11b or Bleistein et al., 2001). In this thesis, equation (5.1) is used to include prior knowledge of model into inversion since low SNR level makes the problem ill-conditioned. In the presented example, this numerical approach was not performed automatically for quality of data and forward modeling restrictions to include the full wavefield. Instead, a visual comparison panel was used.

The inversion result of P-wave and S-wave velocity is shown in Figure 5-9. The initial velocity for inversion was obtained using a linearization of the well log as depicted in Figure 5-10. The migration algorithm was not efficient for shallow reflectors, so data is inverted for reflectors deeper than 0.5 s on the vertical component (assumed to be P-to-P dominant) and 0.3 s for radial component (P-to-S dominant). The lack of low frequency contents of seismic data prevented the integration of reflectivity function to produce an ideal step like gradient function. Consequently, as shown by the color scale in the Figure 5-9, the inversion result is displayed only within the range of 2000 to 6000 m/s for the P- wave and 1000 to 2200 m/s for the S- wave velocity inversion. However, the lateral variation of the resulting inversion shows good correlation with the well log data. To improve the inversion result, the low frequency components of the well log were added to the gradient function in order to update the velocity. As shown in Figure 5-10, the final inversion result showed good correlation with well log information.

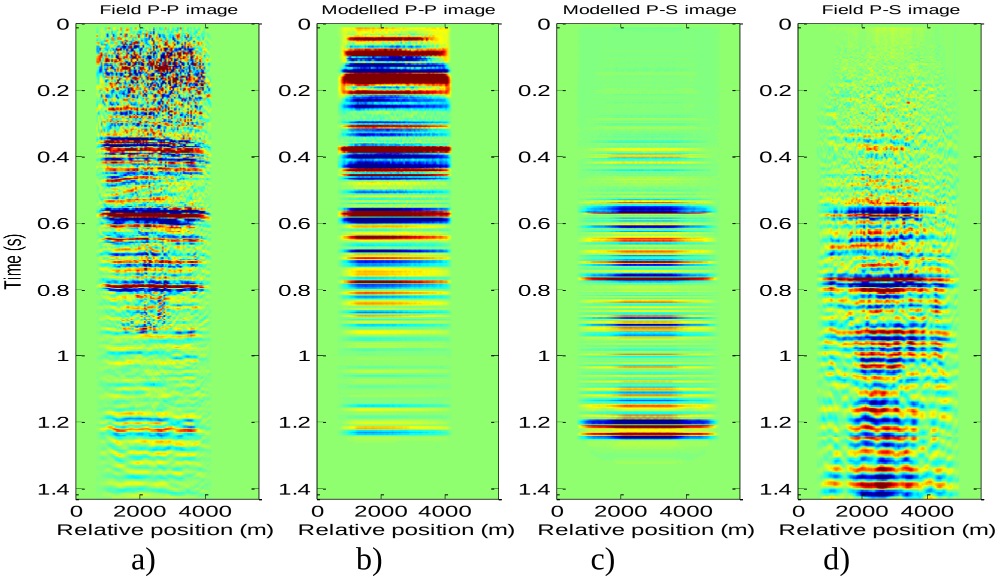

Figure 5-7: Comparison of PSTM mapped in P-to-P time. a) Migrated field P-P data b) Migrated modeled P-P data c) migrated modeled P-S data d) migrated field P-S data.

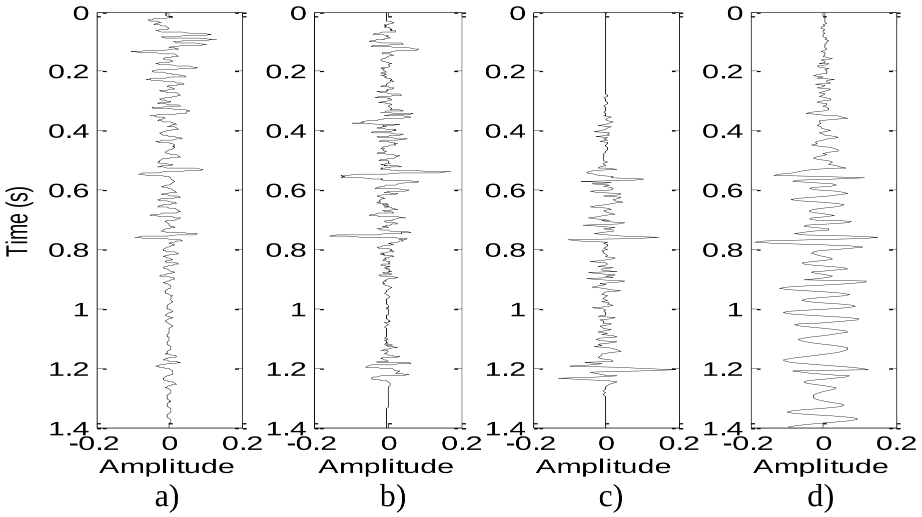

Figure 5-8: Comparison of migration results at a control well mapped in P-to-P time.. a) Migrated field P-to-P data b) Migrated modeled P-to-P data c) migrated modeled P-to-S data d) migrated field P-to-S data.

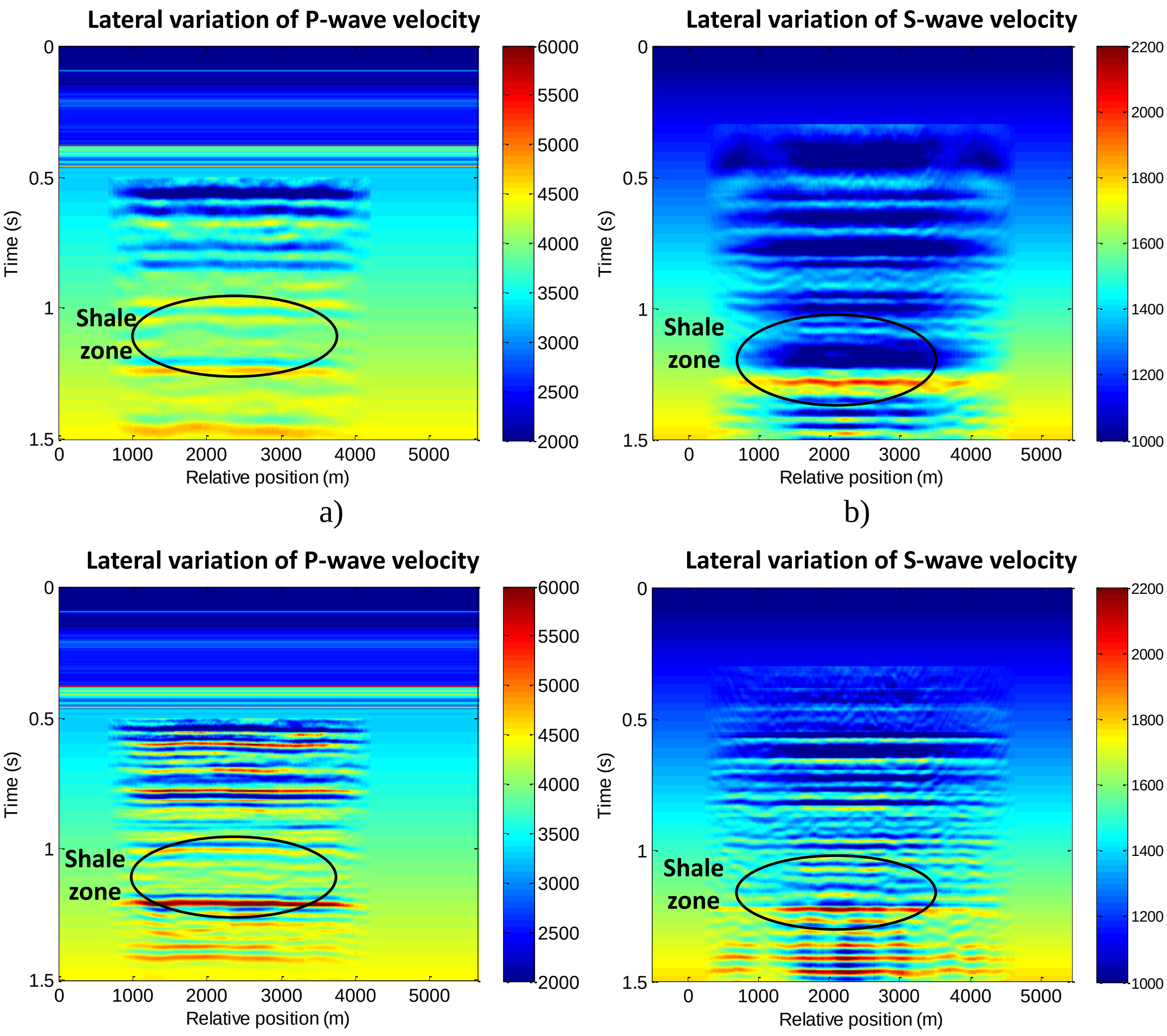

a) b) c) d)

Figure 5-9: P-to-P and P-to-S iterative waveform inversion a) initial inversion from P-to-P data. b) Initial inversion from P-to-S data. c) Updated after three iterations d) Updated after three iterations.

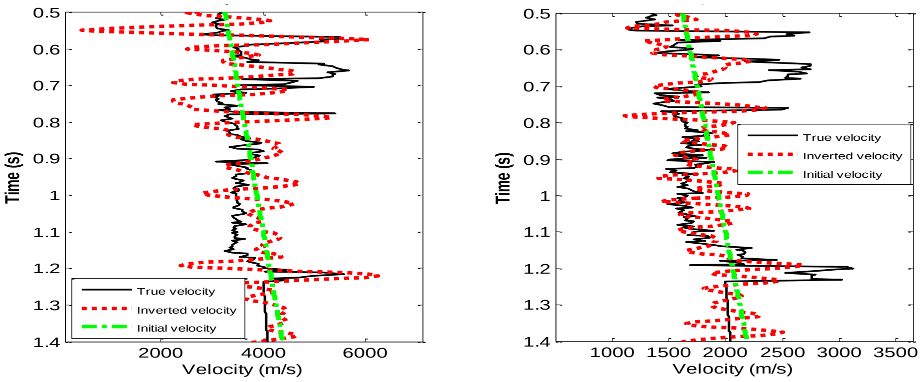

a) b)

Figure 5-10: Inversion results at a control well. a) P- wave velocity, b) S- wave velocity compared with sonic well log (solid blue curve). The low frequency band from the well log is added to the gradient function. Initial model is shown as a green dotted line.

5.5 Field data example: multiparameter elastic inversion (NEBC)

A conventional CMP gather from 3D survey in NEBC was provided by a service operator to test the result of iterative inversion. The CMP gather is positioned in the same position relative to well control that is shown in Figure 5-2a. As shown in Figure 5-11 it has a longer offset range compared to previous data sets so that greater angles of incidence make multiparameter inversion more feasible. It is assumed that the data is processed for true amplitude and multiple elimination. Unfortunately, only P-to-P data is available at this time. An initial model is created by smoothing the available well log data which is shown in Figure 5-2a. Similar to the synthetic example in Figure 5-4, Figure 5-12 compares the differentiated true model (convolved with wavelet and scaled) with the inverted reflectivity. The final inversion result improved the initial result. For example, the shape of final Δv_P, Δv_S and $\Delta\rho$ is closer to the well log data in shallower horizons (e.g., around 0.8 s); this is expected since the AVO operators are nonlinear and once they are updated give more accurate results. This simple example demonstrates the importance of adding the iterative inversion scheme to the current standard direct prestack inversion. Another advantage of this method is the implementation of forward modeling, which could help to identify data type before noise removal. For example the shallow signals were shown to be direct waves and are filtered in Figure 5-11b.

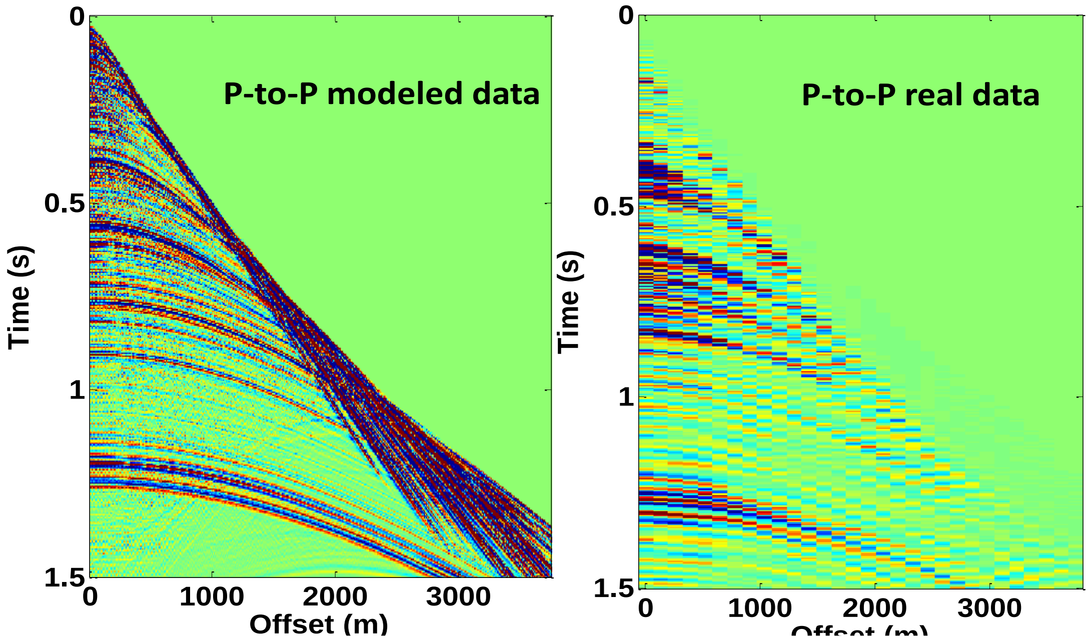

a) b)

Figure 5-11: Iterative inversion of a CMP gather obtained from 3D data in NEBC. a) The forward modeling result. b) The real data result.

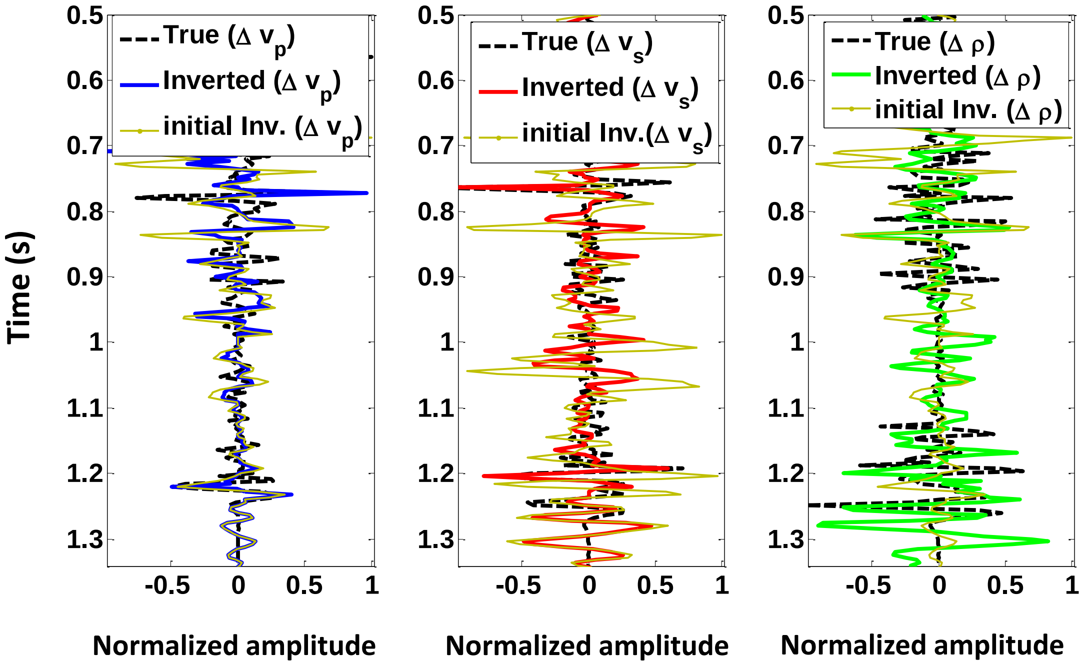

a) b) c)

Figure 5-12: Iterative inversion of a CMP gather obtained from a 3D survey in NEBC. a) The perturbed P- wave velocity, v_P . b) The perturbed S- wave velocity, v_S . c) The perturbed density, $\Delta\rho$.

5.6 Field data example: shear velocity inversion from SH-to-SH wavefields

In addition to vertical and radial components data using a vertical Vibroseis source, a recorded horizontal components using a Vibroseis source in horizontal shear mode is examined for inversion. As shown in Figure 5-13, a conventional velocity analysis has been done by forming an S-to-S wave field CSP gather. As shown in Figure 5-14a, this approach can provide the low frequency component of the shear wave velocity. The low SNR prevented an accurate picking of the events. Figure 5-14 displays a Band Limited Impedance (BLIMP) inversion (Ferguson and Margrave, 1996) of poststack SH-to-SH migrated section. The BLIMP algorithm adds the low frequency of a well log to the integrated reflectivity of the poststack section. In FWI method one can take advantage of the BLIMP methodology to estimate the gradient function by including the low frequency well data.

As shown in Figure 5-14, after 1.5 s (SH-to-SH time) the inversion gives better correlation with the well log data and the v_s inversion from P-to-S data. Accurate deconvolution, true amplitude and phase corrections could enhance the result of inversion.

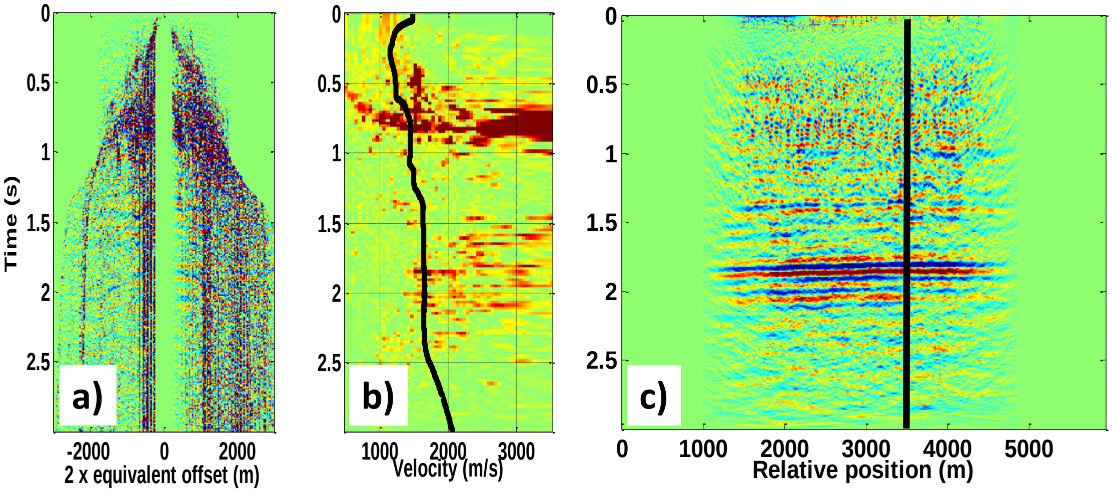

a) b) c)

Figure 5-13: Shear velocity analysis. a) Sample CSP gather for conventional velocity analysis. b) Hyperbolic semblance of (a). The black line indicates the RMS velocity obtained from well log c) The migration of the SH-to-SH data. The vertical black line shows the location of CSP gather.

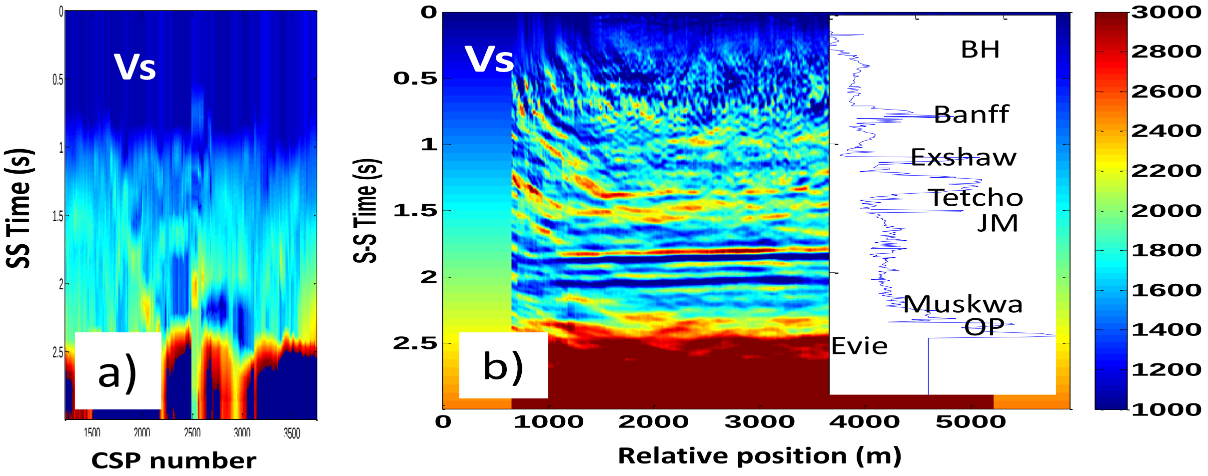

a) b)

Figure 5-14: Shear velocity inversion. (a) The picked velocity from semblance of CSP gathers. b) One step inversion of SH-to-SH wavefield using poststack inversion (Ferguson and Margrave 1998). The shear velocity is assumed to be the dominant contributor of the reflectivity. As shown in Figure 5-13a, the level of SNR is low, so iterative inversion was not successful.

5.7 Conclusions

FWI method has been performed on synthetic and field data example. The inversion of elastic properties from P-to-P and P-to-S requires little iteration to converge for two reasons: firstly, the forward modeling and inversion are consistent and secondly, the source signature is known and the band limitation of the data is under the control of processor. For the real data examples, two perspectives are considered, one is to demonstrate the efficiency of simultaneous P-to-P and P-to-S migration/inversion schemes. This is done by migrating the P-to-P and P-to-S data into the P-to-P traveltime domain and comparing the inversion results with well log data available in study area. Two, to illustrate the problems and suggest solutions for processing steps required to implement FWI method on real data. For example, true amplitude processing of forward modeling and migration/inversion, effects of data band limitation and poor SNR ratio of input data are discussed. Although, there are several techniques available to improve the SNR, band limitation, data true amplitude recovery, statics corrections, etc., which could be applied in the presented processing steps of the input data.

Chapter 6: Discussions and conclusions

I implemented the method of PSTM for the iterative inversion of subsurface elastic properties from seismic reflection data. To calculate the traveltime, the RMS velocity is used that is calculated from the interval velocity using Dix’s (1955) approximation. Dix’s (1955) hyperbolic approximation of traveltime is accurate with a small offset-to-depth-ratio and can handle the vertically inhomogeneous medium. For such a problem, one may refer to the proposed Taner and Koehler (1969) formulation that uses a higher-order Taylor series approximation of the travel time. In addition, for AVO operators the ray path is assumed to be straight. The assumption of a straight ray path usually underestimates the angle of incidence of the waves propagating in heterogeneous multilayer velocity models. For better approximation of the angle of incident waves, one may refer to Ostrander (1984) who considered the arc ray path of a medium with interval velocity v_I which varies linearly with depth from an initial velocity v_0 (e.g. $v_I = v_0 + Kz$ where K is a constant) .

Conventional methods of Full Waveform Inversion (FWI) rely on depth-imaging methods which are computationally expensive and prevent its use in commercial applications. It is shown that implementation of current two-way wave equation migrations such as Reverse Time Migration (RTM) requires multiple elimination due to limitation of the imaging conditions. Hence, in this thesis the one-way wave equation is used for both forward modeling and inversion scheme. In this direction, the mathematical formulation of FWI method is described based on the first order Born approximation. It is shown that the boundary condition upon reflection surface creates restriction for iterative inversion if volume integral Born approximation is used in forward modeling. This restriction is mainly due to the boundaries of updated background model after the first iteration. Instead the surface integral Kirchhoff approximation was implemented for iterative inversion. This lead an efficient algorithm for multiparameter inversion of the elastic properties using Zoeppritz equations which is consistent with surface integral Kirchhoff approximation.

Efforts has been done for reducing the computational costs of iterative inversion. It is demonstrated that iterative seismic reflection inverse problem can be obtained using standard Prestack Time Migration (PSTM) and corresponding forward modeling. The method updates the models in time and it incorporates accurate diffraction stack weighting of the PSTM data. We have used the linearized Zoeppritz solvers for amplitudes and the Double Square Root (DSR) equation for travel time consideration of P-S and P-P data during the waveform inversion. Compared with Prestack Depth Migration (PSDM), PSTM requires that the geological structure have small lateral variations in elastic properties.

To perform a comparison, the scatterpoint response of Marmousi model simulated using ray tracing and Finite Difference Time Domain (FDTD) are compared with PSTM method using Common Scatterpoint Gather (CSP) of Equivalent Offset Migration (EOM). In this direction, the tilt of traveltime of dipping interfaces in CSP gather is implemented in traveltime of semblance plot of CSP gather and DSR equation which enhanced the image output of PSTM and the focusing of energy in semblance plots.

The multiparameter elastic inversion approach is applicable to all types of reflected wavefields such as P-to-P, P-to-S, S-to-S and S-to-P. Traveltime estimation of forward modeling and migration/inversion operators are based on the DSR equation. All operators involved in inversion, including the background model for DSR and AVO are updated at each iteration. The migration/inversion procedure maps the mode converted waves to the traveltime of incident waves which fixes the registration problem of events that travel from source to scatter point. The inversion of the reflected P-to-P and P-to-S synthetic and field data are provided for the numerical examples.

This approach is applicable for complex structures however, to estimate the traveltime of scatterpoints, ray tracing can be added to the algorithm.

References

Aki, K., and Richards, P. G., 1980, Quantitative Seismology: Theory and Methods, W.H. Freeman and Company. Vol. 1.

Audebert, F., Biondi, B., Lumley, D., Nichols, D., Rekdal, T., and Urdaneta1, H., 2001, Marmousi traveltime computation and imaging comparisons, Stanford Exploration Project, Report **80**.

Bancroft, J. C., Geiger, H. D., Foltinek, D. S., and Wang, S., 1994, Prestack migration by equivalent offsets and CSP gathers, CREWES Research Report.

Bancroft, J.C., 1996, Velocity sensitivity for equivalent offset prestack migration , Ann. Mtg: Can. Soc. Of Expl Geophys.

Bancroft, J. C., Geiger, H. D., and Margrave, G. F., 1998, The equivalent offset method of prestack time migration: Geophysics, **63**, 2042-2053.

Bancroft, J. C., 2000, course note "A practical understanding of prestack Migration": University of Calgary

Beylkin, C., 1985, Imaging of discontinuities in the inverse scattering problem by inversion of a casual generalized Radon transform: J. Math. Phys., **26**.99-108.

Beylkin G., and Burridge R., 1990, Linearized inverse scattering problems in acoustics and elasticity: Wave Motion, **12**, 15–52.

Beydoun, W. B., and Mendes M., 1989, Elastic ray-Born l2-migration/inversion: Geophysical Journal International **97**. 151-160.

Black, L., and M. A. Brzostowski, 1994, Systematics of time-migration errors: Geophysics, **59**, 1419–1434, doi:10.1190/1.1443699.

Read More: http://library.seg.org/doi/ref/10.1190/1.3628016

Bleistein, N., Cohen, J. K., and Stockwell, Jr, J.W., 2001, Mathematics of multidimensional seismic imaging, migration, and inversion: Springer Verlag.

Bleistein. N.. 1984, Mathematical methods for wave phenomena: Academic Press Inc.

Bleistein, N., 1987, On the imaging of reflectors in the earth: Geophysics,**52**, 931–942.

Bleistein, N., Cohen, J. K., and Hagin, F. G., 1987, Two and one-half dimensional Born inversion with an arbitrary reference: Geophysics, **52**, 26-36.

Bleistein, N., Chohen, J. K., Stockwell, Jr., 2001, Mathematics of multidimensional seismic imaging, migration and inversion: Springer Press Inc.

Bortfeld, R., 1989, Geometrical ray theory: Rays and traveltimes in seismic systems (second-order approximation of the traveltimes): Geophysics, **54**, 342-349.

Buske, S., I. Lecomte, T. Nemeth, S. Operto, and V. Sallares, 2009, Imaging and inversion — Introduction: Geophysics, **74**, no. 6, WCA1–WCA4, doi: 10.1190/1.3256872.

Cameron, M., S. Fomel, and J. Sethian, 2007, Seismic velocity estimation from time migration: Inverse Problems, 23, 1329-1369.

Cameron, M. K., 2007a, Seismic velocity estimation from time migration, PhD thesis, University of California.

Cameron, M. and J. Sethian, 2008, Study of a Cauchy problem for a nonlinear elliptic PDE for seismic velocity estimation from time migration: Inverse Problems.

Cary P. W., and Zhang A., 2011, True-amplitude PS prestack time migration via 5D Interpolation: CSPG CSEG CWLS Convention.

Cerveny, V., 2001, seismic ray theory: Cambridge University Press Inc.

Cerveny, V., and Castro M.,2001, Application of dynamic ray tracing in the 3-D inversion of seismic reflection data: Geophys. J. Int., **113**,776-779.

Claerbout, J. F., 1985, Imaging the earth interior: Blackwell scientific publications.

- 1971, Toward a unified theory of reflector mapping: Geophysics, **36**,467-481.

Clayton, W., and Stolt, R. H., 1981, A Born-WKBJ inversion method for acoustic reflection data: Geophysics **46**, 1559-1567.

Claerbout, J. F., 1985, Imaging the earth interior: Blackwell scientific publications.

Cohen, J, .K. and Bleistein, N., 1979, Velocity inversion procedure of acoustic waves: Geophysics, **44**, 1077-1087.

Dix, C. H., 1955, Seismic velocities from surface measurements: Geophysics, **20**, 68-86.

Docherty, P., 1991, A brief comparison of some Kirchhoff integral formulas for migration: Geophysics, **56**, 1164-1169.

Downton, J., and C. Ursenbach, 2006, Linearized amplitude variation with offset (AVO) inversion with supercritical angles: Geophysics, **71**, no. 5,E49–E55.

Fowler, J. F., 1997, A comparative overview of prestack time migration methods: 66th Ann. Internat. Mtg., Soc. Expl. Geophys., Expanded Abstracts, 1571–1574.

Ferguson R. J., and Margrave G. F., 1996, A simple algorithm for band-limited impedance inversion,CREWES annual research report, U of Calgary.

Gajewski, D., Coman R., and Vanelle C., 2002, Amplitude preserving Kirchhoff migration: a traveltime based strategy: Stud. geophys. geod., **46**, 193−211.

Gauthier, O., Virieux, J., and Tarantola, A., 1986, Two-dimensional nonlinear inversion of seismic waveforms: Numerical results: Geophysics, **51**, 1387-1403.

Goldin, S. V., 1986, Seismic traveltime inversion, Soc. Expl. Geophys. Monograph.

Gray, S., 2000, Velocity smoothing for depth migration: How much is too much?: 70th Ann. Internat. Mtg: Soc. of Expl. Geophys., 1055-1058.

Hanitzsch, C., Hubral, P., Schleicher, J., and Tygel, M., 1992, True-amplitude migration of 2-D synthetic seismograms, 47th Ann. Internat. Mtg., Europ. Assoc. Expl. Geophys., Expanded Abstracts, 276-277.

Hanitzsch, C., Schleicher, J., and Hubral, P., 1994, True-amplitude migration of 2-D synthetic data: Geophys. Prosp., **42**, 445–462.

Hanitzsch, C., 1997, Comparison of weights in prestack amplitude-preserving Kirchhoff depth migration: Geophysics, **62**, 1812–1816.

Hubral, P., 1977, Time-migration Some ray-theoretical aspects: Geophys. Prosp. **25**, 738-745.

Hubral, P., Krey, T., 1980, Interval Velocities from Seismic Reflection Time Measurements: SEG Expanded Abstracts.

Hubral, P., Schleicher, J., and Tygel, M., 1992, Three-dimensional paraxial ray properties—I: Basic relations: J. Seis. Expl., 1, 265–279.

Ikelle, L. T., J. P. Diet, and A. Tarantola, 1986, Linearized inversion of multioffset seismic reflection data in the ω − k domain: Geophysics, 51, 1266–1276, doi: 10.1190/1.1442179.

Jin, S., Madariaga, R., Virieux, J., & Lambaré, G., 1992, Two-dimensional asymptotic iterative elastic inversion: Geophysical Journal International, **108**(2), 575-588.

Jaramillo, H. H., Bleistein N., 1999, The link of Kirchhoff migration and demigration to Kirchhoff and Born modeling: Geophysics, **64**, 1793–1805.

Hargreaves, N., 2006, Surface multiple attenuation in shallow water and the construction of primaries from multiples: 76th Annual International Meeting: SEG, Expanded Abstracts, 2689–2693, http://dx.doi.org/10.1190/1.2370080 .

Hubral, P., 1977, Time-migration - some ray-theoretical aspects: Geophys. Prosp. 25, 738-745.

Kamps, B., Smoothing velocities for depth migration: unpublished report, Tsunami Development. http://www.tsunamidevelopment.com

Innanen, K., and Margrave G. F., 2011, Seismic inversion and the importance of low frequencies: CREWES annual research report, U of Calgary.

Innanen, K., 2011, Hidden nonlinearities in the Aki-Richards approximation: CREWES annual research report, U of Calgary.

Jaramillo, H., and Bleistein, N., 1999, The link of Kirchhoff migration and demigration to Kirchhoff and Born modeling: Geophysics, **64**(6), 1793–1805.

Khaniani H., Bancroft J. C., and Margrave G. F., 2012, Full waveform inversion algorithm using Common Scatter Point (CSP) gathers: SEG Expanded Abstracts.

Kjartansson, E. (1979), Constant *Q*-wave propagation and attenuation, J. Geophys. Res., **84**(B9),4737–4748.

Krebes, E. S., 2009, Theoretical seismology: lecture notes, university of Calgary.

ten Kroode, F., 2012, A wave-equation-based Kirchhoff operator: Inverse Problems, **28**(11), 115013.

ten Kroode, F., Bergler, S., Corsten, C., de Maag, J., Strijbos, F., and Tijhof, H., 2013, Broadband seismic data — The importance of low frequencies: Geophysics, **78**(2), WA3–WA14.

Lambaré, G., Operto, S., Podvin, P., Thierry, P., 2003, 3-D ray Born migration/inversion— Part 1: Theory: Geophysics, **68**, 1348–1356.

Leary, P. O., 2004, Direct and specific least-square fitting of hyperbolæ and ellipses: Journal of Electronic Imaging **13**(3), 492– 503.

Margrave, G. F., Bancroft, I. C. and Geiger, H. D, 1999, Fourier prestack migration by equivalent wavenumber: Geophysics, **64**, 197-207.

Margrave, G. 2010, Inversion course note: university of Calgary.

Manning, P. M., 2008, Techniques to enhance the accuracy and efficiency of finite-difference modeling for the propagation of elastic waves, PhD thesis, The University of Calgary.

Margrave, G. F., Ferguson, R. J., and Hogan, C. M., 2011, Full Waveform Inversion (FWI) using one-way migration and well calibration: SEG Expanded Abstracts **30**.

Mi, Y., and Margrave G. F., 2001, Converted-wave prestack depth imaging with the nonstationary wavefield extrapolators, CREWES annual research report, U of Calgary.

Mora, P., 1987, Nonlinear two-dimensional elastic inversion of multioffset seismic data: Geophysics, **52**, 1211–1228, doi: 10.1190/1.1442384.

Mora, P., 1988, Elastic wave-field inversion of reflection and transmission data: Geophysics **53**, 750-759.

Morse, P. M.. and Feshbach, H.. 1953, Methods of theoretical physics: McGraw-Hill Book Co. Vol. 2.

Mulder, W. A., and R.-E. Plessix, 2008, Exploring some issues in acoustic full waveform inversion: Geophysical Prospecting, **56**, 827–841, doi: 10.1111/gpr.2008.56.issue-6.

Operto, S., Lambaré, G., Podvin, P., and Thierry P., 2003, 3D ray+Born migration/inversion—Part 2: Application to the SEG/EAGE overthrust experiment: Geophysics, **68**, 1357-1370.

Ostrander, W., 1984, Plane wave reflection coefficients for gas sands at nonnormal angles of incidence: Geophysics, **49**(10), 1637–1648.

Parson, R., 1986, Estimating reservoir mechanical properties using constant offset images of reflection coefficients and incident angles: 56th Ann. Internat. Mtg., Expanded Abstracts, 617-620.

Plessix, R.-E., 2008, Introduction: Towards a full waveform inversion: Geophysical Prospecting, **56**, special issue on full waveform inversion, doi: 10.1111/gpr.2008.56.issue-6.

Plessix, R.-E., G. Baeten, J.W. de Maag, and M. Klaasen, 2010, Application of acoustic full waveform inversion to a low-frequency large-offset land data set: 80th Annual International Meeting, SEG, Expanded Abstracts, 930–934.

Pratt, R. G., 1999, Seismic waveform inversion in the frequency domain, Part I: Theory and verification in a physical scale model: Geophysics, **64**,888–901.

Shaw, R. K., and Sen M. K., 2004, Born Integral, stationary phase, and linearized reflection coefficients in anisotropic media: Geophysical Journal International, 158, 225-238.

Schneider, W. A., 1978, Integral formulation for migration in two and three dimensions: Geophysics, **43**, 49-76.

Schleicher, J.,Tygel, M., and Hubral, P., 1993, 3-D true-amplitude finite offset migration: Geophysics, **58**, 1112–1126.

Schleicher, J.,Tygel, M., and Hubral, P., 2007, Seismic true amplitude imaging: Society of Exploration Geophysicists.

Sears, T., S. Singh, and P. Barton, 2008, Elastic full waveform inversion of multi-component OBC seismic data: Geophysical Prospecting, **56**, 843–862.

Shearer, P. M., 1999, Introduction to seismology: Cambridge University Press.

Simmons, J. L. and Backus, M. M., 1996, Waveform-based AVO inversion and AVO prediction-error, Geophysics, **61**, 1575-1588.

Sirgue, L., and Pratt, R. G., 2004, Efficient waveform inversion and imaging: A strategy for selecting temporal frequencies: Geophysics, **69**, 1, 231.

Smith, G.C., and Gidlow, P.M., 1987, Weighted Stacking for Rock Property Estimation and Detection of Gas: Geophysical Prospecting, **35**, 993-1014.

Stewart, R.R., 1990, Joint P and P-SV Inversion: CREWES Research Report.

Stolt, H. R., and Weglein, A. B., 2012, Seismic Imaging and Inversion - Application of Linear Inverse Theory: Cambridge University Press.

Sun, J., 1994, Geometrical ray theory: Edge-diffracted rays and their traveltimes (second-order approximation of the traveltimes), Geophysics, **59**, 148–155.

Sun, J., and Gajewski, D., 1997, True-amplitude common-shot migration revisited: Geophysics, **62**, 1250–1259.

———1998, On the computation of the true amplitude weighting functions: Geophysics, 63, 1648–1651.

Taner, M. T., and F. Koehler, 1969, Velocity spectra - Digital computer derivation and applications of velocity functions: Geophysics, **34**, 859-881.

Tarantola, A., 1984a, Linearized inversion of seismic reflection data: Geophysical Prospecting, **32**, 998-1015.

- 1984b, Inversion of seismic reflection data in the acoustic approximation: Geophysics, **49**, 1259–1266.

- 1986, A strategy for nonlinear elastic inversion of seismic reflection data: Geophysics, **51**, 1893-1903.

-1987, Inverse problem theory: Methods for data fitting and model parameter estimation: Elsevier Science Publishing Co., Inc.

Thierry, P., S. Operto, and G. Lambaré, 1999, Fast 2D ray-Born inversion/migration in complex media: Geophysics, **64**, 162–181.

Ursin, B., and Tygel, M., 1997: Reciprocal volume and surface scattering integrals for anisotropic elastic media: Wave Motion, **26**, pp. 31-42.

Vigh, D., and Starr, E. W., 2008, 3D prestack plane-wave, full-waveform inversion: Geophysics, **73**, VE135-VE144.

Verschuur, D., and A. Berkhout, 2005, Removal of internal multiples with the common-focus-point (CFP) approach: Part 2 — Application strategies and data examples: Geophysics, 70, no. 3, V61– V72, http://dx.doi.org/10.1190/1.1925754.

Versteeg, R. J., 1993, Sensitivity of prestack depth migration to the velocity model: Geophysics, **58**, 873-882.

Versteeg, R. J., 1994, The Marmousi experience: Velocity model determination on a synthetic complex data set: Rice University.

Veire, H. H., and M. Landrø, 2006, Simultaneous inversion of PP and PS seismic data: Geophysics, **71**, no. 3, R1–R10.

Virieux, J., and S. Operto, 2009, An overview of full-waveform inversion in exploration geophysics: Geophysics, **74**, WCC127-WCC152.

Wards, B. D., Margrave, G. F., and Lamoureux M. P., 2008, Phase-shift time-stepping for reverse-time migration, the Marmousi data experience, CREWES Research Report.

Warner, M., Ratcliffe, A., Nangoo, T., Morgan, J., Umpleby, A., Shah, N., Vinje, V., Štekl, I., Guasch, L., Win, C.,Conroy, G., and Bertrand, A., 2013, Anisotropic 3D full-waveform inversion:Geophysics, **78**(2), R59–R80.

Weglein, A., F. Gasparotto, P. Carvalho, and R. Stolt, 1997, An inverse-scattering series method for attenuating multiples in seismic reflection data: Geophysics, 62, 1975–1989, http://dx.doi.org/10.1190/1.1444298.

Wilson, M. R., Khaniani H., and Bancroft J. C., 2011, Analytic and numerical considerations for velocity grid smoothing in ray based modelling and migration: CREWES Research Report.

Yilmaz, Ö., 1989, Velocity-stack processing: Geophysical Prospecting, **37**, 357–382.

Zuleta, L., 2012, Near-surface characterization and Vp/Vs analysis of a shale gas basin: M.Sc. Thesis, University of Calgary.

Zhou, M., 2003, a well-posed PML absorbing boundary condition for 2D acoustic wave equation: Research report of Utah Tomography and Modeling/Migration Development Project.